REPORT DOCUMENTATION PAGE

Form Approved
OMB No. 0704-0188

1. AGENCY USE ONLY (Leave blank)	2. REPORT DATE	3. REPORT TYPE AND DATES COVERED
		FINAL REPORT 1 Dec 91 - 31 Oct 94

4. TITLE AND SUBTITLE
Studies of Mechanisms of Short Wavelength Generation with Strong-field Interactions

5. FUNDING NUMBERS
61102F
2301/BS

6. AUTHOR(S)
Professor Charles K. Rhodes

7. PERFORMING ORGANIZATION NAME(S) AND ADDRESS(ES)
Laboratory for Atomic, Molecular, and Radiation Physics
Department of Physics
Univ of Illinois at Chicago
845 West Taylor Street
Chicago, Illinois 60607-7059

8. PERFORMING ORGANIZATION REPORT NUMBER
AFOSR-TR-95-0303

9. SPONSORING/MONITORING AGENCY NAME(S) AND ADDRESS(ES)
AFOSR/NE
110 Duncan Avenue Suite B115
Bolling AFB DC 20332-0001

10. SPONSORING/MONITORING AGENCY REPORT NUMBER
F49620-92-J-0068

11. SUPPLEMENTARY NOTES

12a. DISTRIBUTION/AVAILABILITY STATEMENT
APPROVED FOR PUBLIC RELEASE: DISTRIBUTION UNLIMITED

13. ABSTRACT (Maximum 200 words)

SEE FINAL REPORT ABSTRACT

19950523 060

14. SUBJECT TERMS	15. NUMBER OF PAGES
	16. PRICE CODE

17. SECURITY CLASSIFICATION OF REPORT	18. SECURITY CLASSIFICATION OF THIS PAGE	19. SECURITY CLASSIFICATION OF ABSTRACT	20. LIMITATION OF ABSTRACT
UNCLASSIFIED	UNCLASSIFIED	UNCLASSIFIED	UNCLASSIFIED

UIC The University of Illinois at Chicago

Laboratory for Atomic, Molecular, and Radiation Physics (M/C 273)
Department of Physics
College of Liberal Arts and Sciences
845 West Taylor Street
Chicago, Illinois 60607-7059
(312) 996-4868 Fax: (312) 996-8824

13 April 1995

"STUDIES OF MECHANISMS OF SHORT WAVELENGTH GENERATION WITH STRONG-FIELD INTERACTIONS"

FINAL REPORT FOR
GRANT #F49620-92-J-0068

Covering the Period:

11/01/91 - 10/31/94

Prepared for: Dr. Howard R. Schlossberg
Air Force Office of Scientific Research
Bolling Air Force Base
Building 410, Room C219
Washington, D. C. 20332

Principal Investigator: Charles K. Rhodes

Co-Investigators: Armon McPherson
Keith Boyer

Table of Contents

ABSTRACT

The development of a unified picture of short-pulse high-intensity multiphoton processes, embracing atoms, molecules, and solids, appears possible through the study of clusters. Of particular significance are possible intra-cluster processes that can influence the mechanism of ionization and lead to the production of inner-shell vacancies. Inner-shell excitation leading to prompt X-ray emission is specifically considered and the treatment leads to the definition of a critical cluster size n_c representing the achievement of maximal X-ray emission from the ensemble. These results suggest the possibility of designing a new class of molecular materials optimized for the efficient production and amplification of X-rays. Recent experiments, specifically designed to evaluate certain essential predictions of the cluster picture, have furnished considerable supporting evidence for the main features of the proposed model. These studies, which involved Kr and Xe, (1) established the crucial role of cluster formation in the generation of soft X-ray ($\sim$ 80 - 150 eV) emission, (2) verified the scaling of this new phenomenon in to the kilovolt ($\sim$ 800 - 2100 eV) region, (3) provided important insights concerning the dynamical character of the strong-field coupling to the clusters, (4) demonstrated the production of "hollow" atoms, and (5) combined the cluster excitation with a recently discovered mode of channeled propagation. These results strongly indicate that the predicted amplification can be achieved.

I. INTRODUCTION

Our recent work has been aimed at the study of the properties of X-ray emission from multiphoton excited molecules and clusters. As discussed in this report, the basic scaling relations stemming from a general analysis [1] of prompt X-ray emission from ensembles of closely grouped atoms indicate that clusters of heavy atoms and/or suitably designed molecules containing heavy atoms have unusually favorable properties for the production and amplification of X-rays in the kilovolt range. The scaling laws found indicate a very strong dependence on certain atomic and molecular properties which favors heavy materials in a potent and obvious way. In this analysis, explicit contact is made with six independent experimental observations involving three materials (Ar, Kr, and Xe), all either unexplained or anomalous findings concerning the generation of short wavelength ($\lambda \leq 200$ Å) radiation. Consistent agreement of these data with the analysis is found in every case. It is considered significant that this synthesis can be achieved with a treatment that only involves known atomic and molecular properties without the incorporation of additional free parameters.

Four new experimental results [2,3] concerning multiphoton induced emissions (1) from Xe in the 145 - 152 Å range, (2) from Kr in the 72 - 140 Å region, (3) from Xe in the 11 - 17 Å range, and (4) from Kr in the 7 Å region, arising from experiments explicitly designed to test the cluster model, provide strong confirming evidence for the physical picture presented. These results support the concept of a molecular design of specific systems for the production and amplification of X-rays.

The prospects of X-ray amplification are enormously enhanced by knowledge stemming from previous studies [4,5] of confined propagation in which channel formation has been

observed [4]. This physical mechanism enables the spatial distribution of the excited material to be efficiently produced in a geometry suitable for amplification [6-8].

The overall goal of our program is the union of these two physical processes, namely, (1) the cluster excitation and (2) the channeled propagation, in order to produce X-ray sources of exceptional brightness for 3-dimensional microimaging.

II. DISCUSSION OF RESEARCH

A. Multiphoton X-Ray Generation from Molecules and Clusters

A unified picture of short-pulse high-intensity multiphoton processes, embracing atoms, molecules and solids has been proposed in relation to the study of the behavior of clusters [1]. This model is described in Appendix A. Specific experimental tests of the cluster concept have also been performed, the most informative of which were conducted in the kilovolt region and involved the observation of Kr L-shell and Xe M-shell emissions. These findings are presented in Appendices B and C. The production of "hollow" atoms was also demonstrated with the observation of Xe(L) emission in the 4 - 5 keV range, a result presented in Appendix D.

Important scaling relationships have been established by these studies, particularly concerning the energy transfer rate. These results are given in Appendix E. The main conclusion is that energy deposition rates exceeding ~ 1 W/atom are feasible in appropriately designed clusters or molecules incorporating heavy atoms.

B. Channeled Propagation

The spatial control of the energy deposited for excitation plays a crucial role in establishing the conditions for X-ray amplification. The existence of a confined mode of propagation, which occurs under conditions identical with those suitable for excitation of the

clusters, is now supported by both theoretical [6,9] analysis and experimental [10] evidence, as described in Appendices F and G, respectively. This phenomenon has an enormous influence on the scaling relationships [8] governing amplification, the analysis of which is presented in Appendix H. The main conclusion is that ~ 1 J of excitation energy is sufficient to produce strong amplification at quantum energies well into the kilovolt range.

III. RESEARCH FINDINGS

The goal of our work is the union of the material excitation, discussed in Section II.A, with the confined propagation, described in Section II.B. This step would bring into conjunction the two basic requirements for efficient X-ray amplification, namely, (1) a highly excited nonequilibrium medium and (2) a spatial distribution configured for directional amplification.

Preliminary experimental findings obtained by imaging the X-ray emitting zone with a pin-hole camera indicate that this conjunction is possible. The results involve Xe M-shell emission (~ 1 keV) produced under the conditions described in Appendix C. The pin-hole camera was positioned so that a transverse view of the excited region was observed. The camera was equipped with either a 100 μm or 5 μm pin-hole and a filter that eliminated radiation with a quantum energy less than ~ 500 eV. The signal was recorded on a two-dimension array and stored in a microprocessor. The exposures were sufficiently strong that single-pulse images were recorded.

The image of the Xe M-shell kilovolt radiation recorded with the 100 μm pin-hole is illustrated in Fig. (1). The z-coordinate represents the direction of propagation (right to left) and the transverse direction is designated by the r-coordinate. The spatial resolution of the image is ~ 100 μm, the dimension of the pin-hole. A line-out along the axis [(r,z) = (0,z)] is shown in Fig. (2). A clear asymmetry about the focal position of the 248 nm radiation is present. Significantly, the brighter zone is on the far side of the focus and extends for a distance

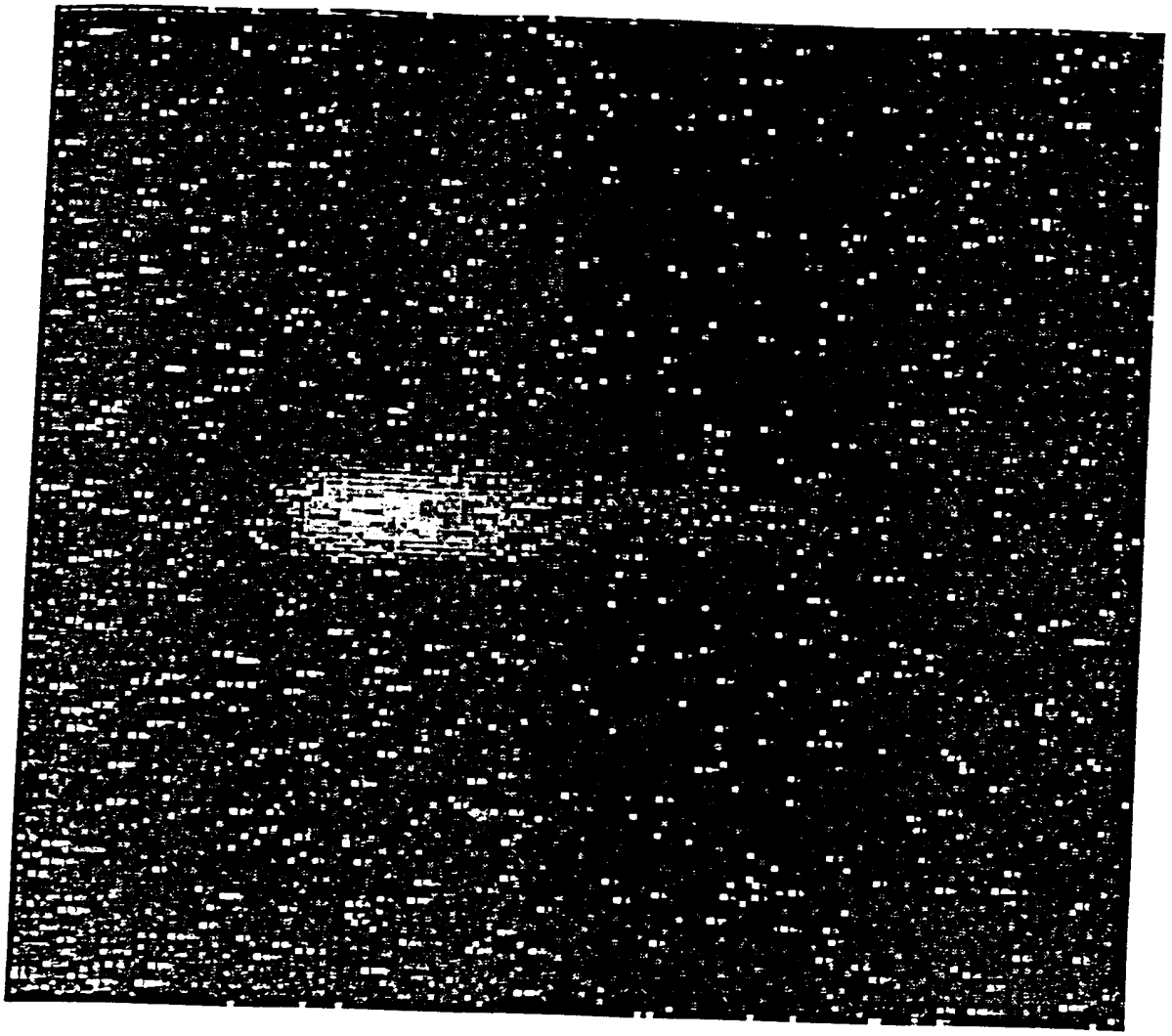

← Direction of 248 nm Propagation

Fig. (1): Pin-hole X-ray camera image in transverse direction indicating the spatial distribution of Xe M-shell radiation (~ 1 keV). The pin-hole had a diameter of ~ 100 μm. The stagnation pressure of the pulsed-valve was 30 psi and the temperature was 293 K.

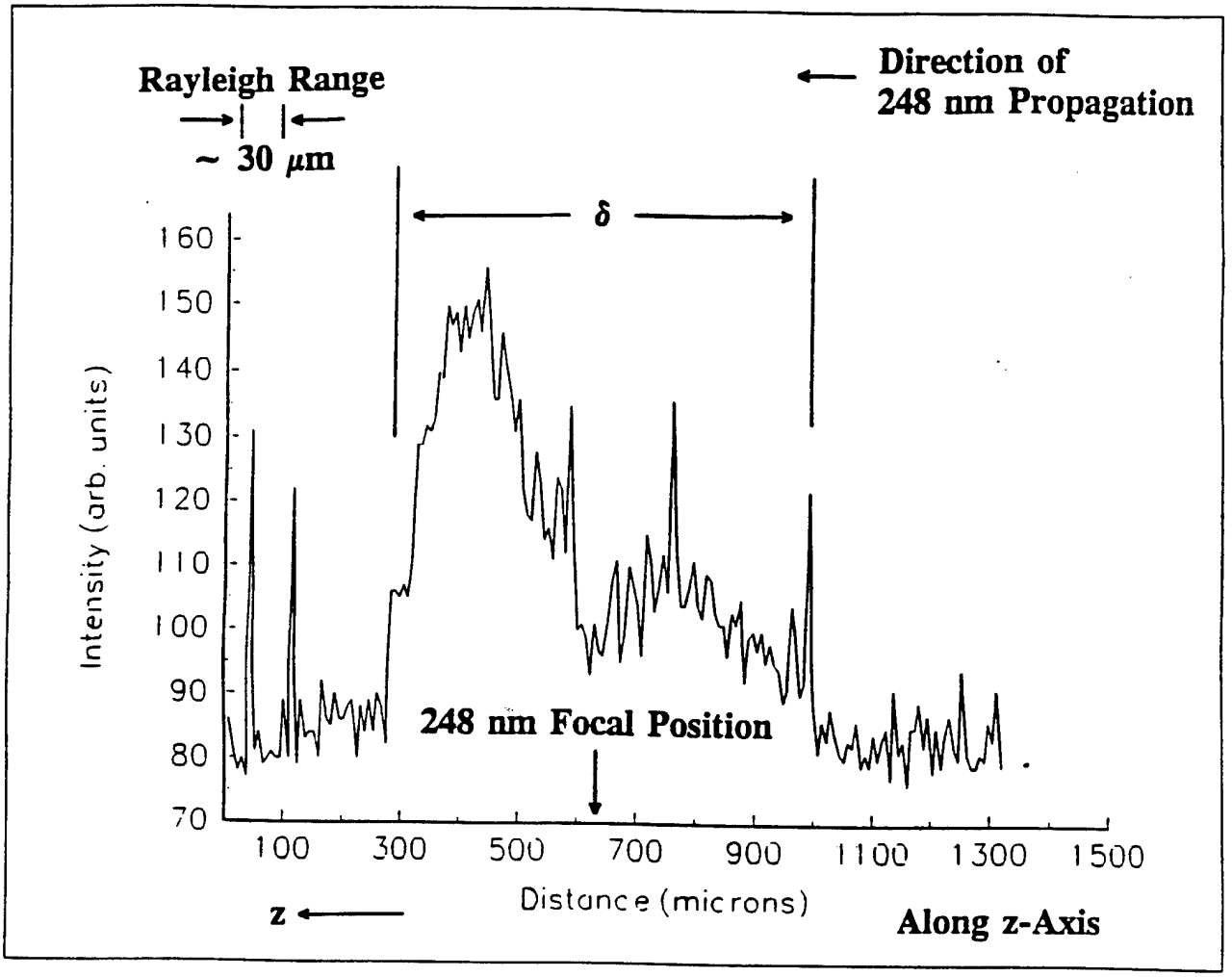

Fig. (2): Line-out [(r,z) = (0,z)] of the data shown in Fig. (1). The position of the 248 nm focal point (z ≡ 625 μm) is indicated along with a marker indicating the Rayleigh range (~ 30 μm) corresponding to the focusing system used for the 248 nm radiation. The length δ represents estimated length of the region in which material from the pulse-valve is present.

present. Significantly, the brighter zone is on the far side of the focus and extends for a distance (200 or 300 μm), a value many times the Rayleigh range ($\sim$ 30 μm) of the optical system used for focusing. Figure (3) illustrates the image obtained with a 5 μm pin-hole while Fig. (4) shows the corresponding axial line-out. The asymmetry is clearly present in the latter as in Fig. (2). Careful inspection of the data from other exposures reveals the existence of a narrow filament with a length of $\sim$ 200 μm and a radial extent limited by the resolution of the imaging system ($\sim$ 20 μm). This radial profile is shown in Fig. (5), which illustrates a transverse line-out of the filamentary region.

The images show that the power density of the incident 248 nm radiation is confined in the region beyond the focus. This type of behavior would be expected if the channeling mechanism discussed in Appendices F and G were influencing the propagation. All the experimental data indicate that this is the case.

IV. CONCLUSIONS

The union of a (1) multiphoton cluster/molecule mechanism for the production of X-rays and (2) a relativistic/charge-displacement process for the establishment of confined propagation appears possible. This combination intrinsically has exceptionally favorable characteristics for the efficient amplification of X-rays in the kilovolt spectral region.

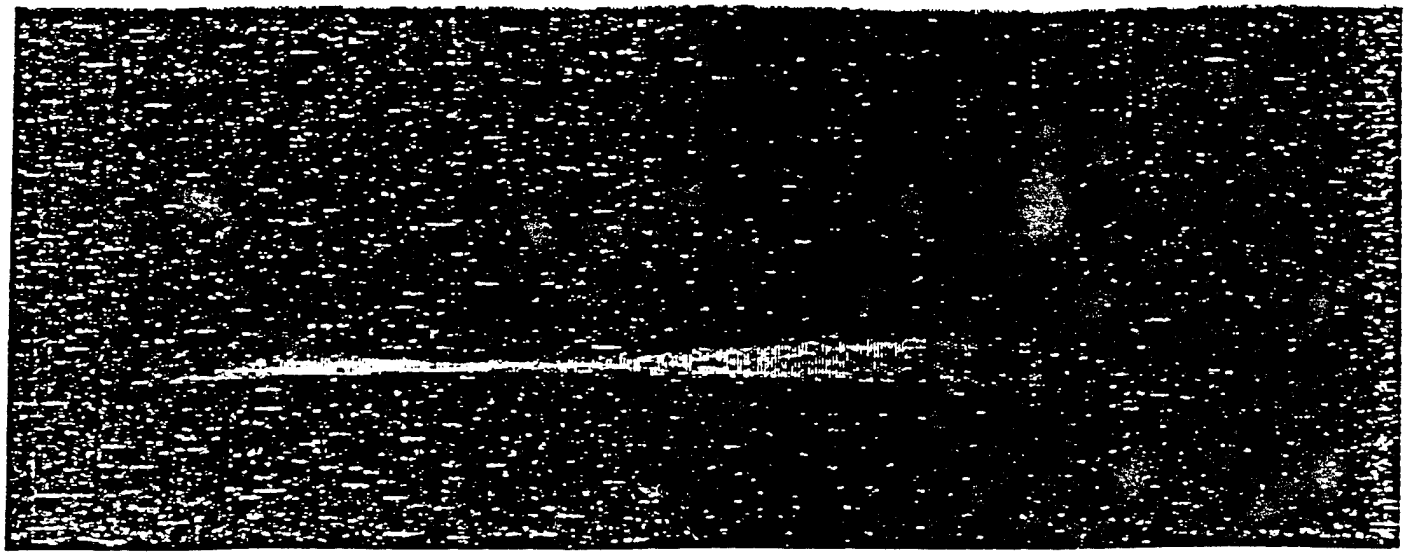

← Direction of 248 nm Radiation

Fig. (3): Pin-hole X-ray camera image in transverse direction indicating the spatial distribution of Xe M-shell radiation ($\sim$ 1 keV). The pin-hole had a diameter of 5 μm. The stagnation pressure of the pulsed-valve was 30 psi and the temperature was 273 K.

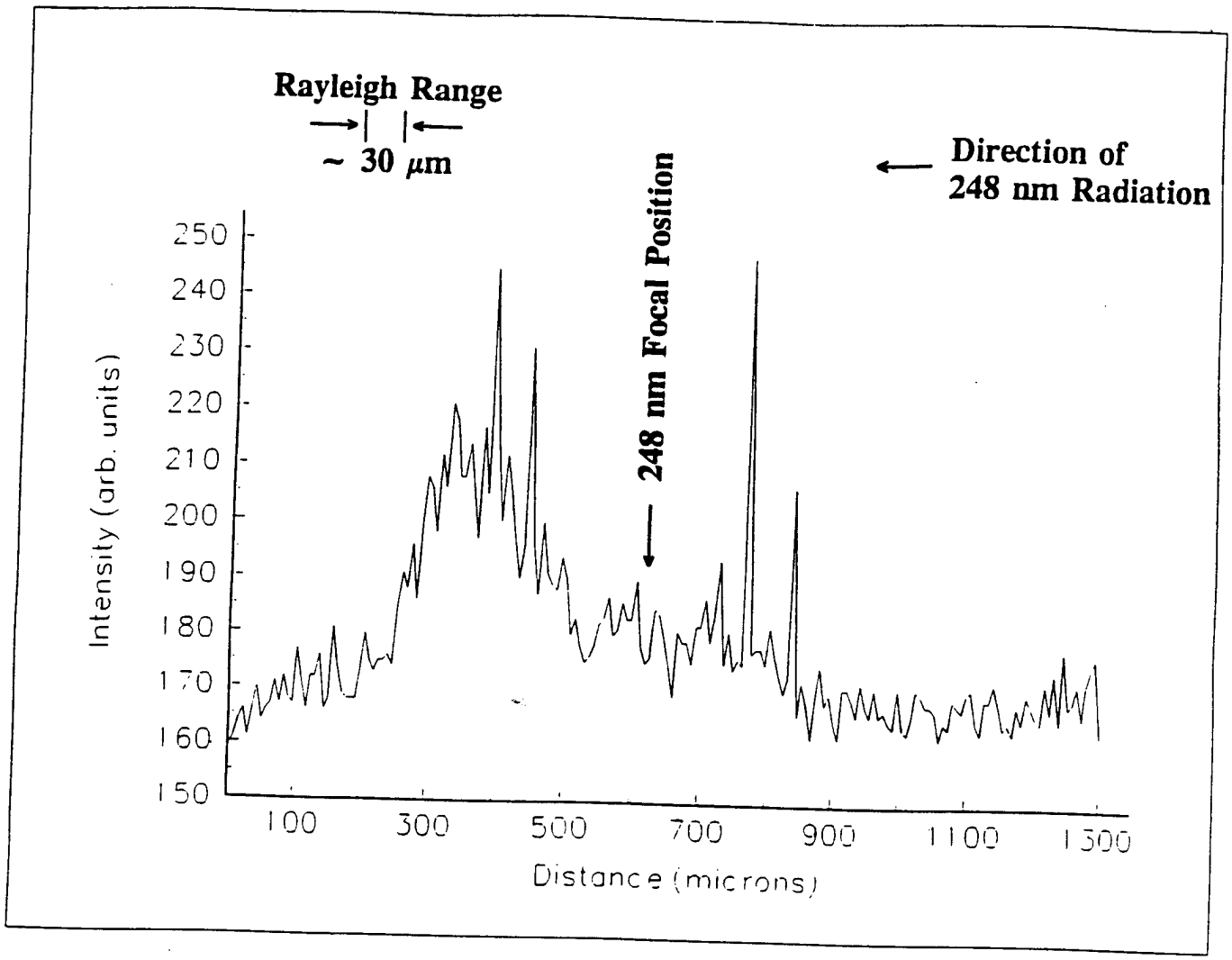

Fig. (4): Line-out [(r,z) = (0,z)] of the data shown in Fig. (3). The approximate position of the 248 nm focal point (z ≡ 625 μm) is indicated along with a marker indicating the Rayleigh range (~ 30 μm) corresponding to the focusing system used for the 248 nm radiation.

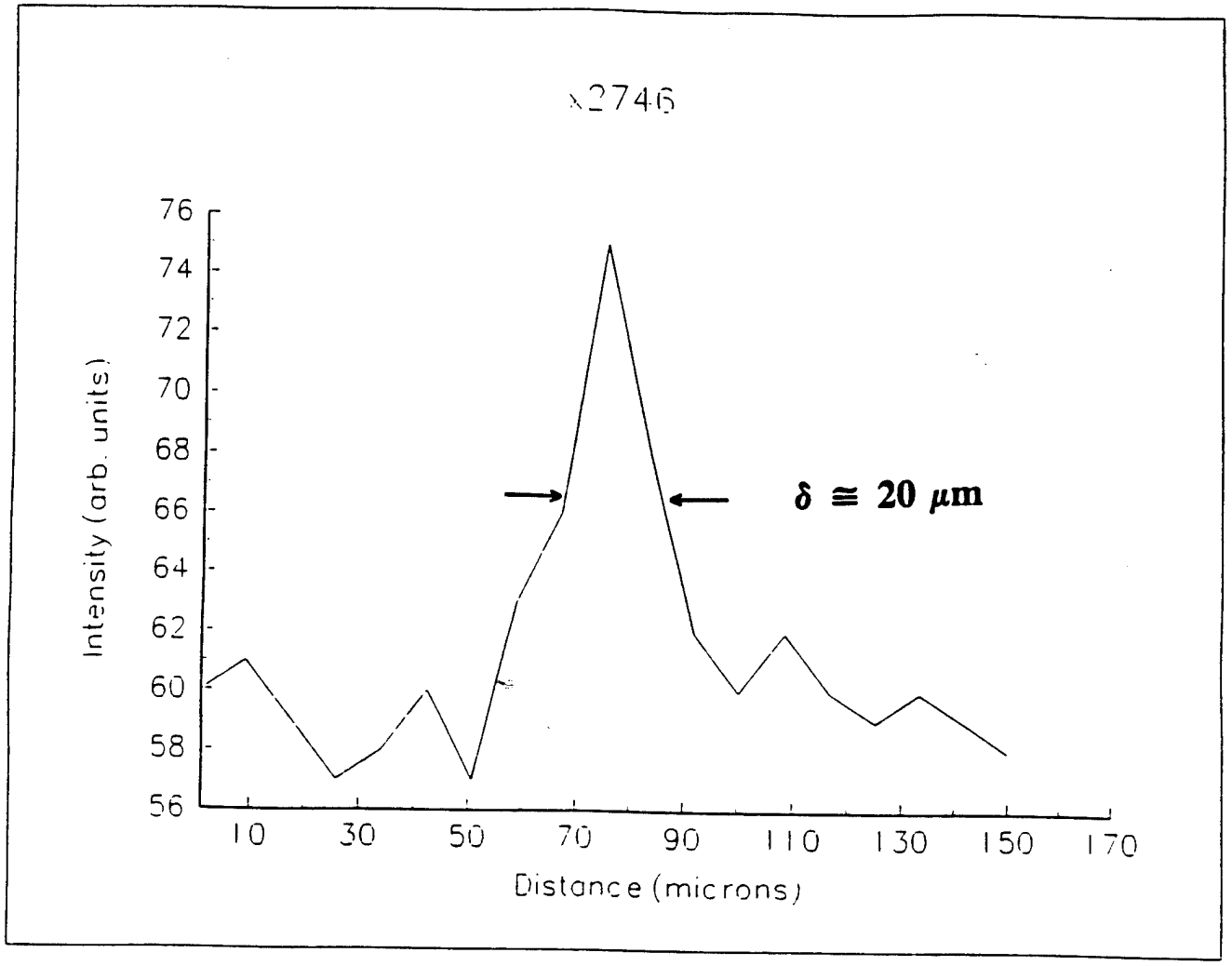

Fig. (5): Radial line-out of observed narrow filamentary region for an Xe pressure of 30 psi and a temperature of 273 K. The measured FWHM of 20 μm corresponds to the limiting spatial resolution of the X-ray imaging system used.

V. REFERENCES

1. A. McPherson, T. S. Luk, B. D. Thompson, K. Boyer and C. K. Rhodes, "Multiphoton Induced X-Ray Emission and Amplification from Clusters," Appl. Phys. B 57, 1 (1993).
2. A. McPherson, T. S. Luk, B. D. Thompson, K. Boyer and C. K. Rhodes, "Role of Cluster Formation on Multiphoton Induced Soft X-Ray (75 - 152 Å) Emission from Kr and Xe Ions," submitted to Physical Review Letters, 1 September 1993.
3. A. McPherson, X. Chen, B. D. Thompson, A. B. Borisov, O. B. Shiryaev, K. Boyer and C. K. Rhodes, "Kilovolt X-Ray (5 - 16 Å) Emission from Multiphoton Excited Kr and Xe Clusters," submitted to Physical Review Letters, 1 September 1993.
4. A. B. Borisov, A. V. Borovskiy, V. V. Korobkin, A. M. Prokhorov, O. B. Shiryaev, X. M. Shi, T. S. Luk, A. McPherson, J. C. Solem, K. Boyer and C. K. Rhodes, "Observation of Relativistic/Charge-Displacement Self-Channeling of Intense Subpicosecond Ultraviolet (248 nm) Radiation in Plasmas," Phys. Rev. Lett. 68, 2309 (1992).
5. A. B. Borisov, A. V. Borovskiy, O. B. Shiryaev, V. V. Korobkin, A. M. Prokhorov, J. C. Solem, T. S. Luk, K. Boyer and C. K. Rhodes, "Relativistic and Charge-Displacement Self-Channeling of Intense Ultrashort Laser Pulses in Plasmas," Phys. Rev. A 45, 5830 (1992).
6. J. C. Solem, T. S. Luk, K. Boyer and C. K. Rhodes, "Prospects for X-Ray Amplification with Charge-Displacement Self-Channeling," IEEE J. Quant. Electron. QE-25, 2423 (1989).
7. K. Boyer, A. B. Borisov, A. V. Borovskiy, O. B. Shiryaev, D. A. Tate, B. E. Bouma, X. M. Shi, A. McPherson, T. S. Luk and C. K. Rhodes, "Method of Concentration of Power in Materials for X-Ray Amplification," Appl. Opt. 31, 3433 (1992).
8. K. Boyer, T. S. Luk, A. McPherson, X. M. Shi, J. C. Solem, C. K. Rhodes, A. B. Borisov, A. V. Borovskiy, O. B. Shiryaev and V. V. Korobkin, "X-Ray Amplifier Energy Deposition Scaling with Channeled Propagation," in the Proceedings of the International Conference on Lasers '91, edited by F. J. Duarte and D. G. Harris (STS Press, McLean, VA 1992) p. 9.
9. A. B. Borisov, A. V. Borovskiy, O. B. Shiryaev, V. V. Korobkin, A. M. Prokhorov, J. C. Solem, T. S. Luk, K. Boyer and C. K. Rhodes, "Relativistic and Charge-Displacement Self-Channeling of Intense Ultrashort Laser Pulses in Plasmas," Phys. Rev. A 45, 5830 (1992).
10. A. B. Borisov, A. V. Borovskiy, V. V. Korobkin, A. M. Prokhorov, O. B. Shiryaev, X. M. Shi, T. S. Luk, A. McPherson, J. C. Solem, K. Boyer and C. K. Rhodes, "Observation of Relativistic and Charge-Displacement Self-Channeling of Intense Subpicosecond Ultraviolet (248 nm) Radiation in Plasmas," Phys. Rev. Lett. 68, 2309 (1992).

VI. APPENDICES

Appendix A: "Multiphoton Induced X-Ray Emission and Amplification from Clusters"

Appl. Phys. B 57, 337–347 (1993)

Applied Physics B Photophysics and Laser Chemistry

Multiphoton-Induced X-Ray Emission and Amplification from Clusters

A. McPherson, T. S. Luk, B. D. Thompson, K. Boyer, C. K. Rhodes

Laboratory for Atomic, Molecular, and Radiation Physics, Department of Physics, M/C 273, University of Illinois at Chicago, 845 W. Taylor, Room 2136, Chicago, IL 60607-7059, USA (Fax: +1-312/996-88 24)

Received 28 June 1993/Accepted 4 August 1993

Abstract. The development of a unified picture of short-pulse high-intensity multiphoton processes, embracing atoms, molecules, and solids, appears possible through the study of clusters. Of particular significance are possible intra-cluster processes that can influence the mechanism of ionization and lead to the production of inner-shell vacancies. Inner-shell excitation leading to *prompt* X-ray emission is specifically considered and the treatment leads to the definition of a *critical cluster size* n_c representing the achievement of maximal X-ray emission from the ensemble. These results suggest the possibility of *designing a new class of molecular materials* optimized for the efficient production and amplification of X-rays.

PACS: 97.85, 33.00, 36.00, 42.55.Vc

This article introduces and explores the possibility of developing a unified picture of short-pulse (< 100 fs) high-intensity (> 10^{15} W/cm^2) multiphoton processes embracing atoms, molecules, and solids, through the study of clusters [1]. Rare-gas clusters $(RG)_n$, on account of their simplicity and close connection with known atomic and molecular properties, appear particularly suitable for this purpose. Of particular significance are possible intra-cluster processes that can influence the mechanism of ionization. This can (1) lead to the production of inner-shell vacancies and (2) the generation of prompt X-rays with a potential for strong amplification. The analysis developed below gives simple relations concerning inner-shell excitation and X-ray emission applicable over a large range of cluster sizes ($1 \leq n \leq 10^3$). The treatment also leads to the definition of a *critical cluster size* n_c representing the achievement of maximal X-ray emission from the ensemble, a parameter that is found to be directly analogous to the concept of nuclear critical mass.

Explicit contact is made with six independent experimental observations [2–4] involving three materials (Ar, Kr, Xe), all either unexplained or anomalous findings concerning the generation of short wavelength ($\lambda \leq 200$ Å) radiation. Consistent agreement with the analysis is found in each case. Significantly, this synthesis is achieved with the *exclusive* use of previously established atomic and molecular properties. A connection with studies of X-ray generation from solid surfaces (BaF_2) is also made in conjunction with this analysis.

1 Coupling to Clusters

1.1 Simple Initial Formulation

The rare-gas cluster is considered as a spherical group of (n) atoms having mutual interatomic spacings r_0 and an overall radius R for the ensemble given by $R \cong r_0 n^{1/3}$, $(n \geq 3)$, and $R \cong r_0(n/2)$, $(n = 1, 2)$, in analogy with simple descriptions [5, 6] of nuclei. Consider irradiation of the cluster at wavelength λ with the stipulation (a) that the characteristic dimension R of a fully ionized cluster be less than the skin depth δ and (b) the assumption that the atoms, which are weakly bound by van der Waals forces, respond to the external optical field as *free* atoms whose ionization can be estimated with a tunneling picture. Condition (a) enables all atoms in the cluster simultaneously to experience the same field strength, since $R < \delta \ll \lambda$. Consistent with these assumptions, we will set the maximum dimension $R_{max} \sim 20$–30 Å, or equivalently, a maximum cluster size of $n_{max} \sim 10^3$. Assumption (b) enables a simple experimentally evaluated procedure to be used to estimate the level of atomic ionization produced. This gives the threshold intensity for ionization [7, 8] as

$$I_{th} = cE_p^4/128\pi e^6 Z^2 , \quad (1)$$

where E_p is the ionization potential, Z the resulting ionic charge, c the speed of light, and e the electronic charge.

1.2 Intra-Cluster Processes

The model of a rare-gas cluster as a sum of *independent* atoms, held weakly together by van der Waals forces and

responding as *individual* systems to the external optical field, is expected to become invalid as the cluster becomes sufficiently large and/or the external electromagnetic field becomes sufficiently strong. This limit could arise through the action of inelastic scattering processes produced by ionized electrons originating from atoms in the cluster that are accelerated by the external optical field and collide with other atoms or ions in the system. Roughly, such intra-cluster processes can be considered as

$$e^- + X^{q+} \xrightarrow{\sigma_{ex}} e^- + (X^{q+})^* , \tag{2}$$

which produces excitation, or the reaction

$$e^- + X^{q+} \xrightarrow{\sigma_{ei}} e^- + e^- + X^{(q+1)+} , \tag{3}$$

which causes additional ionization.

An approximate estimate of the number N_x of such excitations or ionizations can be written as the product of the number of electrons produced in the cluster (nZ), the atomic density in the cluster (r_0^{-3}), the cross section for the inelastic channel under consideration (e.g. σ_{ei}), and the characteristic scale length of the cluster (R). Therefore, for reaction (3),

$$N_x \cong (nZ)\sigma_{ei} r_0^{-3} r_0 n^{1/3} = n^{4/3} Z \frac{\sigma_{ei}}{r_0^2} , \quad (n \geq 3) , \tag{4}$$

with Z determined through (1) for the corresponding intensity. Such a mechanism would cause the pattern of ionization to depend upon the cluster size (n), thereby yielding an observed spectrum of ionic charge states deviating from that characteristic of the free atom ($n = 1$), an easily measured feature in *direct conflict* with the picture of atomic independence assumed above in the simplest initial formulation.

An important immediate consequence of (4) is the existence of a critical size

$$n_c = \left(\frac{r_0^2}{Z\sigma_{ei}} \right)^3 \tag{5}$$

defined by $N_x = n$. Therefore, if σ_{ei} corresponds to an inner-shell ionization, with $n \geq n_c$ an *inner-shell* vacancy would be produced in *every* atom. Furthermore, since the critical size of the cluster depends inversely on the square of the atomic density ($\varrho_a^{-2} = r_0^6$) and inversely on the cube of the cross section for excitation (σ_{ei}^{-3}), n_c is a direct analogue of the nuclear concept of a critical mass, with σ_{ei} replacing the neutron fission cross section σ_{nf} and Z playing the role of the average neutron yield $\bar{\nu}$.

Certain conditions must be met in order for intra-cluster processes of the type expressed by reactions (2) and (3) to occur for an inner-shell. Specifically, such an excitation can only take place if sufficient kinetic energy is possessed by the colliding electron. To estimate this energy, and the conditions necessary for its transfer, we will assume that the electrons experience an acceleration over the characteristic dimension of (R) of the cluster by the external optical field (E) in a time short compared to the period of the oscillating wave. Furthermore, once the electrons leave the vicinity of the cluster we will assume that they represent ionization and are lost from the system. This simple procedure yields a characteristic energy ε_e given by $\varepsilon_e \cong eER$, a result that can be expressed as a characteristic minimum intensity needed for inner-shell excitation

$$I_0 = \frac{\varepsilon_e^2}{8\pi\alpha n^{2/3}/\hbar r_0^2} , \quad (n \geq 3) , \tag{6}$$

with $\alpha = e^2/\hbar c$. Since this simple picture assumes that the acceleration occurs in a time comparable to or less than a period of the wave, validity of this approximation demands that the cluster neither be too large nor the external field too small: namely, it requires that the amplitude x_e of the driven excursion of the electron caused by the field be comparable to or larger than the cluster dimension R. If we set the limiting situations as $x_e = R$, assume that the electron is free, and put $x_e = eE/m\omega^2$, with m denoting the electron mass and ω the angular frequency of the external optical field, we can define another limiting intensity as

$$I_n(\lambda) = \frac{2\pi^3}{\alpha} \left(\frac{r_0}{\lambda} \right)^2 mc^2 \frac{c}{\lambda_c} \frac{n^{2/3}}{\lambda^2} , \quad (n \geq 3) , \tag{7}$$

with λ denoting the wavelength of the optical field and λ_c being the electron Compton wavelength. In this picture, an inner-shell electron with binding energy ε_e can be ionized if the intensity exceeds a *lower bound* given by I_0 or $I_n(\lambda)$, whichever is greatest.

2 Prompt X-Ray Emission

Excitation of the type discussed above can lead to the emission of *prompt* inner $(j-1)$ shell radiation in the X-ray range. Generally, in addition to the production of a hole in the $(j-1)$ shell, the possibility of *prompt* $j \rightarrow j-1$ transitions requires retention of at least one electron in the j-shell during the course of irradiation. This determines an *upper bound* on the intensity of irradiation $I_{max}(j)$ through (1) which is, in the simple model considered, *independent* of the cluster size.

2.1 Krypton

Considering Kr M-shell emission as an example, from the threshold ionization curve [7–9] derived from (1) and exhibited in Fig. 1, we find that $I_{max}(N) \cong 2 \times 10^{16}$ W/cm^2. By combining the conditions stemming from (6) and (7) with $I_{max}(N)$, Fig. 2 illustrates the conditions on intensity and cluster size for which the model allows *prompt* M-shell emissions. The region corresponding to prompt L-shell [10] emissions ($\varepsilon_e = 1.67$ keV) is also represented in Fig. 2.

Several important results are manifest in the form of Fig. 2. First, the crossing points $n_p(P)$ and $n_q(Q)$, found by equating (1) with (6) and (7), respectively, yield the condition for the existence of an allowed zone for prompt emission as

$$\frac{n_q}{n_p} = \left(\frac{\lambda}{8\pi Z\alpha\lambda_c} \right)^6 \left(\frac{E_p}{mc^2} \right)^9 \left(\frac{E_p}{\varepsilon_e} \right)^3 > 1 , \tag{8}$$

an expression which we observe is *independent* of r_0. Furthermore, (8) strongly favors the situation in which the magnitudes of the characteristic energies, and hence, the corresponding levels of ionization Z, are high. This is

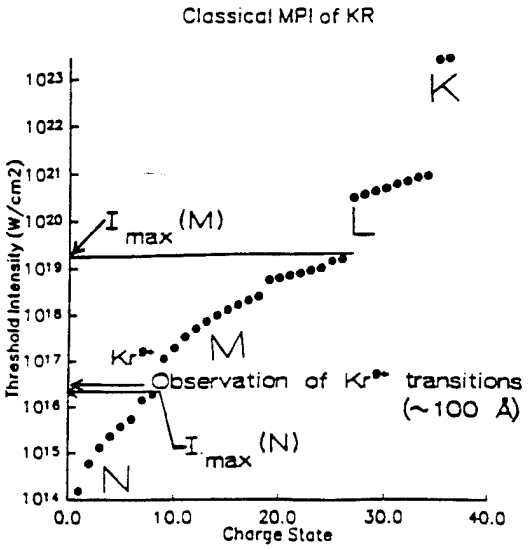

Fig. 1. Threshold intensity I_{th} for ionization shown as a function of resulting charge state Z calculated for Kr with the classical method described in [7, 8]. The respective atomic shells (K, L, M, N) are designated. The maximum intensities $I_{max}(M)$ and $I_{max}(N)$ associated with leaving some M-shell and N-shell populations, respectively, are indicated. Also shown is the intensity ($\sim 5 \times 10^{16}$ W/cm^2) at which Kr^{9+} transitions at ~ 100 Å were observed in fluorescence in experiments reported in [4, 11]

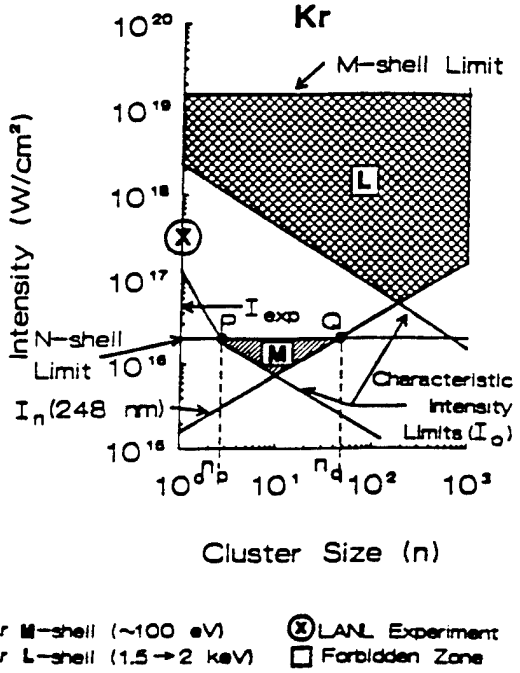

Fig. 2. Representation of limiting conditions applicable for production of prompt Kr L-shell and M-shell emission from Kr clusters as a function of intensity of irradiation and cluster size. The experimental datum (LANL) corresponding to Lee et al. [2] and the crossing points P and Q are shown. The additional condition I_n(248 nm), stemming from (7), is also represented. See text for other details

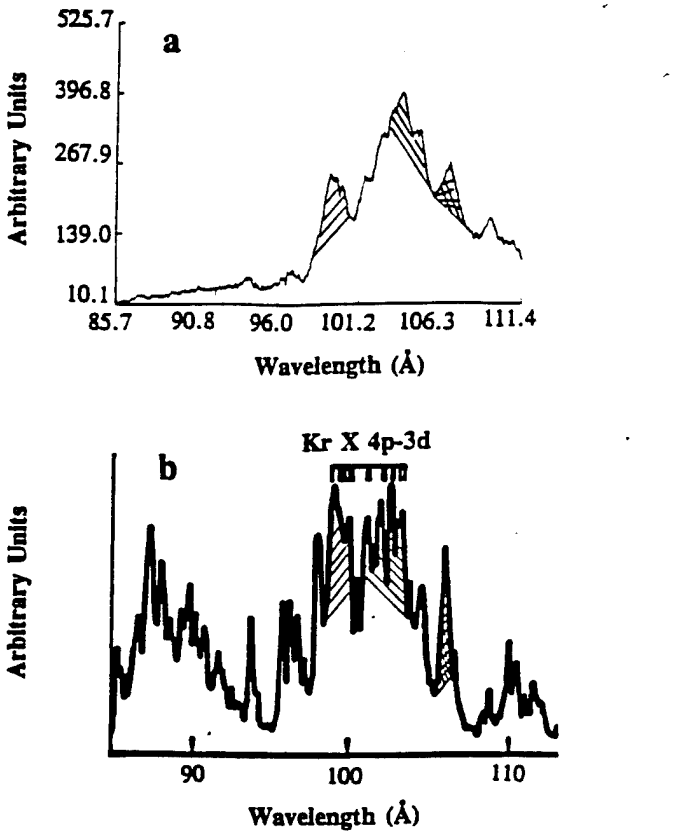

Fig. 3a, b. Spectra of Kr in the region near 100 Å. a Multiphoton produced spectrum of Kr produced in a gas jet, as described in [11], in the ~85-100 Å region with a peak intensity of irradiation of $\sim 5 \times 10^{16}$ W/cm^2. The $4p \rightarrow 3d$ features from Kr^{9+} appear prominently. b Spectrum of Kr observed in a theta pinch plasma by Jones and Källne [12]. The Kr^{9+} $4p \rightarrow 3d$ transitions are indicated. The correspondence between the multiphoton and the theta pinch produced spectra involving Kr^{9+} in the ~100 Å region is marked

readily seen by letting E_p be approximated by hydrogenic binding ($E_p \propto Z^2$), keeping $E_p/\varepsilon_e \sim$ constant, and noting that $n_q/n_p \sim Z^{12}$ follows. As a natural consequence of the systematics of atomic binding energies, we observe that large allowed zones are associated with level structures in the kilovolt range, a feature apparent from comparison of the regions of M-shell and L-shell emission shown in Fig. 2.

The information in Fig. 2 can be directly related to *two* independent experimental studies, one [2] involving the search for *prompt* multiphoton-induced X-ray emission from free Kr atoms ($n = 1$) and another concerning the measurement of fluorescence produced in a pulsed gas target undergoing multiphoton excitation [4, 11]. The datum corresponding to the former [2] ($I \cong 3 \times 10^{17}$ W/cm^2, $n = 1$), designated as LANL, appears on Fig. 2. Although the experiment actually represents all intensities $I \leq 10^{17}$ W/cm^2 due to the distribution of intensity occurring in the focal region, we see from Fig. 2 that there is *no overlap* of the experimental conditions with *either* of the zones for prompt L- or M-shell emissions. The experimental region lies well below the L-shell region and is excluded from the M-shell zone by the *crossing* P. Hence, prompt X-ray emission is forbidden, a prediction fully in agreement with the experimental observation of none [2].

The second experiment involves the anomalous detection [4, 11] of intense Kr M-shell fluorescence from Kr^{9+} $4p \rightarrow 3d$ transitions at ~ 100 Å, as illustrated in Fig. 3a, arising from material produced in a *pulsed gas jet* and irra-

diated at a peak intensity of $\sim 5 \times 10^{16}$ W/cm^2 with subpicosecond 248 nm radiation. The corresponding spectral region observed from a theta pinch by Jones and Källne [12] is shown in Fig. 3b.

The observation of *any* Kr^{9+} radiation by the multiphoton excitation, either prompt or delayed, immediately presents a paradox. As shown in Fig. 1, with a peak intensity of $\sim 5 \times 10^{16}$ W/cm^2, *no* production of Kr^{9+} is possible, a result that is *experimentally* based on earlier measurements of ion production [8] involving free krypton atoms under *identical* conditions of irradiation. Yet the Kr^{9+} array at $\sim$ 103 Å was among the brightest features observed throughout the entire region studied [4, 11]. However, Fig. 2 shows that the formation of *small clusters* ($n \geq 2-3$) *would* permit both anomalous ionization (Kr^{9+} production) and the emission of Kr^{9+} $4 \rightarrow 3$ radiation of the kind illustrated in Fig. 3, thereby reconciling the paradox. Furthermore, a review of the hydrodynamic properties and operating conditions [4, 11] of the pulsed valve, particularly in comparison to other work [13–15] in which Kr_2 and Kr_3 species were formed and *directly* measured [14], showed that the hydrodynamic conditions were essentially the same in both studies. Indeed, the observed pressure dependence of the Kr^{9+} signal was close to that seen in the earlier studies [14] involving Kr_2 and Kr_3 formation. Both of these considerations lead firmly to the conclusion that significant production of small Kr_n clusters was inevitable in the multiphoton experiments in which the Kr^{9+} transitions were observed.

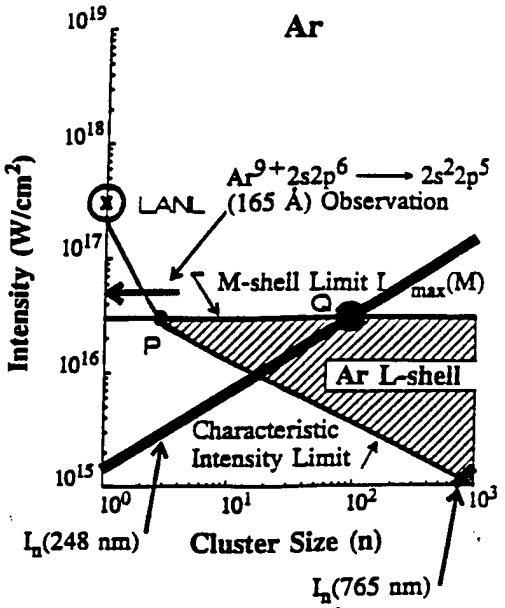

Fig. 4. Representation of limiting conditions for excitation of prompt Ar L-shell radiation from Ar clusters as a function of intensity of irradiation and cluster size. The M-shell limit is taken from Fig. 7. The allowed zone is shaded. Points P and Q designate the crossings described in the text. The conditions I_n(248 nm) and I_n(765 nm), stemming from (7), are also indicated. The experimental datum (LANL) of Lee et al. [2] is shown along with the maximum intensity ($\sim 5 \times 10^{16}$ W/cm^2) used in fluorescence studies of Ar discussed further in [3]

2.2 Argon and Xenon

Additional observations [2–4] with Ar and Xe can be explained mutatis mutandis and the corresponding diagrams appear for these materials in Figs. 4 and 5, respectively. The results [2] of Lee et al. (LANL data), which show no prompt emission, are consistent in all cases illustrated for both materials. Note the exclusion of the atomic region ($n = 1$) for Ar L-shell and Xe N-shell emissions by the crossings.

Again, however, the experiments examining the multiphoton-induced fluorescence with the pulsed jet indicate very different behavior. Fluorescence [3] from Ar, observed with a maximum intensity of irradiation of $\sim 5 \times 10^{16}$ W/cm^2, detected the clear presence of radiation at $\sim$ 165 Å on the well-known doublet $2s2p^6 \rightarrow 2s^22p^5$ transition [16] of Ar^{9+}. This finding, as shown in Fig. 6, is another paradoxical result, since Fig. 7 indicates that the threshold intensity of Ar^{9+} production is $\sim 10^{18}$ W/cm^2, approximately 20-fold *higher* than that used in the experiment. Furthermore, spectroscopic analysis of the plasma [3] led to the conclusion that electron collisions could not have produced the Ar^{9+} species. In this connection, we note that the cross section for electron collisional ionization of Ar^{8+} is quite small [17]. However, as shown in Fig. 4, small cluster formation ($n = 2, 3$) *would allow* the excitation of an L-shell electron. Since the maximum experimental intensity is also above the M-shell limit, this interaction could readily generate the Ar^{9+} species seen. Therefore, small cluster formation removes the anomaly of the Ar^{9+} production and the observed radiation on the 165 Å doublet could then be generated in the manner previously described [3].

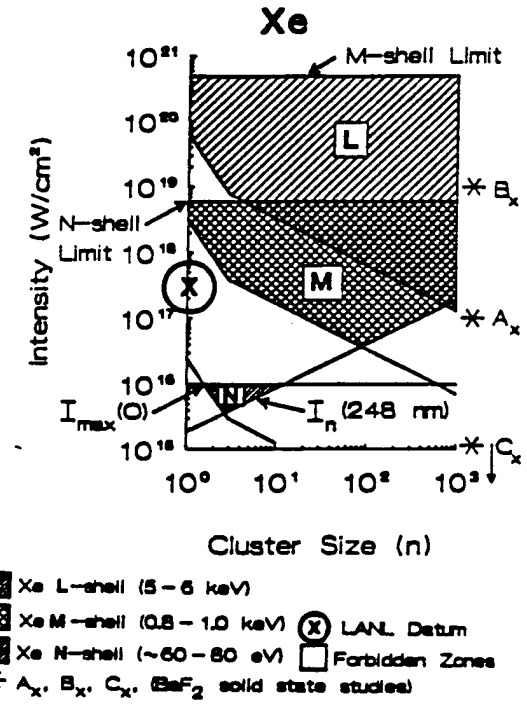

Fig. 5. Representation of limiting conditions applicable for excitation of prompt Xe N-shell, M-shell and L-shell radiation from Xe clusters as a function of intensity of irradiation and cluster size. The experimental datum (LANL) corresponding to Lee et al. [2], which falls in the forbidden zone, is shown. The boundaries are established as previously described for Kr and Ar in Figs. 2 and 4, respectively. The points A_x, B_x, and C_x correspond approximately to the conditions pertaining to the data in Figs. 11, 12, and 13, respectively. See text for details

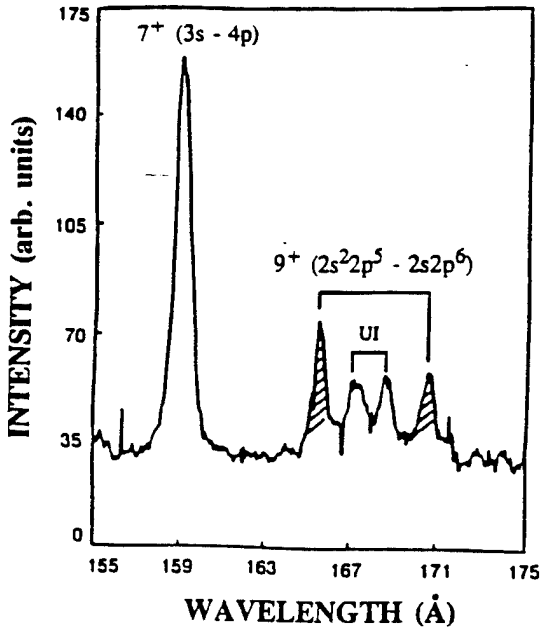

Fig. 6. Transitions observed in Ar with a pulsed-gas jet at an intensity of $\sim 5 \times 10^{16}$ W/cm^2 at 248 nm as reported in [3]. The Ar^{9+} $2s^22p^5$–$2s^22p^6$ doublet is clearly visible along with two unidentified (UI) lines. The latter may be associated with satellite transitions in Ar^{8+}

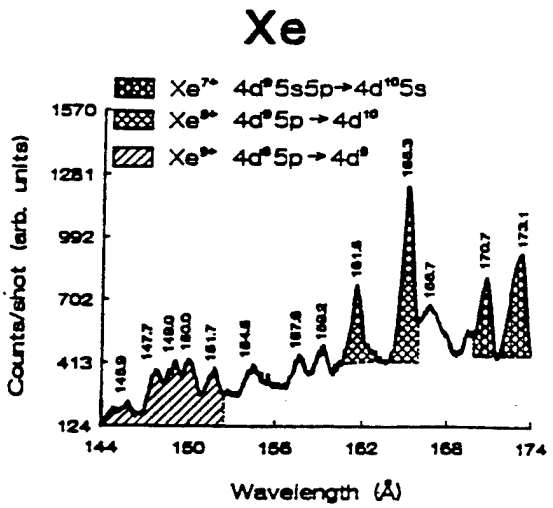

Fig. 8. Emission spectrum of Xe in the 144-174 Å region observed in a pulsed-gas jet at a peak intensity of $\sim 5 \times 10^{16}$ W/cm^2 with subpicosecond 248 nm irradiation. Features associated with Xe^{7+}, Xe^{8+}, and Xe^{9+} are identified

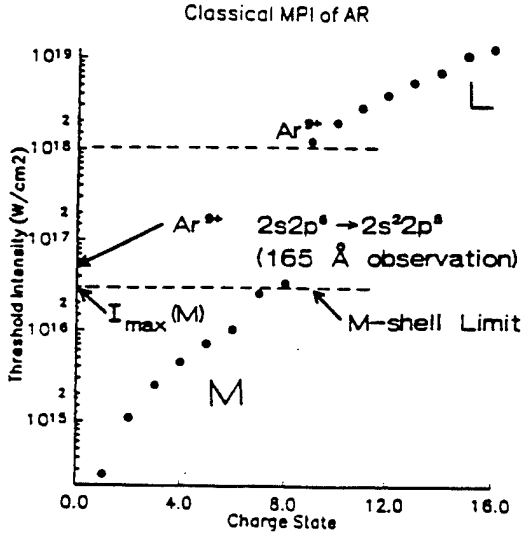

Fig. 7. Threshold intensity I_{th} for ionization shown as a function of resulting charge state Z calculated for Ar with the classical method described in [7]. The respective atomic shells (L and M) are designated. The maximum intensity $I_{max}(M)$ associated with leaving some M-shell population is indicated. Also shown is the threshold for Ar^{9+} production ($\sim 10^{18}$ W/cm^2) and the maximum intensity ($\sim 5 \times 10^{16}$ W/cm^2) utilized in fluorescence studies [3] of Ar using a pulsed-gas jet in which the 165 Å $2s2p^6 - 2s^22p^5$ transition in Ar^{9+} was observed

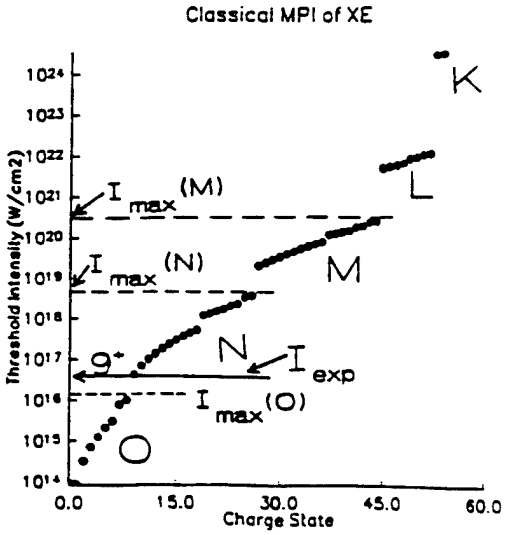

Fig. 9. Threshold intensity I_{th} shown as a function of resulting charge state Z calculated for Xe with the classical method described in [7]. The respective atomic shells (K, L, M, N, O) are designated. The maximum intensities $I_{max}(M)$, $I_{max}(N)$ and $I_{max}(O)$ associated with leaving some M-shell, N-shell and O-shell populations, respectively, are indicated. The experimental intensity ($I_{exp} \cong 5 \times 10^{16}$ W/cm^2) used in studies of fluorescence from Xe using a pulsed-gas jet is indicated. This intensity is just sufficient to lead to observable Xe^{9+} in ion measurements

A similar analysis can be applied to Xe L-shell, M-shell, and N-shell emissions which yields conclusions analogous to those found for Ar and Kr. The corresponding allowed zones for prompt emission from those shells are indicated in Fig. 5.

The multiphoton-induced fluorescence observed [11, 18] from Xe, particularly from levels involving $4d$ excitation, suggests additional important insights. Transitions [19–21] originating from states involving a $4d$ hole were observed in three species, Xe^{7+}, Xe^{8+}, and Xe^{9+}. The identified configurations of the lines shown in Fig. 8 were $4d^95s5p \rightarrow 4d^{10}5s(Xe^{7+})$, $4d^95p \rightarrow 4d^{10}(Xe^{8+})$, and $4d^85p \rightarrow 4d^9(Xe^{9+})$. The maximum intensity used at 248 nm was $\sim 5 \times 10^{16}$ W/cm^2 which is just sufficient, as seen from Fig. 9,

to lead to observable Xe^{9+} production in ion charge state measurements [18].

Experimentally, these transitions presented two obviously anomalous features, (1) their exceptional strength and (2) the nature of the radiating configurations detected. The Xe^{8+} line at 165.3 Å was by far the most intense feature seen in any of our studies of fluorescence, indicating that copious $4d$ excitation was certainly being produced. Furthermore, consider the configuration $[4d^8 5p]$ of the excited state in Xe^{9+} producing the array in the ~150 Å region. This level has *two* $4d$ holes, but retains a relatively weakly bound $5p$ electron. Production of this level by recombination from $Xe^{10+}(4d^8)$ is *not* possible, since the intensity was too low for its production [18]. Collisional excitation by sufficiently energetic electrons in the plasma formed is possible, but calls for an unusually high efficiency given the very high observed intensity of the xenon transitions. Furthermore, it was not possible to reconcile in any reasonable way the observed density dependence of the emission with collisions arising from plasma electrons. In fact, as in the case of Kr^{9+} radiation discussed above, the observed pressure dependence was in far closer accord with that associated with the formation of small rare gas clusters [14, 22] arising from the complex hydrodynamics associated with the flow.

The apparently anomalous $4d$ excitation implied by the Xe fluorescence would be expected, however, if the *cluster process* discussed above in relation to Ar and Kr is operative. In Fig. 5 the triangular zone representing the allowed region for prompt N-shell emission, as shown enlarged in Fig. 10, indicates that dimer (Xe_2) formation would be sufficient to permit *prompt* emission to occur in the regions of the focus for which the intensity corresponds to the correct range $[I < I_{max}(0)]$. Emission from Xe^{7+} and Xe^{8+} species having a $4d$ excitation could be expected to originate from the small clusters ($2 \leq n \leq 20$) corresponding to the indicated allowed zone. Anomalous ionization would also be expected, which could possibly produce $Xe^{10+}(4d^8)$, and consequently, through recombination in the plasma, the Xe^{9+} $4d^8 5p \rightarrow 4d^9$ lines at ~150 Å. However, the information shown in Fig. 10 suggests the possibility of another mechanism of production for the $Xe^{9+}(4d^8 5p)$ state.

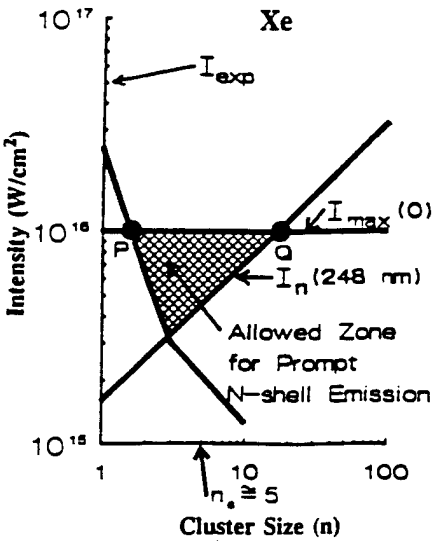

Fig. 10. Expansion of Fig. 5 showing the parameters concerning $4d$-subshell excitation in Xe. The experimental intensity ($I_{exp} \sim 5 \times 10^{16}$ W/cm^2) used in the studies of fluorescence is indicated. The limiting curve I_n(248 nm) is shown. The O-shell limit is taken from Fig. 9 and the allowed zone for prompt N-shell emission is shown. The critical cluster size ($n_c \cong 5$) corresponding to $4d$-shell excitation for the prevailing experimental conditions is indicated

For electrons with a kinetic energy of ~100 eV, the cross section for $4d$ ionization in Xe is unusually high, a feature arising from the shape resonance involving the $5p$, $5s$, and $4d$ shells well known from studies of photoionization and electron collisional ionization in that atom [23–30]. The measurements establish a maximum cross section of $\sigma_{ei} \cong 1.6 \times 10^{-16}$ cm^2 for $4d$ electrons [24]. A comparably high value [23, 31] also holds for ions such as Xe^{2+}. Since the value $Z = 7$ corresponds to the production of Xe^{8+}, we can now evaluate the critical cluster size through (2). With [32] $r_0 = 4.4$ Å, we obtain $n_c \cong 5$, a remarkably small value and one that *matches* the allowed region shown in Fig. 10. Therefore, since the critical cluster size is so small in this case, the production of single $4d$ vacancies can be nearly *saturated* even in relatively small clusters, and the production of *double* vacancies could become significant. Hence, *direct double* vacancy production induced by the intra-cluster mechanism becomes a possibility for the origin of the $Xe^{9+}(4d^8 5p)$ species.

2.3 *Solid-State Studies* (BaF_2)

The results for Xe presented in Fig. 5, with (a) the neglect of the small difference in atomic number separating Xe($Z = 54$) and Ba($Z = 56$), (b) the further neglect of the relatively small difference in atomic spacings, and (c) the assumption that $n \sim 10^3$ corresponds to a cluster having properties approximately those of bulk solid matter, enable us to make contact with data recently obtained in experiments studying X-ray generation from BaF_2 surfaces. The spectra of interest are shown in Figs. 11, 12 and 13. The conditions pertaining to the data shown in Fig. 11 are represented approximately by the point A_x in Fig. 5. Since this point lies at the border of the M-shell allowed zone, it carries the strong implication that anomalous features stemming from the type of direct coupling discussed above may actually be observable in the spectrum obtained with solid BaF_2.

Transitions involving the Ba M-shell arising from this form of interaction would be expected (1) to appear as relatively narrow features, (2) exhibit observable satellite structure due to the distribution of electrons presumably produced in the N-shell of the system during the interaction, and (3) display a considerably different dependence on the conditions of irradiation than the broad quasicontinuum discussed in [33] and [34]. Indeed, an anomalous feature ($\lambda_x = 13.40 \pm 0.05$ Å) exhibiting *all three* of these expected characteristics is seen in Fig. 11. The transition appears to be associated with weak satellite structure and it was found experimentally to be quite sensitive to the conditions of irradiation, a feature illustrated by the comparison of Fig. 11 with Figs. 12 and 13. Higher intensity, corresponding to point B_x in Fig. 5, gives relatively *less* radiation at λ_x, and irradiation with a long (~2 ns) low intensity (< 10^{15} W/cm^2)

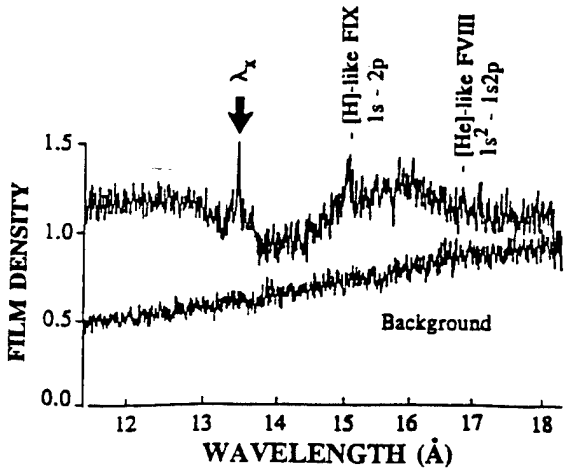

Fig. 11. Spectrum of BaF_2 irradiated with subpicosecond (~270 fs) ultraviolet (248 nm) radiation at a peak intensity of $\sim 8 \times 10^{16}$ W/cm^2 observed with a von Hamos curved crystal spectrometer on a *single* exposure. Occurring along with the Ba M-shell continuum, the F^{8+} L_α(14.98 Å) line and an unidentified feature at 13.40 ± 0.05 Å are seen. These data were recorded in Chicago by A. McPherson and A.P. Shevel'ko. We acknowledge the assistance of P.G. Burkhalter and D.A. Newman of the Naval Research Laboratory in obtaining the densitometer trace of these data. Assuming $n \cong 10^3$, the conditions of these data are represented on Fig. 5 approximately by the point A_x

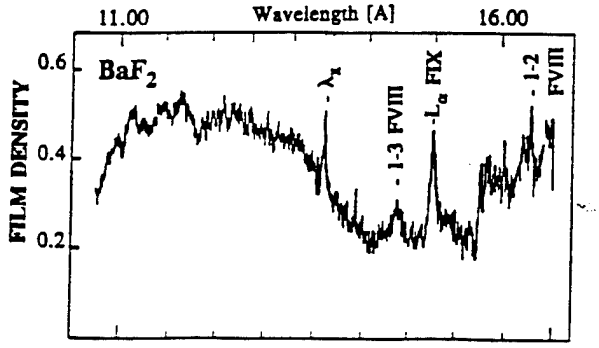

Fig. 12. Spectrum of BaF_2 irradiated as in Fig. 11 except with an incident intensity of $\sim 10^{19}$ W/cm^2. The F^{8+} L_α transition appears stronger, but the unknown λ_x feature has become relatively weakened. These data correspond approximately to point B_x in Fig. 5

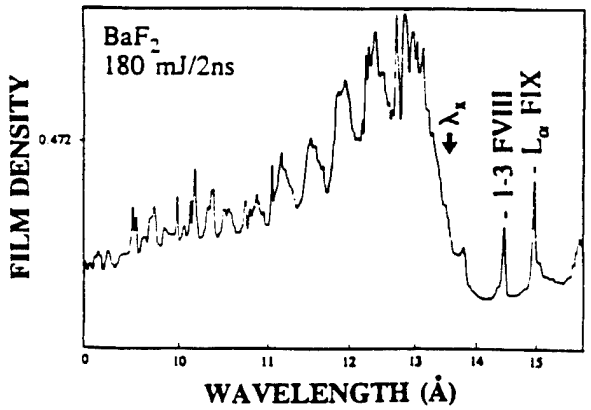

Fig. 13. Spectrum of BaF_2 irradiated by 1.06 μm radiation with a 2 ns pulse length at an intensity $< 10^{15}$ W/cm^2. The M-shell quasicontinuum is present, but the unknown λ_x feature is absent. These data, which were recorded at the Lebedev Physical Institute, Moscow, by A. Shevel'ko and A. McPherson in April 1993, correspond approximately to the region below point C_x in Fig. 5

pulse, corresponding to a position far removed from the M-shell allowed zone in Fig. 5 (region below point C_x), leads to a vanishing of the λ_x line. Finally, theoretical calculations performed by the Moscow group (A. Shevel'ko and coworkers) indicate that λ_x corresponds best to the $3d^{10}4s^2 - 3d^9 4s^2 4f$ transition, a transition whose nature could be expected with the proposed method of coupling by $3d \rightarrow 4f$ excitation through reaction (2).

Two additional comments relevant to the data shown in Fig. 11 can be made. First, the unknown feature λ_x is definitely not weak, since the 9–13 Å continuum [33, 34] against which it must compete, is very strong. Second, if the transition is associated with a direct process of excitation of the nature discussed above, then it can only occur in the early stages of the development of the hot plasma, since the high temperature plasma would quickly lead to full ionization of the N-shell. On the basis of LASNEX simulation [34] of the experiments [33] on Ba in which the electron temperature is calculated, the relevant time appears to be approximately the initial ~50–100 fs of irradiation. It is further implied that the excitation would also be confined to a region quite close to the surface, perhaps in the first skin depth. Hence, such transitions might be able to serve as highly spatially localized probes of the interaction for times sufficiently short that equilibrium conditions cannot be established. Of course, these observations only give a hint at the possibilities, and much further study is needed to verify or deny these hypotheses and possibilities.

3 Implications for X-Ray Amplification

Overall, six previously unexplained or anomalous experimental observations involving three materials (Ar, Kr, and Xe) can be accounted for by the formation of small clusters. In addition, a possible connection with X-ray generation from solids has been made. Furthermore, it can be similarly shown [35] that both the observed [36] production of $2\sigma_g$ excitation in N_2, involving subsequent emission at 55.8 nm, and the anomalous production [37] of U^{10+} from UF_6 are consistent with the picture developed.

In aggregate, these results have two important implications. One involves the possibility of developing a unified picture of high-intensity multiphoton processes applicable for sufficiently short pulses to atoms, molecules, and solids. The second concerns the concept of a *molecular design* for systems optimized for efficient X-ray production and amplification. The latter results from the potential confluence of several favorable factors. They are (1) the inner-shell specificity of the excitation expressed in Figs. 2, 4, 5, and 10, (2) the high efficiency of coupling potentially indicated ($n \sim n_c$), and (3) the ability to combine *simultaneously* the propitious qualities of both high and low density in the dynamic of the medium. The selectivity (1) and the efficiency (2) are consequences of the fact that the electronic motions involved in the coupling occupy only a relatively small fraction of the available phase space. With respect to the latter (3), the use of clusters achieves this paradoxical combination of opposites automatically. Namely, clusters enable atomic excitation rates to achieve the extraordinarily high values characteristic of condensed matter while simultane-

ously eliminating, through local rapid expansion to low particle density, undesirable collisional interactions that would establish equilibrium conditions in the excited material.

The interaction also leads naturally to the production of *inverted* population densities. Consider the case of Ar, as illustrated in Fig. 7, irradiated at an intensity I_γ that is *just below* $I_{max}(M)$. In this circumstance, seven electrons are removed from the M-shell, producing Ar^{7+} with the configuration $1s^2 2s^2 2p^6 3s$, but *no* Ar^{8+} having the configuration $1s^2 2s^2 2p^6$ can be formed. However, as shown in Fig. 4, in $(Ar)_n$ clusters with $n \geq 3$, an L-shell electron can be additionally liberated at the same intensity I_γ with the outcome that Ar^{8+} can be produced, but only with the *excited* configuration $1s^2 2s^2 2p^5 3s$. Furthermore, if we have $n \geq n_c$ *every* atom in the cluster is produced in the excited $(Ar^{8+})^*$ state and *no* ground configuration Ar^{8+} species is formed. Basically, the generation of the ground Ar^{8+} state is totally blocked, but the channel leading to the excited level is fully open. Therefore, in addition to the selective and efficient production of radiation on the $3s \rightarrow 2p$ transition of Ar^{8+}, these dynamics also automatically generate *inverted* population distributions with the capacity for amplification.

Intra-cluster collisional ionization of the M-shell electrons by reaction (3) can potentially destroy the inversion by enabling the generation of Ar^{8+} $1s^2 2s^2 2p^6$ ground state species in the example considered above. However, the use of heavy materials, which exhibit *shape resonances* for inner-shell excitation (e.g. Xe 4*d*) and which have large corresponding cross sections ($\sigma_{ei} \sim 10^{-16}$ cm^2), appears to sharply reduce the significance of such losses. Estimates of the cross section for the loss channel noted above (M-shell collisional ionization), computed for relevant conditions using the Bethe approximation [38], give an estimate of $\sim 10^{-17} - 10^{-18}$ cm^2, so the shape resonances corresponding to inner-shell excitation can still dominate. Basically, this question reduces to the issue of whether ionization cross sections, as a function of energy, can exhibit significant edges with respect to inner-shell excitation. As shown in Figs. 14 and 15, the experimental evidence demonstrates that when the inner-shell interaction involves a shape resonance [31, 39], such edges can be prominent. However, the dynamics of these collisional amplitudes, which will occur when the strong radiative field is present, can only be reliably tested by experiment.

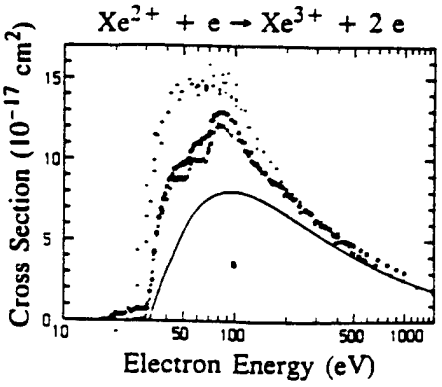

Fig. 14. Single ionization cross sections of Xe^{2+} as a function of electron energy (*solid circles*). Also shown are experimental results of Griffin et al. (X) and Achenbach et al. (+). The curve is the semiempirical calculation using the Lotz formula. Figure and caption taken from [31] which should be consulted for further details. Figure used with permission

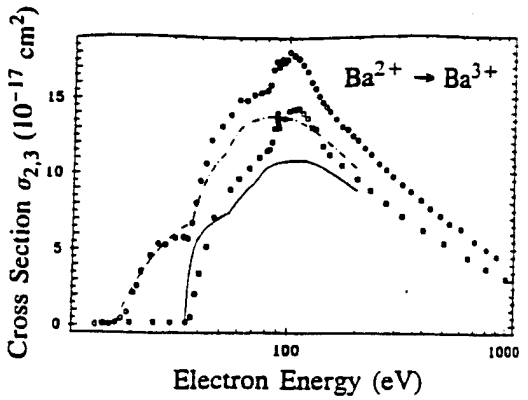

Fig. 15. Absolute cross sections for single ionization of Ba^{2+} ions. *Open squares* represent measurements employing a "cold" Penning ion source (low content of metastable ions in the parent beam); the *open circles* are measurements employing a "hot" ECR ion source (producing a substantial amount of metastable ions in the parent beam). The statistical uncertainties are smaller than the size of the symbols. The *solid line* is a distorted-wave calculation for direct ionization of the 5*p* and 5*s* subshells of ions in the $5s^2 5p^6$ ground-state configuration. The chain curve is a distorted-wave calculation for direct ionization of the 5*p* and 5*s* subshells of ions in the $5s^2 5p^5 5d$ metastable configuration. Figure and caption taken from [39] which should be consulted for further details. Figure used with permission

Auger processes can also generate losses. In this case, the Auger rate depends quite sensitively on the configuration [40], a property that can be used to suppress strongly the Auger decay. For the short pulse excitation (~ 100 fs) being considered, Ar ions with the excited state configurations Ar^{6+} $(1s^2 2s^2 2p^5 3s^2 3p)$, Ar^{7+} $(1s^2 2s^2 2p^5 3s^2)$, Ar^{7+} $(1s^2 2s^2 2p^5 3s 3p)$, and Ar^{8+} $(1s^2 2s^2 2p^5 3s)$ appear to have sufficiently reduced Auger rates. Overall, the figures on both collisional and Auger losses suggest that, in *properly selected systems* undergoing irradiation at an appropriate intensity, the loss channels may be a small fraction ($< 10\%$) of the total excitation.

This situation could lead to very significant levels of amplification. If we assume that the amplifiying X-ray transition is Doppler broadened, on account of the ionic velocity arising from the coulomb explosion, ignore the collisional and Auger loss channels, and take the cluster size $n = n_c$, it can be shown [35] that the gain constant g_λ per unit electron density n_e at wavelength λ_x is given by

$$\frac{g\lambda}{n_e} = \frac{\lambda_x^2}{8\pi Z\sqrt{2}} \frac{A_\lambda}{c} \frac{\sigma_{ei}}{r_0^2} \left(\frac{Mc^2 a_0}{e^2}\right)^{1/2} \left(\frac{r_0}{a_0}\right)^{1/2} \text{cm}^2 \qquad (9)$$

for homonuclear clusters composed of atoms with mass M having an X-ray spontaneous emission rate A_λ. In (9) we have assumed, in order to determine the velocity associated with the Doppler width, that the ion kinetic energy is given by the expression

$$U_i = \frac{Z^2 e^2 n^{2/3}}{r_0} = n^{2/3} Z^2 \frac{e^2}{a_0} \frac{a_0}{r_0}, \qquad (10)$$

a value that can be shown to be the upper bound of possibilities for a uniformly ionized spherical cluster [35]. Table 1

Table 1. Estimated quantities associated with the dynamics of multiphoton excited clusters and soft X-ray amplification. The dominance of Doppler broadening is assumed and $n = n_c$. See text for definitions and details

Material	r_0 [Å]	Transition λ_x [Å]	ε_e [eV]	Z	I_{max} [W/cm^2]	σ_{ei} [cm^2]	n_c	A_λ [s^{-1}]	g_λ/n_e [cm^2]
Ar	3.8	L(3–2) ~ 50	250	7	3×10^{16}	$\sim 1.2 \times 10^{-18}$	$\sim 5 \times 10^5$	1.3×10^{11}	1.9×10^{-19}
Kr	4.0	M(4–3) ~100	210	7	$\sim 2 \times 10^{16}$	$1–3 \times 10^{-17}$	4.4×10^2 -1.2×10^4	$\sim 10^{11}$	$1.3–3.9 \times 10^{-17}$
Br_2	2.3	M(4–3) ~100	184	6	$\sim 2 \times 10^{16}$	$1–3 \times 10^{-17}$	~8 $\sim 2.2 \times 10^2$	$\sim 10^{11}$	$0.3–1.0 \times 10^{-16}$
Xe	4.4	N(5–4) ~150	~140	7	$\sim 10^{16}$	$\sim 1.6 \times 10^{-16}$	~5	5×10^{10}	4.7×10^{-16}
I_2	2.7	N(5–4) ~150	~130	6	$\sim 10^{16}$	$\sim 1.6 \times 10^{-16}$	~1	5×10^{10}	$\sim 10^{-15}$
Xe	4.4	M(4–3) ~ 30	~700	25	6×10^{18}	$\sim 4 \times 10^{-19}$	$\sim 7 \times 10^6$	$\sim 10^{12}$	4.6×10^{-20}
U	2.8	O(6–5) ~100	~200	10	$\sim 2 \times 10^{16}$	$\sim 2 \times 10^{-16}$	~1	$\sim 10^{11}$	$1–3 \times 10^{-15}$
UF_6	~4	O(6–5) ~100	~200	~10	$\sim 2 \times 10^{16}$	$\sim 2 \times 10^{-16}$	~1	$\sim 10^{11}$	$\sim 10^{-15}$
UF_6	~4	N(5–4) ~ 30	~500	~12	$\sim 5 \times 10^{16}$	$\sim 10^{-16}$	~4	$\sim 10^{12}$	$\sim 4 \times 10^{-17}$

presents the estimated quantities for a selected group of materials. It is immediately seen that very favorable conditions for amplification ($g_\lambda \sim 10^2\,\mathrm{cm}^{-1}$) may be achievable for electron densities $n_e < 10^{18}\,\mathrm{cm}^{-3}$ at wavelengths as short as $\lambda_x \cong 100$ Å with the use of subpicosecond excitation.

4 Concept for Molecular Design

A constraint governing the *molecular design* of a system *optimized* for X-ray production can be derived from the conditions expressed in (1), (5), (6), and (7). In general, the allowed zone for prompt X-ray emission from the j-shell of atoms in a homonuclear cluster appears as a triangular region of the kind illustrated in Fig. 16. If we identify the

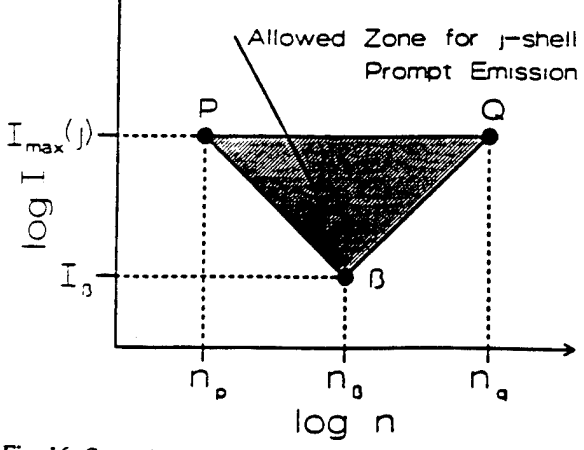

Fig. 16. General representation of the allowed zone for prompt j-shell emission from a homonuclear cluster as a function of intensity (I) and cluster size n. The three constraints arising from (1), (6), and (7) are shown along with the vertex β having coordinates (n_β, I_β). The diagram is similar to that shown for the Xe N-shell in Fig. 10

optimization of the system with (1) the utilization of the lowest possible intensity and (2) excitation of the cluster under conditions of maximal amplification per unit density, then the vertex β defines that optimum subject to the subsidiary condition $n_\beta = n_c$. An explicit statement for this situation can be easily found. From equality of (6) and (7), we find

$$n_\beta^{4/3} = \left(\frac{\lambda}{2\pi r_0}\right)^4 \left(\frac{\varepsilon_e}{mc^2}\right)^2, \tag{11}$$

an expression, which, when combined with the condition $n_\beta = n_c$ with the use of (5), gives the result

$$\frac{\varepsilon_e}{mc^2}\left(\frac{Z\sigma_{ei}\lambda}{2\pi r_0^3}\right)^2 = 1. \tag{12}$$

Finally, if the factor Z is represented by setting $I_\beta = I_{th}$ from (1), then the overall expression

$$\frac{1}{128\pi\alpha^3}\left(\frac{E_p}{mc^2}\right)^2 \frac{E_p^2}{\lambda_c^2 \hbar I_\beta} \frac{\varepsilon_e}{mc^2}\left(\frac{\sigma_{ei}\lambda}{2\pi r_0^3}\right)^2 = 1 \tag{13}$$

is found, a statement which relates (1) the atomic properties (ε_e, E_p, σ_{ei}), (2) the molecular structure constant (r_0), and (3) the parameters describing the irradiation (I_β, λ). Although not fully establishing any particular molecular configuration, (13) *explicitly illustrates the relative dependencies* of these important variables with respect to the optimum condition.

5 Conclusions

A unified picture of high-intensity multiphoton processes, involving atoms, molecules, and solids, may be developed through the study of clusters. Of particular significance are possible intra-cluster processes that can influence the level of ionization produced and lead to the excitation of inner-shell states with the subsequent generation of prompt X-rays.

The behavior of shape resonances [41] characteristic of inelastic electron scattering processes, particularly for ionized systems [42] for which rather little is known, feature prominently in the dynamics. Overall, at least six previously unexplained or anomalous experimental observations involving three materials find interpretations consistent with the physical picture developed. It is considered significant that this synthesis can be achieved with the exclusive use of known atomic and molecular properties.

The definition of a critical cluster size $n_c = (r_0^2/Z\sigma_{ei})^3$ for inner-shell excitation highlights the complexity of the relationships governing the coupling by combining (1) a static structural factor (r_0), (2) a dynamical consideration involving inelastic electron collisional processes (σ_{ei}), and (3) the nonlinearity of the interaction with the strength of the radiation field, which is implicitly represented by the factor Z.

The general result is that molecular systems and clusters *intrinsically* have properties making them considerably more suitable than atoms for the production of X-ray emission through the mechanism of multiphoton coupling at high field strengths. This outcome creates the possibility of *designing* molecules [43] optimized for efficient X-ray production at selected wavelengths and provides a general method for the generation of nonequilibrium distributions of excited states suitable for X-ray amplification. If this can be accomplished, a class of presently unknown molecular materials is likely to emerge. Presently, since the available clues indicate that heavy atoms are strongly favored, such materials may possibly be related to metallic clusters [1], giant molecules [44] involving atoms such as Au, Pb, Th, and U, and systems incorporating rare earth atoms [45, 46] or transition metals [47].

Acknowledgements. The authors acknowledge the expert technical assistance of J. Wright and P. Noel and the valued scientific collaboration of A.P. Shevelko. Helpful discussions are acknowledged by C.K. Rhodes with J. Solem, E.W. Schlag, K. Müller-Dethlefs, R. Jung, W. Waterstradt, J. Dietrich, J. Belling, E. Grant, W. Sandner, and U. Becker. Support for this research was provided under contracts (DoE) DE-FG 91ER1208, AFOSR-89-0159, (ONR) N00014-91-J-1106, (SDIO) N00014-91-K-2013, and (ARO) DAAL 3-91-G-0174. Partial support was also provided by the Alexander von Humboldt Stiftung.

References

1. *Small particles and Inorganic Clusters. Proc. of the Fifth Int'l Meeting on Small Particles and Inorganic Clusters.* Z. Phys. D **19**. No. 1–4 (1991); Z. Phys. D **20**. No. 1–4 (1991)
2. P.H.Y. Lee, D.E. Casperson, G.T. Schappert: Search for Multiphoton-Induced Inner-Shell Excitation. Phys. Rev. A **40**. 1363 (1989)
3. G. Gibson, R. Rosman, T.S. Luk, I.A. McIntyre, A. McPherson, G. Wendin, K. Boyer, C.K. Rhodes: Characteristics of a Non-Equilibrium Picosecond Laser Plasma. In *Short Wavelength Coherent Radiation: Generation and Applications*, Vol. 2, ed. by R.W. Falcone, J. Kirz (Optical Society of America, Washington, D.C. 1988) p. 246
4. A. McPherson, T.S. Luk, G. Gibson, J.C. Solem, K. Boyer, C.K. Rhodes: Studies of Strong-Field Effects in Multiphoton Subpicosecond Excited Plasmas: Soft X-Ray Fluorescence and Propagation. In *Fundamentals of Laser Interactions II*, ed. by F. Ehlotzky, Lect. Notes Phys., Vol. 339, (Springer, Berlin, Heidelberg 1989) p. 93
5. M.A. Preston: *Physics of the Nucleus* (Addison-Wesley, Reading, MA 1962)
6. W.A. Saunders, N. Dam: Liquid Drop Model of Multiply Charged Metal Cluster Fission. Z. Phys. **20**. 111 (1991)
7. S. Augst, D. Strickland, D.D. Meyerhofer, S.L. Chin, J.H. Eberly: Tunneling Ionization of Noble Gases in a High-Intensity Laser Field. Phys. Rev. Lett. **63**, 2212 (1989)
8. G.N. Gibson, T.S. Luk, C.K. Rhodes: Tunneling Ionization in the Multiphoton Regime. Phys. Rev. A **41**. 5049 (1990)
9. T.A. Carlson, C.W. Nestor, Jr., N. Wassermann, J.D. McDowell: Calculated Ionization Potentials for Multiply Charged Ions. At. Data **2**. 63 (1970)
10. K-N. Huang, M. Aoyagi, M.H. Chen, B. Crasemann, H. Mark: Neutral-Atom Electron Binding Energies from Relaxed-Orbital Relativistic Hartree-Fock-Slater Calculation. At. Data Nucl. Data Tables **18**. 243 (1976)
11. A. McPherson, G. Gibson, H. Jara, U. Johann, T.S. Luk, I.A. McIntyre, K. Boyer, C.K. Rhodes: Studies of Multiphoton Production of Vacuum-Ultraviolet Radiation in the Rare Gases. J. Opt. Soc. Am. B **4**. 595 (1987)
12. L.A. Jones, E. Källne: A Study of the VUV Emission from Highly Ionized Krypton in a Theta Pinch Plasma. J. Quant. Spectrosc. Radiat. Transfer **30**. 317 (1983)
13. Y. Morioka, H. Masuda, Y. Lu, K. Tanaka, T. Hayaishi: Threshold Photoelectron and TOF Photoelectron Spectra of Ar_2^+ and Kr_2^+. J. Phys. B **25**, 5343 (1992)
14. S.T. Pratt, P. Dehmer: Photoionization of the Kr_2 Dimer. Chem. Phys. Lett. **87**, 533 (1982)
15. O.F. Hagena: Cluster Ion Sources. Rev. Sci. Instrum. **63**, 2375 (1992)
16. R.L. Kelly: Atomic and Ionic Spectrum Lines below 2000 Angstroms: Hydrogen through Krypton Part I (H-Cr). J. Phys. Chem. Ref. Data, **16**, Suppl. 1, 1 (1987)
17. Y. Zhang, C.B. Reddy, R.S. Smith, D.E. Golden, D.W. Mueller, D.C. Gregory: Measurement of Electron-Impact Single-Ionization Cross Sections of Ar^{8+}. Phys. Rev. A **44**, 4368 (1991)
18. C.K. Rhodes: Physical Processes at High Field Strengths. Phys. Scri. T **17**. 193 (1987)
19. J.R. Roberts, E.J. Krystautas, J. Sugar: One-Electron Spectrum of Xe VIII. J. Opt. Soc. Am. **69**. 1620 (1979)
20. V. Kaufman, J. Sugar: Ag I-Like Array $4d^{10}5s - 4d^9 5s5p$ of I VII through Eu XVII. J. Opt. Soc. Am. B **1**. 38 (1984)
V. Kaufman, J. Sugar, J.L. Tech: Analysis of the $4d^9 - 4d^8 5p$ Transitions in Nine-Times Ionized Xenon (Xe X). J. Opt. Soc. Am. **73**. 691 (1983)
21. J. Blackburn, P.K. Carroll, J. Costello, G. O'Sullivan: Spectra of Xe VII and IX in the Extreme Ultraviolet: $4d - mp$, nf Transitions. J. Opt. Soc. Am. **73**. 1325 (1983)
22. P.M. Dehmer, S.T. Pratt, J.L. Dehmer: Photoelectron Spectra of Xe_2 Obtained by Resonantly Enhanced Multiphoton Ionization. J. Phys. Chem. **91**. 2593 (1987)
23. M.J. Higgins, M.A. Lennon, J.G. Hughes, K.L. Bell, H.B. Gilbody, A.E. Kingston, F.J. Smith: *Atomic and Molecular Data for Fusion. Part 3*. Recommended Cross Sections and Rates for Electron Impact Ionization of Atoms and Ions: Copper to Uranium, Culham Report, CLM-R294 (Abingdon, Oxfordshire, UK 1989)
24. D. Mathur, C. Badrinathan: Ionization of Xenon by Electrons: Partial Cross Sections for Single, Double, and Triple Ionization. Phys. Rev. A **35**, 1033 (1987)
25. S. Southworth, U. Becker, C.M. Truesdale, P.H. Kobrin, D.W. Lindle, S. Owaki, D.A. Shirley: Electron-Spectroscopy Study of Inner-Shell Photoexcitation and Ionization of Xe. Phys. Rev. A **28**. 261 (1983)
26. H. Aksela, S. Aksela, G.M. Bancroft, K.H. Tan, H. Pulkkinen: $N_{4,5}OO$ Resonance Auger Spectra of Xe Studied with Selective Excitation by Synchrotron Radiation. Phys. Rev. A **33**. 3867 (1986)
27. U. Becker, T. Prescher, E. Schmidt, B. Sonntag, H.-E. Wetzel: Decay Channels of the Discrete and Continuum *Xe* 4*d* Resonances. Phys. Rev. A **33**. 3891 (1986)

28. U. Becker, R. Hölzel, H.G. Kerkhoff, B. Langer, D. Szostak, R. Wehlitz: Zerfälle der $Xe4d$ — np Anregungen: Resonante Auger- und Doppel-Auger-Prozesse. BESSY, Bericht (1984)
29. A.F. Starace: Atomic Photoionization. In *Fundamental Processes in Energetic Atomic Collisions*, ed. by H.O. Lutz, J.S. Briggs, H. Kleinpoppen (Plenum, New York 1983) p. 69
A.F. Starace: Theory of Atomic Photoionization. Handb. Phys. **31**, 1 (1982)
30. M.Ya. Amusia, N.A. Cherepkov: Many-Electron Correlations in Scattering Processes, in *Case Studies in Atomic Physics 5*, ed. by E.W. McDaniel, M.R. McDowell (North-Holland, Amsterdam 1975) p. 47
31. A. Matsumoto, A. Danjo, S. Ohtani, H. Suzuki, H. Tawara, T. Takayanagi, K. Wakiya, I. Yamada, M. Yoshino, T. Hirayama: Measurements of Absolute Cross Sections for Electron-Impact Ionization of Doubly Charged Rare Gas Ions. Ne^{2+}, Ar^{2+}, Kr^{2+}, and Xe^{2+}. J. Phys. Soc. Jpn **59**, 902 (1990)
32. K.P. Huber, G. Herzberg: *Molecular Spectra and Molecular Structure IV. Constants of Diatomic Molecules* (Von Nostrand Reinhold, New York 1979)
33. A. Ziegler, P. G. Burkhalter, D.J. Nagel, K. Boyer, T.S. Luk, A. McPherson, J.C. Solem, C.K. Rhodes: High Intensity Generation of 9-13 Å X-Rays from BaF_2 Targets. Appl. Phys. Lett. **59**, 777 (1991)
34. W.H. Goldstein, A. Zigler, P.G. Burkhalter, D.J. Nagel, A. Bar-Shalom, J. Oreg, T.S. Luk, A. McPherson, C.K. Rhodes: X-Ray Emission from a 650 Femtosecond Laser-Produced Barium Plasma. Phys. Rev. E **47**, 4349 (1993)
35. C.K. Rhodes: Multiphoton-Induced X-Ray and Ion Emission from Clusters: Unified Analysis of Strong-Field Interactions in Atoms, Molecules, and Solids. Laboratory Memorandum, (January 1993)
36. G. Gibson, T.S. Luk, A. McPherson, K. Boyer, C.K. Rhodes: Observation of a New Inner-Orbital Molecular Transition at 55.8 nm in N_2^{2+} Produced by Multiphoton Coupling. Phys. Rev. A **40**, 2378 (1989)
37. T.S. Luk, H. Pummer, K. Boyer, M. Shahidi, H. Egger, C.K. Rhodes: Anomalous Collision-Free Multiple Ionization of Atoms with Intense Picosecond Ultraviolet Radiation. Phys. Rev. Lett. **51**, 110 (1983)
38. M. Inokuti: Inelastic Collisions of Fast Charged Particles with Atoms and Molecules – The Bethe Theory Revisited. Rev. Mod. Phys. **43**, 297 (1971)
39. K. Tinschert, A. Müller, G. Hofmann, E. Salzborn, S.M. Younger: Electron-Impact Single and Double Ionization of Ba^{2+} and Ba^{3+} Ions. Phys. Rev. A **43**, 3522 (1991)
40. F.P. Larkins: Dependence of Fluorescence Yield on Atomic Configuration. J. Phys. B **4**, L29 (1971)
41. J.P. Connerade, J.M. Esteva, R.C. Karnatak: *Giant Resonances in Atoms, Molecules, and Solids*, NATO ASI Series B, Physics Vol. 151 (Plenum, New York 1987)
42. D.C. Griffin, C. Bottcher, M.S. Pindzola, S.M. Younger, P.C. Gregory, P.H. Crandall: Electron-Impact Ionization in the Xenon Isonuclear Sequence. Phys. Rev. A **29**, 1729 (1984)
43. T.S. Luk, A. McPherson, G.N. Gibson, K. Boyer, C.K. Rhodes: Molecular X-Ray Laser Research. Izv. Acad. Nauk. Ser. Fiz. T. **55**, 768 (1991) (in Russian); English translation in *Short Wavelength Lasers and Their Applications*, ed. by V.V. Korobkin, M.Yu. Romanovsky (Nova, Commack, New York 1992) p. 1
44. J.M. van Ruitenbeek, M.J.G.M. Jurgens, G. Schmid, D.A. van Leeuwen, H.W. Zandbergen, L.J. de Jongh: Metallic Susceptibility in a Giant Molecule: $Pd_{561}Phen_{36}O_{200}$. Z. Phys. D **19**, 267 (1991)
45. D. Rayane, A. Benamar, P. Melinon, B. Tribollet, M. Broyer: Structure of Small Rare Earth Clusters: Z. Phys. D **19**, 191 (1991)
46. C. Bréchignac, Ph. Cahuzac, F. Carlier, M. de Frutos, A. Masson, J.Ph. Roux: Generation of Rare Earth Metal Clusters by Means of the Gas-Aggregation Technique. Z. Phys. D **19**, 195 (1991)
47. G. Schmid: Developments in Transition Metal Chemistry – The Way to Large Clusters. In *Clusters*, Structure and Bonding, Vol. 62 (Springer, Berlin, Heidelberg 1985) p. 51

Appendix B: "Multiphoton Induced X-Ray Emission from Kr Clusters on *M*-Shell (~ 100 Å) and *L*-Shell (~ 6 Å) Transitions"

Multiphoton Induced X-Ray Emission from Kr Clusters on M-Shell (−100 Å) and L-Shell (−6 Å) Transitions

A. McPherson, T. S. Luk, B. D. Thompson, A. B. Borisov, O. B. Shiryaev, X. Chen, K. Boyer, and C. K. Rhodes

Laboratory for Atomic, Molecular, and Radiation Physics, Department of Physics, M/C 273, University of Illinois at Chicago, 845 W. Taylor, Room 2136, Chicago, Illinois 60607-7059

(Received 2 September 1993; revised manuscript received 28 December 1993)

Experiments demonstrating the role of cluster formation on multiphoton-induced x-ray emission and the scaling of this phenomenon into the kilovolt range have been performed on Kr. For the Kr M shell, augmentation of Kr_n formation leads to a large increase in Kr^{9+} ($4p \rightarrow 3d$) emission (−100 Å) and the appearance of a strong band at −90 Å. The observation of L-shell transitions (−5–7.5 Å) demonstrates the scaling of this phenomenon into the kilovolt region and leads to the conclusion that the interaction produces direct inner-shell excitation with the emission of prompt x rays.

PACS numbers: 32.80.Wr, 32.30.Rj

It has been postulated [1] that a unified picture of high-intensity short-pulse multiphoton processes, embracing atoms, molecules, and solids, appears possible through the study of atomic and molecular clusters. Of particular significance in this analysis are *intracluster* processes involving inelastic electron collisions of the form

$$e^- + X \xrightarrow{\sigma_n} e^- + e^- + (X^+)^* \qquad (1)$$

that can lead to the production of inner-shell excited species capable of prompt x-ray emission.

Essential predictions of the proposed model have been explicitly tested in new experimental studies involving five atomic shells [Kr(M), Kr(L), Xe(N), Xe(M), and Xe(L)]. This Letter establishes the crucial role of cluster formation in the generation of the anomalous emissions previously observed [2–4] from the Kr M shell (−110 eV) and demonstrates the scaling of this new phenomenon into the kilovolt range (−800–2100 eV) through measurements of Kr L-shell radiation.

The detection of intense Kr^{9+} ($4p \rightarrow 3d$) emission at −100 Å in earlier spectroscopic studies [2,3] using pulsed-gas targets presented an obvious paradox. Measurements of ion production [5] using tenuous gas targets, conducted under identical conditions of irradiation, had demonstrated that *no* production of Kr^{9+} was possible from free Kr atoms. Hence, the identification [6,7] of the Kr^{9+} emissions, produced by either a prompt or a delayed mechanism, was fully anomalous. However, if sufficient cluster formation were produced in the hydrodynamic flow of the jet furnishing the target [2–4], the cluster model showed that this paradox could be entirely resolved; the anomalous emissions found a simple explanation which applied generally to all cases considered [1].

The multiphoton-induced production of prompt short wavelength radiation from clusters requires that certain conditions be met [1]. These requirements establish relationships between the intensity of irradiation (I) and the cluster size (n) which define allowed zones for the emission to occur. Such emission can only take place if sufficient kinetic energy is possessed by the colliding electron in reaction (1) to excite an inner electron. This condition, based on a simple formulation of the work done by the external field on a free electron in the cluster, leads to the specification of two limiting intensities given by

$$I_0 = \frac{\epsilon_e^2}{8\pi a n^{2/3} \hbar r_0^2}, \qquad I_n(\lambda) = \frac{2\pi^3}{a}\left(\frac{r_0}{\lambda}\right)^2 mc^2 \left(\frac{c}{\lambda_c}\right)\frac{n^{2/3}}{\lambda^2}, \qquad (2)$$

in which ϵ_e, r_0, a, λ, m, λ_c, and c denote the inner-shell binding energy [8], the interatomic spacing, the fine structure constant, the wavelength of irradiation, the electron mass, the electron Compton wavelength, and the speed of light, respectively. Hence, an inner-shell $j-1$ electron with binding energy ϵ_e can be ionized if the intensity exceeds a *lower bound* given by either I_0 or $I_n(\lambda)$, whichever is greatest. In addition to the production of a vacancy in the $j-1$ shell, *prompt* $j \rightarrow j-1$ emission requires the retention of at least one electron in the outer j shell during the course of irradiation. This determines an *upper bound* on the intensity which, with the use of the tunneling ionization model [9], leads to a limiting intensity $I_{max}(j)$ given by

$$I_{max}(j) = cE_p^4(j)/128\pi e^6 Z^2, \qquad (3)$$

where $E_p(j)$ is the ionization potential of the most tightly bound j-shell electron, Z the resulting ionic charge, and e the electronic charge. Hence, the allowed zones for prompt x-ray emission from atoms of a homonuclear cluster generally appear in the form shown for the Kr M and L shells in Fig. 1.

This picture leads to the prediction that an increase in the cluster density and average cluster size should lead to both a corresponding *intensification* and a spectral *modification* of the detected emission. Since Kr_n cluster formation can be strongly augmented by cooling the flow

0031-9007/94/72(12)/1810(4)$06.00

in the jet [10,11], in light of the form of the allowed zone for the M shell in Fig. 1, a comparison of spectra observed at comparable pressures (densities) and substantially different temperatures should indicate the importance of the role of cluster species in the production of the radiating ions.

The experimental apparatus used has been described elsewhere [3]. The laser [12] employed in the present study, which had a wavelength of 248 nm, a pulse width of $\sim$300 fs, and a power of $\sim$0.7 TW, was focused with an $f/10$ CaF_2 lens into the gas target and provided a maximum focal intensity of $(0.5-1.0)\times10^{17}$ W/cm^2, conditions essentially the same as in the previous work [2–4]. The gas target was produced by a high-pressure pulsed valve fitted with a circular sonic nozzle having a diameter of 0.5 mm. The gas flow was cooled with free-flowing dry nitrogen which had passed through a liquid nitrogen bath. A thermocouple attached to the valve body measured the temperature of the gas and a grazing incidence spectrometer was used to record the spectra [2–4].

The relevant spectral comparison for Kr in the 72–112 Å region is presented in Fig. 2. The Kr spectrum illustrated in Fig. 2(a) was obtained with a stagnation pressure of 115 psia at 293 K, conditions very similar to those of the earlier work [2,3]. Figure 2(b) presents the Kr spectrum corresponding to a significantly reduced nozzle temperature (238 K) and a stagnation pressure (130 psia), nearly the same as that pertaining to the data in Fig. 2(a).

Three principal differences distinguish the spectra shown in Figs. 2(a) and 2(b). They are (1) a large increase in the observed Kr^{9+} $(4p\rightarrow3d)$ signal upon reduction of the temperature (e.g., from $\sim$30 to $\sim$450 at $\sim$103 Å), (2) the appearance of a strong highly structured band at 90 Å at the lower temperature, and (3) the large relative reduction in Fig. 2(b) of the narrow features appearing in the 72–83 Å region of Fig. 2(a). Spectral data [6,7] indicate that the features observed in Fig. 2(b) in the 86–97 Å region arise from Kr^{10+} $(4p\rightarrow3d)$ transitions in the $\sim$86–91 Å range and Kr^{9+} $(4s4p\rightarrow4s3d)$ lines in the $\sim$90–97 Å interval. A contribution from $3p$ excitation in both Kr^{9+} and Kr^{10+} may occur in this same region. The spectrum also gives evidence for the presence of a broad unresolved band in the $\sim$76–85 Å region composed of dense arrays [6] originating from Kr^{10+} $(4s4p\rightarrow4s3d)$ and Kr^{11+} $(4p\rightarrow3d)$ transitions.

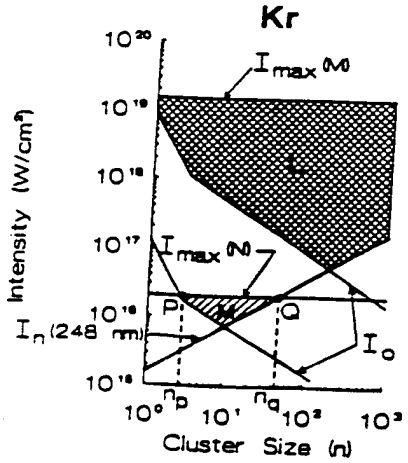

FIG. 1. Representation of the allowed zones for production of prompt Kr M- and L-shell emission from Kr clusters as a function of the intensity of 248 nm irradiation and cluster size. The boundaries outlining the allowed region are defined in the text. The maximum experimental intensities used for the M-shell and L-shell studies correspond to 1.0×10^{17} W/cm^2 and $\sim8\times10^{18}$ W/cm^2, respectively.

These two signatures, a sharply increased signal strength and the appearance of new categories of transitions and higher charge states, are precisely the outcomes anticipated from enhanced cluster formation [1]. One expects that a higher cluster (Kr_n) density for fixed n would cause a corresponding increase in the emission and that the formation of larger clusters would lead to a further intensification of the emission and to new stages of ionization and classes of transitions. Since the 90 Å band only appeared in the cooled spectrum, we believe that it is mainly associated with the formation of the larger clusters produced at the lower temperature (238 K).

Figure 2(a) also exhibits the clear visibility of relatively weak narrow transitions in the $\sim$72–83 Å region which can be associated with $4f\rightarrow3d$ transitions [7] in Kr^{8+}. In distinct contrast to the lines in the 85–104 Å range, these features do *not grow* dramatically as the temperature is decreased. They remain weak and become relatively insignificant as the temperature is reduced. This sharply contrasting behavior indicates the action of a *different* mechanism for their excitation. Since the two spectra shown in Fig. 2 were generated under essentially the same *average* plasma conditions, conventional collisional mechanisms, such as recombination, should occur in largely the same fashion in both cases. This expectation matches the observed behavior of the transitions associated with $4f$ orbital excitation and we attribute those weak features to recombination.

The cluster model predicts the existence of large allowed regions associated with level structures in the kilovolt range, a property manifest in Fig. 1 through comparison of the zones associated with the M and L shells. Specifically, the model [1] predicts that the irradiation of Kr clusters with intensities above $\sim10^{18}$ W/cm^2, for nearly an arbitrary cluster distribution, should result in emission of prompt x rays from L-shell transitions [7, 13,14] in Kr ions ($\sim$7 Å).

Experiments testing this scaling behavior have been conducted with a peak intensity of $\sim8\times10^{18}$ W/cm^2. In this case, the focusing was provided by an $f/3$ off-axis parabolic mirror and a crystal spectrometer, using Kodak Industrex film and PET for the 4.5–7.5 range, was used.

The L-shell emission spectrum of Kr shown in Fig. 3, which involves transitions [7,13,14] from Kr^{q+} ($q=24-$

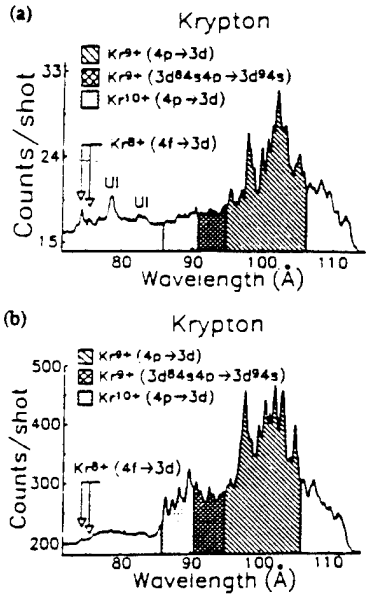

FIG. 2. Comparison of Kr spectra in the 72–112 Å region produced at different temperatures by multiphoton excitation with subpicosecond irradiation at 248 nm with a maximum intensity of $(0.5–1.0)\times10^{17}$ W/cm^2. The vertical scales in both spectra are absolute values giving a valid measure of the comparative signal strengths. The spectral resolution is 0.9 ± 0.1 Å. (a) Nozzle temperature 293 K and stagnation pressure 115 psia. UI designates unidentified transitions. The base line corresponds to ~17 counts/shot. (b) Nozzle temperature 238 K and stagnation pressure 130 psia. Unresolved arrays from Kr^{10+} and Kr^{11+} may contribute to the signal in the ~76–85 Å region.

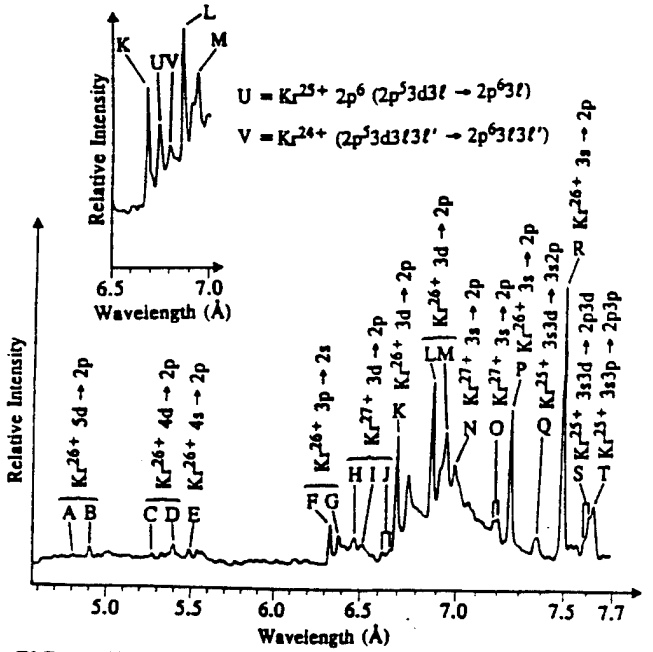

FIG. 3. Kr L-shell emission spectrum produced by multiphoton excitation with 248 nm radiation at a peak intensity of -8×10^{18} W/cm^2. The stagnation pressure of the pulsed jet was 115 psia and the gas temperature was 243 K. Transitions from Kr^{q+} ($q=24–27$) are identified. The inset, presenting data from another exposure, details the 6.5–7.0 Å region and shows the prominent $Kr^{24+}(V)$ and $Kr^{25+}(U)$ satellite lines observed in these experiments.

27) in the 4.5–7.5 Å region, was recorded with 720 laser pulses. This spectrum exhibits several salient properties: (1) a group of strong $3l\rightarrow2l'$ lines in the 6.3–7.7 Å region, (2) a small set of far weaker $4l,5l\rightarrow2p$ transitions in the 4.8–5.6 Å region, (3) lines with significant strength having $2s$ excitation (e.g., F), and (4) a substantial number of transitions involving satellite lines [14] [e.g., $Rk^{24+}(V/2p^63l3l'\rightarrow2p^53d3l3l')$ and $Kr^{25+}(U/2p^63l\rightarrow2p^53d3l)$ shown in the inset].

Several considerations bear directly on the interpretation of these data. First, the radiating charge states are anomalous. In analogy with the Kr^{9+} transitions discussed above, the presence of lines from Kr^{q+} ($q=24–27$) is equally anomalous, since the tunneling ionization picture [5,9] predicts no charge states higher than Kr^{22+}. Second, the radiative transitions are fast. The lifetimes [15] of the $3s\rightarrow2p$, $3d\rightarrow2p$, and $3p\rightarrow2s$ transitions occurring in the ~6–7 Å region fall largely in the 10–1000 fs range and the $2p\rightarrow2s$ (~200 eV) transition [7] has a lifetime [16,17] less than 10 ps. Third, recombination and plasma collisional processes are relatively slow. Considering the properties of the flow, the relative positions of the focal zone and the nozzle, and the level of ionization ($Z\cong25$), the maximum average electron density [4] is $\sim5\times10^{20}$ cm^{-3}. This gives a rate less than 10^{10} s^{-1} for both recombination [18] and $2s\rightarrow2p$ collisional excitation [16].

In light of these considerations, the experimental observations lead to the following interpretations. The five weak transitions (A–E) associated with Kr^{26+} all involve transitions of the form $nl\rightarrow2p$ with $n\geq4$. Since the N-shell limit [$I_{max}(N)$] falls *entirely* below the allowed L-shell zone in Fig. 1, the postulated cluster mechanism cannot account for the presence of these lines. In analogy with the weak $4f\rightarrow3d$ features occurring in Fig. 2(a), these lines are attributed to recombination from Kr^{27+}, a species identified by transitions (H,I,J,N,O).

The strong lines observed in the 6.3–7.7 Å region uniformly involve transitions with $3s$, $3p$, or $3d$ electrons. Using the most weakly bound of these ($3d$), and combining the information in Fig. 1 with the conditions for tunneling ionization [1,9], we can estimate the minimum cluster size necessary to observe L-shell ionization and still retain a $3d$ electron. Since the maximum intensity consistent with the retention of a $3d$ electron is $\sim2\times10^{18}$ W/cm^2, the L-shell zone indicates that clusters with $n\geq3$ would suffice. Evidence [10,11] on Kr_n formation indicates that an appreciable density with sizes at least as large as $n\sim10$ is formed under our experimental conditions.

Lines F and G involve $2s$ excitation in Kr^{26+}. Since $2p\rightarrow2s$ radiative decay is fast and electron collisional communication between the $2s$ and $2p$ states is slow, the

formation of Kr^{26+} $2s2p^63p$ levels by recombination from excited $2s2p^6$ Kr^{27+} ions would have to be rapid. However, since the plasma conditions cannot support a recombination rate comparable to the radiative decay, it follows that the Kr^{26+} excited states are *directly* produced in the excitation of the cluster. The same reasoning and conclusion hold in relation to the $3d \rightarrow 2p$ satellite lines [e.g., $Kr^{24+}(V)$ and $Kr^{25+}(U)$].

The comparison of the spectrum illustrated in Fig. 3 with corresponding data obtained with a Z pinch [13] reveals a relative abundance of satellite lines in the multiphoton spectrum and significant reversals in relative line intensities. Both observations are in natural accord with the cluster model. The strong appearance of satellite transitions in the multiphoton spectrum [e.g., $Kr^{24+}(V)$], at the relatively low average electron density characteristic of this experiment, is again indicative of a direct mechanism of production [1] in the cluster which can be associated with the existence of the allowed L-shell region. In the 6.3–7.7 Å region, the multiphoton $(m\gamma)$ $3s \rightarrow 2p$ transitions consistently exhibit the anomalous property of having a greater intensity than the corresponding $3d \rightarrow 2p$ lines, while the reverse holds for the Z-pinch (Z) spectrum [13]. Specifically, for Kr^{26+} $R > L$ $(m\gamma)$, $R < L$ (Z) and for Kr^{27+} $N > J$ $(m\gamma)$, $N < J$ (Z). Recombining collisionally dominated optically thin plasmas characteristically produce emission with $nd \rightarrow 2p$ transitions dominating [19] the corresponding $ns \rightarrow 2p$ lines.

The anomalous strength of the $3s$ transitions congenially matches the expectations of the cluster picture. Electron loss can occur by tunneling ionization and intracluster inelastic electron collisions. With a maximum intensity of 8×10^{18} W/cm^2, $3s$ electrons *cannot* be removed by the tunneling process [9], although the full $3d$ shell is ionized for intensities $> 2\times10^{18}$ W/cm^2. Collisionally, since the $3d$ ionization cross section [20,21] is approximately tenfold the value for the $3s$ level, retention of the $3s$ electron is again favored. It follows that in the region corresponding to L-shell excitation, particularly for intensities above $\sim10^{18}$ W/cm^2, a higher probability exists for retention of $3s$ electrons than for $3d$. This tendency should also be enhanced for the higher charge states seen, assuming a greater intensity for their production. Namely, the $3s/3d$ ratio should be greater for Kr^{27+} than for Kr^{26+}, a feature that is reflected in the multiphoton data $(N/J > R/L)$.

In summary, experimental studies of multiphoton-induced emissions in the 5–7.5 Å region from Kr have established that the cluster mechanism demonstrated in the $\sim$80–110 eV range scales into the kilovolt zone. The experimental evidence supports the conclusion that multiphoton coupling to clusters can *directly* generate inner-shell vacancies and the production of *prompt* x rays. Finally, recent measurements [22] demonstrating the multiphoton production of Xe(L) emission further corroborate this conclusion.

The authors acknowledge the expert technical assistance of J. Wright and P. Noel and extend special thanks to S. Guggenheim for the use of his densitometer. Helpful discussions are acknowledged (C.K.R.) with J. C. Solem, E. W. Schlag, K. Müller-Dethlefs, R. Jung, E. Waterstradt, H-J. Dietrich, J. Belling, E. Grant, W. Sandner, U. Becker, J. Sugar, R. D. Cowen, R. B. Spielman, and R. E. Stewart. Support for this research was provided under Contracts No. (DOE) DE-FG02-91ER1208, No. AFOSR-89-0159, (ONR) No. N00014-91-J-1106, (SDI/NRL) No. N00014-91-K-2113, and (ARO) No. DAAL 3-91-G-0174. Partial support (C.K.R.) was provided by the Alexander von Humboldt Stiftung.

[1] A. McPherson *et al.*, Appl. Phys. B **57**, 337 (1993).
[2] A. McPherson *et al.*, in *Fundamentals of Laser Interactions II*, edited by F. Ehlotzky (Springer-Verlag, Berlin, 1989), p. 93.
[3] A. McPherson *et al.*, J. Opt. Soc. Am. B **4**, 595 (1987).
[4] G. Gibson *et al.*, in *Short Wavelength Coherent Radiation: Generation and Applications*, edited by R. W. Falcone and J. Kirz (Optical Society of America, Washington, D.C., 1988), Vol. 2, p. 246.
[5] G. N. Gibson, T. S. Luk, and C. K. Rhodes, Phys. Rev. A **41**, 5049 (1990).
[6] L. A. Jones and E. Källne, J. Quant. Spectrosc. Radiat. Transfer **30**, 317 (1983).
[7] R. L. Kelley, J. Phys. Chem. Ref. Data **16**, Suppl. 1, 1 (1987).
[8] K-N. Huang *et al.*, At. Data Nucl. Data Tables **18**, 243 (1976).
[9] S. Augst *et al.*, Phys. Rev. Lett. **63**, 2213 (1989).
[10] O. F. Hagena and W. Obert, J. Chem. Phys. **56**, 1793 (1972).
[11] S. T. Pratt and P. Dehmer, Chem. Phys. Lett. **87**, 533 (1982).
[12] B. Bouma *et al.*, J. Opt. Soc. Am. B **10**, 1180 (1993).
[13] R. B. Spielman *et al.*, J. Appl. Phys. **57**, 830 (1985).
[14] R. Stewart, *Experimental Studies of L-Shell X-Ray Emission from High Density Plasmas* (University Microfilms International, Ann Arbor, MI, 1985).
[15] P. G. Burkhalter *et al.*, J. Appl. Phys. **50**, 4532 (1979).
[16] G. A. Doschek and U. Feldman, J. Appl. Phys. **47**, 3083 (1976).
[17] W. L. Wiese, M. W. Smith, and B. M. Miles, in *Atomic Transition Probabilities* (U.S. GPO, Washington, D.C., 1969), NSRDS-NBS 22.
[18] D. R. Bates and A. Dalgarno, in *Atomic and Molecular Processes*, edited by D. R. Bates (Academic, New York, 1962), p. 245.
[19] H. A. Bethe and E. E. Salpeter, in *Quantum Mechanics of One- and Two-Electron Atoms* (Springer-Verlag, Berlin, 1957), p. 266.
[20] E. J. McGuire, Phys. Rev. A **16**, 73 (1977).
[21] C. J. Powell, Rev. Mod. Phys. **48**, 33 (1976).
[22] A. McPherson *et al.*, "Evidence for the Multiphoton Production of Hollow Atoms: Xe L-Shell Emission in the 4–5 keV Region" (to be published).

Appendix C: "Multiphoton X-Ray Generation from Clusters: Analysis of Energy Transfer Scaling"

MULTIPHOTON X-RAY GENERATION FROM CLUSTERS: ANALYSIS OF ENERGY TRANSFER SCALING*

K. Boyer, X. Chen, A. McPherson, B. D. Thompson
and C. K. Rhodes

Laboratory for Atomic, Molecular, and Radiation Physics
Department of Physics, M/C 273, University of Illinois at Chicago
845 W. Taylor, Room 2136, Chicago, IL 60607-7059

ABSTRACT

A preliminary analysis is given concerning the scaling relations for multiphoton production of inner-shell vacancies and prompt X-ray emission from molecules and clusters. The discussion, which is based on recent studies of X-ray emission (5-16 Å) observed from Kr and Xe clusters, indicates that energy deposition rates exceeding ~ 1 W/atom are feasible in appropriately designed molecules incorporating heavy atoms.

1. Introduction

A cluster/molecule mechanism[1] has been postulated for the multiphoton production of X-rays. Of particular significance in this analysis are intra-cluster processes of the form

$$e^- + X \longrightarrow e^- + e^- + (X^+)^* \qquad (1)$$

which can lead to the excitation of inner-shell electrons and prompt X-ray emission. This concept represents the cluster/molecule analog of an interaction previously considered for multiphoton excitation of free atoms[2].

Recent experiments,[3,4] specifically designed to evaluate certain essential predictions of the cluster picture,[1] have furnished considerable supporting evidence for the main features of the proposed model. These studies, which involved Kr and Xe, (1) established the crucial role of cluster formation[3] in the generation of soft X-ray (~ 80-150 eV) emission, (2) verified the scaling of this new phenomenon into the kilovolt (~ 800-2100 eV) region,[4] and (3) provided important insights concerning the dynamical character of the strong-field coupling to the clusters.[4] Although these findings[1,3,4] are only the initial studies of these interactions and much further examination is necessary, there currently exists a sufficient body of information on which to base an analysis of the consequences of these results. Therefore, a preliminary assessment of certain key scaling relations is the goal of the discussion presented below. Particular emphasis is given to an exploration of the upper limits of power and energy transfer, since these limits will govern the efficacy of multiphoton processes in the generation of bright X-ray sources.

---

* Submitted to the ICOMP VI Proceedings, 9 September 1993

2. Discussion

2.1. Background

Several years ago estimates were made concerning limiting cross sections for multiphoton coupling to free atoms.[5] The main interest was the evaluation of the effective cross section for energy transfer in the high intensity limit ($> 10^{19}$ W/cm^2) for heavy materials. The analysis considered only individual atoms and incorporated assumptions concerning the electronic motions induced by the incident wave consistent with establishing an upper bound on the cross section. The outcome was the prediction that an energy transfer rate in the range of 0.1-1.0 W/atom was feasible with an intensity of irradiation of $\sim 10^{19}$-10^{20} W/cm^2. This enormous value for the rate of energy transfer is roughly comparable to that developed during the subpicosecond irradiation of solid surfaces at high intensity.[6]

Although it may be difficult to produce the conditions necessary for such a high rate of energy transfer to occur in free atoms,[7] the results of current experimental studies indicate that properly designed molecules[1,3,4] are able to develop rates of that magnitude. Specifically, the experimental findings suggest that molecules can be designed in a fashion that enables them to behave transiently like solid matter. Hence, a gas of these molecules responds as a solid whose average density can be independently controlled. In such a medium, since the highly ionized molecules subsequently undergo a rapid coulomb explosion, the system quickly converts itself into an ionic gas combining a relatively low average particle density with an unusually elevated energy density.

2.2. Conditions for Cluster Excitation and X-Ray Emission

Consider a spherical cluster of n identical atoms. The multiphoton induced production of prompt short wavelength radiation from clusters requires that certain conditions be met.[1] These requirements establish relationships between the intensity of irradiation[1] and the cluster size (n) which define allowed zones for the emission to occur. Certainly, such emission can only take place if sufficient kinetic energy is possessed by the colliding electron in Eq. (1) to excite an inner electron. This condition leads to the specification of two limiting intensities given by

$$I_o = \frac{\epsilon_e^2}{8\pi\alpha n^{2/3}\lambda r_o^2} \tag{2}$$

and

$$I_n(\lambda) = \frac{2\pi^3}{\alpha}\left(\frac{r_o}{\lambda}\right)^2 (mc^2)\left(\frac{c}{\lambda_c}\right)\frac{n^{2/3}}{\lambda^2}, \tag{3}$$

in which ϵ_e, r_o, α, λ, m, λ_c, and c denote the inner-shell binding energy,[8] the interatomic spacing of the cluster, the fine structure constant, the wavelength of irradiation, the electron mass, the electron Compton wavelength, and the speed of light, respectively. In this picture, an inner-shell (j-1) electron with binding energy ϵ_e can be ionized if the intensity exceeds a lower bound given by either I_o or $I_n(\lambda)$, whichever is greatest. In addition to the production of

a vacancy in the (j-1)-shell, prompt $j \longrightarrow j\text{-}1$ emission requires the retention of at least one electron in the outer j-shell during the course of irradiation. This determines an upper bound on the intensity which, with the use of the tunneling ionization model,[9] leads to a limiting intensity $I_{max}(j)$ given by

$$I_{max}(j) = cE_p^4(j)/128\pi e^6 Z^2, \qquad (4)$$

where $E_p(j)$ is the ionization potential[10] of the most tightly bound j-shell electron, Z the resulting ionic charge and e the electronic charge. Hence, the allowed zone for prompt X-ray emission from atoms of a homonuclear cluster appears generally as a triangular region of the form shown in Fig. 1.

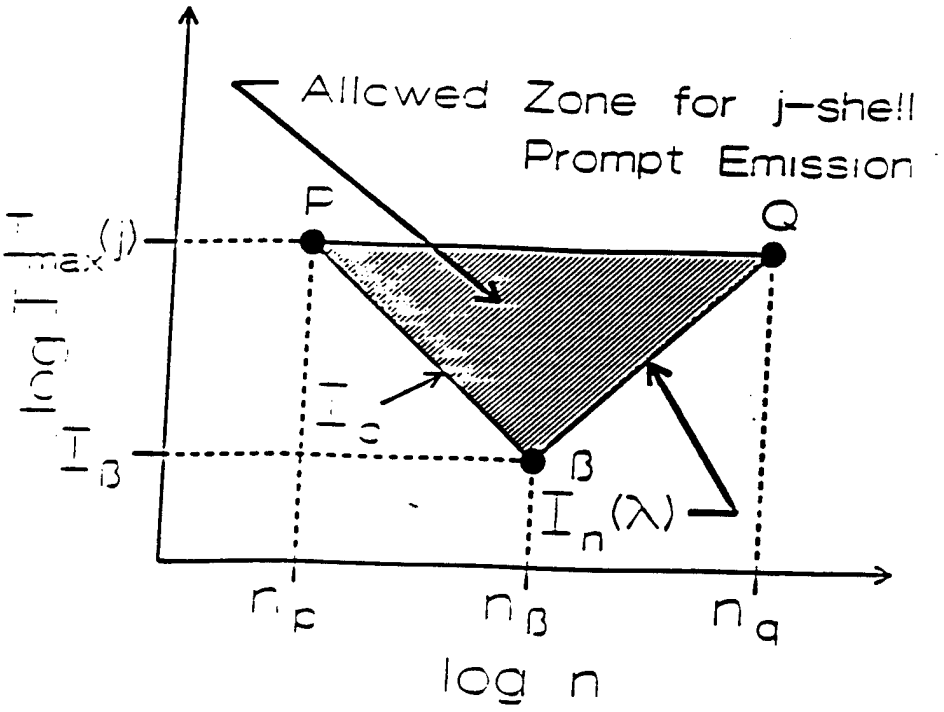

Fig. 1: General representation of the allowed zone for prompt j-shell emission from a homonuclear cluster as a function of intensity (I) and cluster size n. The three constraints arising from Eqs. (2), (3), and (4) are shown along with the corresponding intersections P, Q, and β.

It can be readily shown[1] that an approximate estimate of the number N_x of excitations occurring through reaction (1) in the cluster can be written as the product of the number of electrons produced in the cluster (nZ), the atomic density in the cluster (r_0^{-3}), the cross section for the inelastic channel under consideration (σ_{ei}), and the characteristic scale length R of the cluster given approximately by

$$R = r_o n^{1/3}. \tag{5}$$

Therefore, for reaction (1),

$$N_x = (nZ)\sigma_a r_o^{-3} r_o n^{1/3} = n^{4/3} Z \frac{\sigma_a}{r_o^2}, \tag{6}$$

with Z determined through Eq. (4) for the corresponding intensity. Equation (6) is a conservative estimate, since it assumes that the electrons driven by the external field experience only a single transit through the cluster and are subsequently lost to ionization.

An important immediate consequence of Eq. (6) is the existence of a critical size

$$n_c = \left(\frac{r_o^2}{Z\sigma_a} \right)^3 \tag{7}$$

defined by the condition $N_x = n$. Therefore, if σ_{ei} corresponds to an inner-shell ionization, with $n \geq n_c$ an inner-shell vacancy would be produced in every atom. Furthermore, since the critical size of the cluster depends inversely on the square of the atomic density ($\rho_a^{-2} = r_o^6$) and inversely on the cube of the cross section for excitation (σ_{ei}^{-3}), n_c is a direct analogue of the nuclear concept of a critical mass, with σ_{ei} replacing the neutron fission cross section σ_{nf} and Z playing the role of the average neutron yield $\bar{\nu}$. We note that the definition of a critical cluster size n_c for inner-shell excitation highlights the complexity of the relationships governing the coupling by combining (1) a static structural factor (r_o), (2) a dynamical consideration involving inelastic electron collisional processes (σ_{ei}), and (3) the nonlinearity of the interaction with the strength of the radiation field, which is implicitly represented by the factor Z.

2.3. Synopsis of Experimental Findings

The general picture presented above has been specifically tested in a recent series of experiments.[3,4] Specifically, these studies have examined the Xe(N) and Kr(M) shells[3] in the 80-150 eV region and the Xe(M) and Kr(L) shells[4] in the 800-2100 eV range. The spectroscopic results obtained in all four cases were found to be generally in agreement[3,4] with the expectations of the cluster picture.[1] The studies of the Xe(N) and Kr(M) shell emissions[3] established the crucial role of cluster formation in the generation of the observed spectra. The corresponding examinations of the Xe(M) and Kr(L) shell radiation established important aspects of the scaling of this new phenomenon into the kilovolt spectral range.

3. PRELIMINARY ANALYSIS OF SCALING RELATIONSHIPS

Important clues concerning the mechanism of interaction and the scaling of the energy transfer rate arose from the analysis[4] of the spectra in the 5-16 Å range involving the Kr L-shell and Xe M-shell emissions. Specifically, these data provided detailed information concerning the dynamics of the energy transfer and indicated (1) the significance of multiple transits of the driven electrons through the cluster and (2) the possible influence of coherent electron motions on the magnitude of the multiphoton coupling.

3.1. Estimate of Multiple Transits

The spectroscopic evidence[4] indicates that the excitation is confined to a short time interval which corresponds to the duration of the physical integrity of the cluster. An estimate of this time from the data gave a time $\tau \sim 10$ fs, a value which fits reasonably well with the range anticipated from the dynamics of a coulomb explosion of the ionized cluster. Since the period of the incident radiation is significantly shorter than this time, the electrons driven by the external field can experience multiple transits through the cluster, one for each half-cycle of the incident wave. The number m of such transits in the time τ is given by

$$m = \frac{2\tau c}{\lambda}. \tag{8}$$

3.2. Scaling of Energy Transfer Rate and Possible Role of Coherent Motions

It was possible to establish a lower bound on the experimentally generated energy transfer rate per atom P_{xe} from the Kr data.[4] The value found was $P_{xe} \sim 240$ mW/atom, an exceptionally high magnitude. Moreover, this experimental figure was found[4] to be significantly higher than the upper bound that could be derived on the basis of Eq. (6), a statement that is based on the inelastic scattering process given in Eq. (1). Basically, the data appeared to indicate that the nonlinear coupling is anomalously strong and, consequently, that an important correction to Eq. (6) is required.

In contrast, acceptable agreement with the experimental figure P_{xe} was found in comparison with an earlier estimate[5] of the upper bound of the effective multiphoton energy transfer cross section formulated in the high intensity ($> 10^{19}$ W/cm^2) limit. This bound on the maximum cross section σ_m was the uncomplicated statement

$$\sigma_m = 8\pi\lambda_c^2 \simeq 3.6 \times 10^{-20} cm^2. \tag{9}$$

In combination with the intensity used ($I_{exp} \sim 8 \times 10^{18}$ W/cm^2) in the kilovolt studies,[4] this value gave a corresponding theoretical figure $P_{xt} = \sigma_m I_{exp} \equiv 290$ mW/atom, a magnitude which appropriately exceeds the experimental value.

The importance of this finding is that the derivation of σ_m given in Eq. (9) included a mechanism of enhanced coupling which involved an ordered electronic motion[11] induced by the external field. Without this feature in the interaction, the upper bound derived would have been in clear disagreement with the experimentally indicated value. The enhancement in the coupling stems physically from constructive interference of the driven electrons (Z) in the inelastic scattering process leading to atomic excitation. Roughly, the incorporation of this consideration into the analysis of the clusters leads to a modification in Eq. (6) of the form

$$\sigma_a \rightarrow Z\sigma_a. \tag{10}$$

Equations (8) and (10) both lead to multiplicative corrections of Eq. (6), the conservative estimate for the number of excitations N_x produced in the cluster. Therefore, the modified statement for N_x, which incorporates the combined factor $\Gamma \equiv 2\pi cZ/\lambda$ from the product of Eqs. (8) and (10), reads

$$N'_x = n^{4/3}\left(\frac{2\tau c Z^2 \sigma_{ai}}{\lambda r_e^2}\right) = \Gamma N_x, \tag{11}$$

a result which leads to a correspondingly changed critical cluster size

$$n_c' = \left(\frac{\lambda r_e^2}{2\tau c Z^2 \sigma_{ai}}\right)^3 = \Gamma^{-3} n_c. \tag{12}$$

Since $\Gamma >> 1$ is generally valid for the physical conditions of interest, the introduction of this modification has four important consequences. They are (1) the probability of excitation is substantially raised, (2) the critical cluster size is very greatly reduced, (3) a significant wavelength dependence is introduced into both of these quantities, and (4) clusters composed of heavy atoms having high levels of ionization (Z) are potently favored. Furthermore, since the magnitude of Γ can be quite large, very substantial modifications of the signal strengths experimentally produced can be expected. For example, on the basis of experimental data concerning Kr L-shell excitation,[4] $Z \cong 25$ and $m \cong 20$, giving $\Gamma \cong 500$. Therefore, in the case of the Kr L-shell, the ratio of Eq. (6) to Eq. (12) is

$$\frac{n_c}{n_c'} = \Gamma^3 \cong 1.25 \times 10^8, \tag{13}$$

an enormous reduction in the critical size which gives $n_c' \cong 33$, a value in a range that can be practically achieved.[12,13]

3.3. Molecular Design Concept

The modifications to the scaling relationships discussed above alter the molecular design conditions[1] for X-ray generation. A constraint governing the molecular design of a system optimized for X-ray production can be derived from the conditions expressed in Eqs. (2), (3), (4), and (12). We recall that the allowed zone for prompt X-ray emission appears as a triangular region of the kind illustrated in Fig. (1). If we identify the optimization of the system with (1) the utilization of the lowest possible intensity and (2) excitation of the cluster under conditions of maximal amplification per unit density,[1] then the vertex β defines that optimum subject to the subsidiary condition $n_\beta = n'_c$. An explicit statement for this situation can be easily found. From equality of Eq. (2) and Eq. (3), we find

$$n_\beta^{4/3} = \left(\frac{\lambda}{2\pi r_e}\right)^4 \left(\frac{\epsilon_e}{mc^2}\right)^2, \tag{14}$$

an expression, which, when combined with the condition $n_\beta = n'_c$ with the use of Eq. (12), gives the result

$$\left(\frac{\epsilon_e}{mc^2}\right)\left(\frac{Z^2\sigma_{ei}\tau c}{\pi r_e^3}\right)^2 = 1, \tag{15}$$

a statement which is independent of the wavelength λ. Finally, if the factor Z^2 is represented by setting $I_\beta = I_{max}(j)$ from Eq. (4), we obtain

$$\left(\frac{1}{128\pi\alpha^3}\right)\left(\frac{E_p(j)}{mc^2}\right)^2\left(\frac{E_p^2(j)}{\lambda_c^2 M_\beta}\right)\left(\frac{\epsilon_e}{mc^2}\right)^{1/2}\left(\frac{\sigma_{ei}}{\pi r_e^2}\right)\left(\frac{\tau c}{r_e}\right) = 1, \tag{16}$$

an expression which relates (1) the atomic properties [ϵ_e, $E_p(j)$, σ_{ei}], (2) the molecular parameters (r_0, τ), and (3) the intensity of irradiation (I_β). Although not fully establishing any particular molecular configuration, Eq. (16) explicitly illustrates the relative dependencies of these important variables with respect of the optimum condition.

3.4. Kr L-Shell System

The experimental study[4] of the Kr L-shell emissions was extremely informative and led to the need for the modifications expressed by the factor

$$\Gamma = \frac{2\tau cZ}{\lambda}. \tag{17}$$

Since we see that this factor (Γ) can be large, it can also have an enormous influence on the circumstances that may allow amplification.[1] We now explore the consequences of this enhanced coupling on the potential for amplification on 3 ⟶ 2 transitions in Kr ions in the wavelength region ~ 7 Å.

Table I assembles the parameters relevant to the excitation of the Kr L-shell system. We will specifically consider the Kr^{26+} transition[14,15] ($1s^22s^22p^6$ ⟵ $1s^22s^22p^53d$) at 6.70 Å which has a radiative lifetime[16] of ~ 10 fs. An estimate of the Doppler broadening that would occur[1] as a result of the coulomb explosion of the cluster indicates that Doppler broadening exceeds the radiative width, so we will use a stimulated emission cross section reflecting that larger width. Using the results developed elsewhere,[1] and incorporating the enhancement given by Eq. (17), we can write the X-ray gain constant g_λ per unit electron density n_e as

$$\frac{g_\lambda}{n_e} = \frac{\lambda_x^3\sqrt{2}}{8\pi}\left(\frac{A_x}{c}\right)\left(\frac{\sigma_{ei}}{r_e^2}\right)\left(\frac{\tau c}{\lambda}\right)\left(\frac{Mc^2a_o}{e^2}\right)^{1/2}\left(\frac{r_o}{a_o}\right)^{1/2} \tag{18}$$

for homogeneous clusters composed of atoms having mass M and an X-ray transition with a spontaneous emission rate A_x. We note that g_λ/n_e is independent of the level of atomic ionization Z and involves a dependence on the wavelength of excitation λ. If we assume further that the greatest permissible electron density of the medium is the critical electron density corresponding to wavelength λ, then the maximum value of the gain constant g_λ achievable scales as λ^{-3}, a dependence heavily favoring shorter wavelengths.

Table I: Parameters applying to the Kr L-shell Kr^{26+} ($1s^2 2s^2 2p^6$ — $1s^2 2p^2 2p^5 3d$) transition at 6.7 Å with excitation at 248 nm. The column (ε_λ/n_e) assumes that the full ionic population resides in the excited Kr^{26+} state.

Material	r_0(Å)	Transition λ(Å)	ϵ_ϕ (eV)	Z	I_{max}(W/cm^2)	σ_{ai}(cm^2)	τ(fs)	n_c^*	$A_{\frac{3}{2}}$ (s^{-1})	ε_λ/n_e(cm^2)
Kr	4.0	L(3-2) ~ 7	− 1670	26	− 8 × 10^{18}	4.3 × 10^{-20} (2p)	− 10	− 33	− 10^{14}	2.6 × 10^{-18}

4. Conclusions

Recent experimental findings have indicated that Kr and Xe clusters undergoing multiphoton excitation in strong fields produce intense X-ray emission from directly excited ionic states. An analysis of the scaling relationship involved in the multiphoton coupling, in light of these new experimental data, indicate that energy deposition rates exceeding − 1 W/atom are feasible in appropriately designed molecules incorporating heavy atoms.

5. Acknowledgements

Support for this research was provided under contracts (DoE) DE-FG02-91ER1208, AFOSR-89-0159, (ONR) N00014-91-J-1106, (SDI/NRL) N00014-91-K-2113, and (ARO) DAAL 3-91-G-0174.

6. References

1. A. McPherson, T. S. Luk, B. D. Thompson, K. Boyer, and C. K. Rhodes, "Multiphoton Induced X-Ray Emission and Amplification from Clusters," *Appl. Phys. B* 57, XXX (1993).
2. C. K. Rhodes, "Studies of Collision-Free Nonlinear Processes in the Ultraviolet Range," in *Multiphoton Processes*, edited by P. Lambropoulos and S. J. Smith (Springer-Verlag, Berlin, 1984) p. 31.
3. A. McPherson, T. S. Luk, B. D. Thompson, K. Boyer, and C. K. Rhodes, "Role of Cluster Formation on Multiphoton Induced Soft X-Ray (75-152 Å) Emission from Kr and Xe Ions," submitted to Phys. Rev. Lett., 1 September 1993.
4. A. McPherson, X. Chen, B. D. Thompson, A. B. Borisov, O. B. Shiryaev, K. Boyer, and C. K. Rhodes, "Kilovolt X-Ray (5-16 Å) Emission from Multiphoton Excited Kr and Xe Clusters," submitted to Phys. Rev. Lett., 1 September 1993.
5. K. Boyer, H. Jara, T. S. Luk, I. A. McIntyre, A. McPherson, R. Rosman, and C. K. Rhodes, "Limiting Cross Sections for Multiphoton Coupling," *Revue Phys. Appl.* 22, 1793 (1987).
6. A. Zigler, P. G. Burkhalter, P. J. Nagel, K. Boyer, T. S. Luk, A. McPherson, J. C. Solem, and C. K. Rhodes, "High Intensity Generation of 9-13 Å X-Rays from BaF_2 Targets," *Appl. Phys. Lett.* 59, 777 (1991).

7. P. H. Y. Lee, P. E. Casperson, and G. T. Schappert, "Search for Multiphoton-Induced Inner-Shell Excitation," *Phys. Rev. A* **40**, 1363 (1989).
8. K-N. Huang, M. Aoyagi, M. H. Chen, B. Crasemann, and H. Mark, "Neutral-Atom Electron Binding Energies from Relaxed-Orbital Relativistic Hartree-Fock-Slater Calculation," *Atomic Data and Nuclear Data Tables* **18**, 243 (1976).
9. S. Augst, D. Strickland, D. D. Meyerhofer, S. L. Chin, and J. H. Eberly, "Tunneling Ionization of Noble Gases in a High-Intensity Laser Field," *Phys. Rev. Lett.* **63**, 2212 (1989).
10. T. A. Carlson, C. W. Nestor, Jr. N. Wassermann, and J. D. McDowell, "Calculated Ionization Potentials for Multiply Charged Ions," *Atomic Data* **2**, 63 (1970).
11. K. Boyer and C. K. Rhodes, "Atomic Inner-shell Excitation Induced by Coherent Motion of Outer-shell Electrons," *Phys. Rev. Lett.* **54**, 1490 (1985).
12. W. Miehle, O. Kandler, T. Leisner, and O. Echt, "Mass Spectroscopic Evidence for Icosahedral Structure in Large Rare Gas Clusters: Ar, Kr, Xe," *J. Chem. Phys.* **91**, 5940 (1989).
13. O. F. Hagena and W. Obert, "Cluster Formation in Expanding Supersonic Jets: Effects of Pressure, Temperature, Nozzle Size, and Test Gas," *J. Chem. Phys.* **56**, 1793 (1972).
14. Raymond L. Kelly, "Atomic and Ionic Spectrum Lines below 2000 Angstroms: Hydrogen through Krypton, Part I (H-Cr) and Part II (Mn-Kr)," *J. Phys. Chem. Ref. Data*, Vol. **16**, Suppl. 1, 1 (1987).
15. R. Stewart, *Experimental Studies of L-Shell X-Ray from High Density Plasmas*, (University Microfilms International, Ann Arbor, MI, 1985).
16. The lifetime was calculated with the algorithm developed by R. D. Cowan.

Appendix D: "Multiphoton-Induced X-Ray Emission at 4 - 5 keV from Xe Atoms with Multiple Core Vacancies"

Multiphoton-induced X-ray emission at 4–5 keV from Xe atoms with multiple core vacancies

A. McPherson, B. D. Thompson, A. B. Borisov, K. Boyer & C. K. Rhodes

Department of Physics (M/C 273), University of Illinois at Chicago, 845 West Taylor Street, Chicago, Illinois 60607-7059, USA

SEVERAL recent experimental findings[1-3] have pointed to a possible route for making an X-ray laser, which could in principle provide an imaging system capable of molecular resolution[4]. The method involves the multiphoton excitation of atoms in van der Waals clusters or in molecules to yield ions with core-electron vacancies[1,2], which can then decay by emission of X-rays, in conjunction with a self-chanelling propagation mode of electromagnetic radiation[3]. The multiphoton excitation may be stimulated by ultrahigh-brightness, subpicosecond pulses of laser light[5]. We have previously observed[2] emission of X-rays from L-shell transitions in core-excited krypton atoms using this approach. Here we report the multiphoton production of X-rays of wavelength 2–3 Å from highly ionized xenon atoms which possess a large number of inner-shell vacancies while retaining several electrons in relatively weakly bound outer orbitals. Atoms with this 'inverted' electronic configuration are designated 'hollow atoms'[6,7]. We find that generation of hollow atoms can become the dominant excitation mode for such systems, making their exploitation in an X-ray laser a real possibility.

In the cluster/molecule approach proposed previously for X-ray amplification, a molecule or a loosely bound cluster of atoms is irradiated by an intense ($>10^{16}$ W cm^{-2}) source with a wavelength matched to the excitation conditions of the atomic constituents. An initially ionized free electron in the cluster or molecule may then lead to further ionization via intra-cluster inelastic electron–atom collisions:

$$e^- + X \rightarrow (X^+)^* + e^- + e^-$$

By adjusting the excitation intensity depending on the interatomic spacings and inner-shell binding energies, processes such as these can lead to the selective generation of inner-shell excited species. We have tested some of the predictions of this model previously for the production of Kr(L) (5–7-Å) emission[2]. A significant feature of the Kr(L) spectrum was the anomalous strength of the satellite lines, a property that indicates the occurrence of inner-shell ($n=2$) excitation while outer-shell ($n=3$) electrons remain bound to the atom.

We have now obtained experimental evidence for the direct multiphoton production in gas-phase xenon clusters of hollow atoms having multiple L-shell vacancies. Specifically, we have observed Xe(L) emission in the 2–3 Å range produced by excitation of the clusters with ultra-intense subpicosecond ultraviolet radiation. One measurement involves the recording of X-ray 'pinhole' CCD (charge-coupled device) camera images of the radiating zone with a spatial resolution of ~100 μm. Another entails spectral measurements obtained with a von Hámos curved crystal spectrometer[8]. Both studies were performed with the apparatus and methods previously described[2]. The clusters

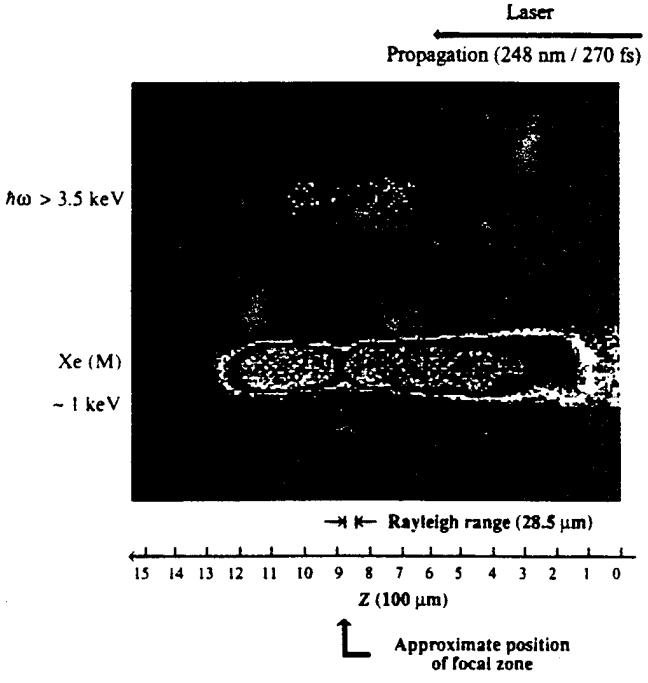

FIG. 1 X-ray images produced by a single exposure with the double pinhole camera. The upper and lower pinholes correspond to the Xe(L) and Xe(M) emissions, respectively. The pinholes had a diameter ~100 μm, limiting the spatial resolution to that value. The stagnation pressure of the pulsed jet was 75 pounds per square inch above atmospheric pressure and the temperature of the nozzle was 233 K. The approximate location of the focal region is indicated along with the corresponding Rayleigh range of the focusing system (*f*/3). The more restricted spatial distribution of the shorter wavelength emission ($\hbar\omega_x > 3.5$ keV) is expected, as significantly higher intensities are needed for the L-shell excitation relative to those required for the corresponding M-shell excitation[1,2]. Intensity grey scale is presented in pseudocolour.

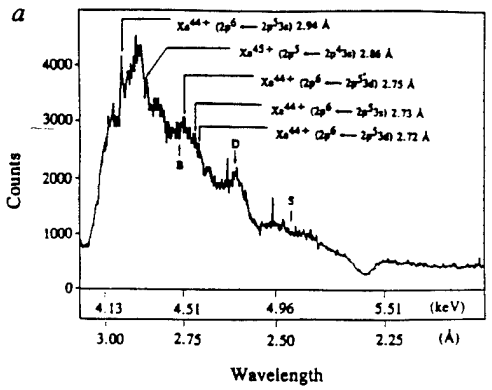

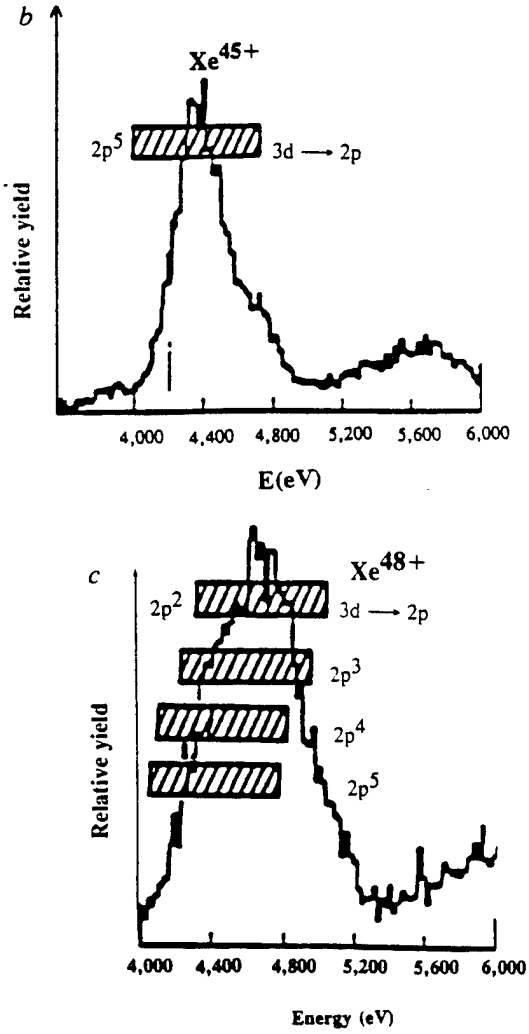

FIG. 2 *a*, The spectrum of the short-wavelength component ($\hbar\omega_X > 3.5$ keV) shown in Fig. 1, recorded with 720 laser pulses by a von Hámos spectrometer operating in third order. The spectrum shows a single broad feature having a width of ~700 eV and an asymmetrical wing extending to the blue side. Additional features are also indicated and identified. Although occurring generally in the expected spectral region for L-shell transitions in Xe, the measured spectrum is entirely different from that normally anticipated (for example, Ne-like). Specifically, the customary L-shell spectrum at a low average plasma density ($n_e \approx 10^{20}$ cm^{-3}) is dominated by a few sharp lines. In contrast, it is evident that the multiphoton-produced spectrum illustrated is predominantly composed of a very broad single feature. The film was read with a film scanning system (Materials Data Inc., Livermore, California) using an Agfa (Studio Scan) scanner for negatives. D denotes a localized defect in the film. The estimated accuracy of the abscissa is ±50 eV. *b*, Xe(L) emission recorded in the 4–6 keV range following the impact of slow Xe^{45+} ions on Cu surfaces as described in ref. 7. The features in the 4–5 and 5–6 keV regions arise from $3d \rightarrow 2p$ and $4d \rightarrow 2p$ transitions, respectively, in an atom that possesses a large number of $n \geq 3$ electrons. On account of the interactions associated with the presence of the outer ($n \geq 3$) electrons, the allowed transitions become distributed over a large spectral region and a broad band of emission develops. The correspondence of the $3d \rightarrow 2p$ emission in the 4–5 keV range with the multiphoton-produced spectrum shown in *a* is marked. The abscissa has been adjusted to closely match that of *a*. The estimated accuracy of the abscissa is ±50 eV. (Shown with permission[7].) *c*, Corresponding Xe(L) emission recorded following the impact of slow Xe^{48+} ions on a Cu surface[7] which also manifests properties similar to the spectrum in *a*. The $2p^2$ and $2p^3$ (shaded) zones overlap with a shoulder at ~5 keV and feature S in *a*. The estimated accuracy at the abscissa is ±50 eV. (Shown with permission[7]).

were produced in a cooled pulsed-gas jet. We use a laser[5] with a wavelength of 248 nm, a pulse length of ~300 femtoseconds (fs, 10^{-15} s) and a peak power of ~0.7 terawatts (TW, 10^{12} W). The focusing system produces a maximum intensity of ~8 exawatts cm^{-2} (EW, 10^{18} W).

The X-ray 'pinhole' camera pictures are single-shot exposures obtained by viewing, in a direction transverse to the propagation of the 248-nm beam, the plasma excited by the focused subpicosecond 248-nm radiation directly below the pulsed jet. The camera has two pinholes that can record images simultaneously. One pinhole has a stainless-steel filter with a thickness of 12.7 μm, making it entirely 'blind' to radiation with a quantum energy $\hbar\omega_X < 3.5$ keV. The other pinhole has a filter with the composition (2,000 Å Al + 1 μm polycarbonate + 10 μm Be) so that all radiation with a quantum energy $\hbar\omega_X \gtrsim 700$ eV is transmitted. Furthermore, as the Xe(M) emission at ~1 keV was found experimentally to be considerably brighter than the Xe(L) radiation at ~4 keV, with the use of these filters, one image represents the spatial distribution of the Xe(M) radiation while the other presents the corresponding distribution of the Xe(L) emission. The experimentally observed spatial distributions are shown in Fig. 1.

In Fig. 2 we show the spectra in the 4–5 keV range obtained by our method (Fig. 2*a*), and those for Xe(L) emission following the impact of Xe^{45+} (Fig. 2*b*) and Xe^{48+} (Fig. 2*c*) ions on a copper surface[7], which were shown to come from hollow-atom states. The spectra share several characteristics including general spectral position, breadth and particular features. The overall correspondence leads to the conclusion that the $3d \rightarrow 2p$ emissions observed in both cases arise from the same type of ionic states, namely hollow-atom configurations in which inner-shell vacancies are associated with the presence of a large number (~10) of outer-shell ($n \geq 3$) electrons.

The multiphoton spectrum shown in Fig. 2*a* has a clear asymmetry, weak narrow components superimposed on the dominant broad feature, and visible modulations in the intensity that can be correlated with spectral characteristics observed in studies of ion-surface emission[6,7], laser-imploded microballoons[9] and radiatively driven capsules[10]. The asymmetry of the multiphoton spectrum can be explained by the presence of multiple L-shell vacancies. For example, the broad feature S in Fig. 2*a* at ~5 keV lies at a position representing a null in Fig. 2*b*, but this region corresponds to a significant shoulder in Fig. 2*c* which overlaps the multiple-vacancy $2p^2$ and $2p^3$ zones (shaded). Three transitions in Xe^{44+} (2.72–2.75 Å), whose known wavelengths are indicated to coincide with the feature B, correspond to the strongest lines observed in the microballoon[9] and capsule[10] studies. Additionally, two narrow transitions are identified in the multiphoton spectrum at 2.94 and 2.86 Å, attributed to $3s \rightarrow 2p$ transitions in Xe^{44+} and Xe^{45+}, respectively. The clear appearance of the Ne-like Xe^{44+} ($3s \rightarrow 2p$) line mirrors the observation of the corre-

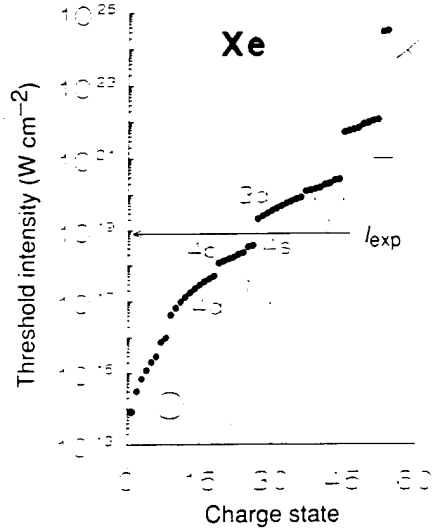

FIG. 3 Threshold intensities for ionization of electrons from bound states of xenon as derived from ref. 12. Specific electron shells and levels are indicated. With a maximum experimental intensity $I_{exp} \approx 8 \times 10^{18}$ W cm^{-2}, the Coulomb-suppression picture leads simultaneously to the disappearance of 4*d* states and the retention of the 3*d* electrons. Hence, the absence in the multiphoton spectrum illustrated in Fig. 2*a* of the $4d \rightarrow 2p$ band shown in Fig. 2*b* and *c* is another feature of experimental agreement between the results of the multiphoton excitation, the findings of the ion–surface studies[7] and the expectations of the cluster approach[1,2].

sponding Ne-like Kr^{26+} ($3s \rightarrow 2p$) transition as the strongest feature in multiphoton produced Kr(L) emission[2].

The presence of the Xe^{45+} species with the excited-state configuration ($2p^4 3s$) and the overlap of the feature S with the spectrum shown in Fig. 2*c* arising from the Xe^{48+} ions confirm the direct production of double vacancies by the multiphoton coupling and suggest that higher levels of 2*p* shell ionization are also present. The generation of the Xe^{45+} ($2p^4 3s$) state from the neutral atom requires an energy transfer[11] exceeding 70 keV.

The multiphoton spectrum in Fig. 2*a* does, however, exhibit a significant difference from those produced by ion–surface collisions[7]: the feature at ~5.5 keV in Fig. 2*b* and *c*, which corresponds to the $4d \rightarrow 2p$ component, is absent in Fig. 2*a*. This fact is easily explained by the Coulomb-suppression model of multiphoton ionization[12], the threshold conditions for which are illustrated in Fig. 3.

The comparison of the morphologies of the multiphoton-produced Kr(L) and Xe(L) spectra shown in Fig. 4 is informative. If the spectra are registered to the corresponding $2p \leftarrow 3s$ Ne-like Kr^{26+} and Xe^{44+} features, the two spectra are essentially isomorphic with the major exception that the gaps between the dominant sharp features of the Kr(L) distribution are filled in by the high density of satellite lines seen in the Xe(L) emission. Hence the line spectrum for charge state $Z = 36$ is replaced at $Z = 54$ by satellite transitions characteristic of the hollow-atom spectrum. Extrapolation of this trend leads to the conclusion that, for heavy atoms in clusters and appropriately designed molecules, the multiphoton excitation of hollow-atom states will be the predominant excitation.

A comparison of the spectrum shown in Fig. 2*a* with a spectrum thermally produced[10] with an electron temperature $T_e \lesssim 1.4$ keV at a comparable electron density ($n_e \approx 10^{24}$ cm^{-3}), as shown in Fig. 5, reveals a significant difference. The thermal spectrum deviates grossly from the multiphoton-generated distribution. Specifically, the former is essentially null between 2.8 and 3.0 Å, the region corresponding to the strong maximum in the latter. Conversely, the high degree of spectral correspondence shown between Fig. 2*a*, *b* and *c*, as the effective electron temperature associated with the ion–surface interaction is very low ($\lesssim 5$ eV), indicates that the multiphoton-produced emission involves a negligible contribution from thermal excitation. Because the multiphoton spectrum must involve electron colli-

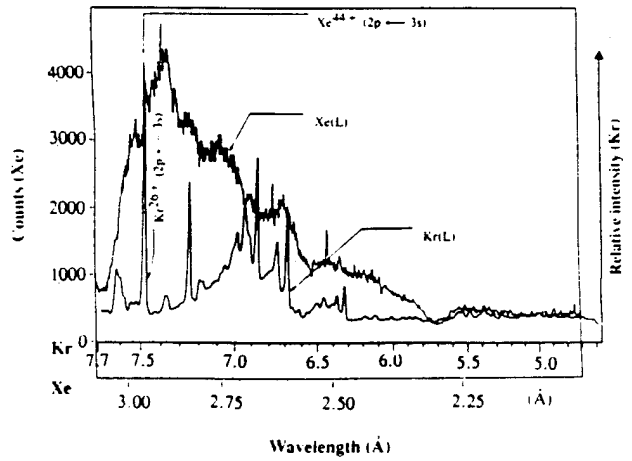

FIG. 4 Comparison of the morphologies of the multiphoton-produced emission for Kr(L) (ref. 2) and Xe(L). The two spectra are registered by the corresponding ($2p \leftarrow 3s$) Ne-like transitions for Kr^{26+} and Xe^{44+}. The conversion from a line-dominated spectrum for Kr to a continuous distribution reflecting the characteristics of the hollow-atom configurations produced with Xe is clear.

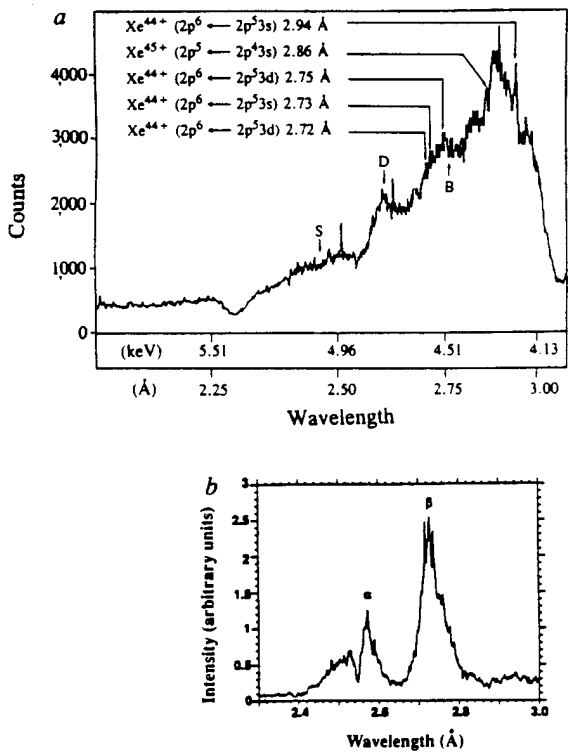

FIG. 5 Comparison of the multiphoton-generated Xe(L) spectrum (*a*) with a thermally produced spectrum[10] (*b*) obtained at a comparable electron density ($n_e \approx 10^{24}$ cm^{-3}). The thermal spectrum was obtained at a temperature estimated[10] to be $T_e \lesssim 1.4$ keV. In contrast to the spectral similarity exhibited in Fig. 2, these two spectra correspond poorly, particularly in the important region where the maximum of the multiphoton spectrum occurs (~2.8–3.0 Å). (*b* shown with permission[10].) S is a significant shoulder feature, D is a localized film defect, B is a strong line (see text), α is an identified strong feature of the thermal spectrum[10] and β is a feature of the thermal spectrum corresponding to B.

sions in the kilovolt range[1], this signifies that electron motions produced by the external field occupy only a very small fraction of the available phase space. Therefore, we can conclude that the electronic motions causing the observed multiphoton excitation possess a very signficant level of order and are not appreciably perturbed by a thermal component[13–15]. □

Received 14 February; accepted 11 July 1994.

1. McPherson, A., Luk, T. S., Thompson, B. D., Boyer, K. & Rhodes, C. K. *Appl. Phys.* B**57,** 337–347 (1993).
2. McPherson, A. *et al. Phys. Rev. Lett.* **72,** 1810–1813 (1994).
3. Borisov, A. B. *et al. Phys. Rev. Lett.* **68,** 2309–2312 (1992).
4. Solem, J. C. & Baldwin, G. C. *Science* **218,** 229–235 (1982).
5. Bouma, B., Luk, T. S., & Rhodes, C. K. *J. opt. Soc. Am.* B**10,** 1180–1184 (1993).
6. Schneider, D. *et al. Phys. Rev.* A**42,** 3889–3895 (1990).
7. Clark, M. W. *et al. Phys. Rev.* A**47,** 3983–3997 (1993).
8. Mazing, M. A. & Shevel'ko, A. P. *Proceedings of the Lebedev Physical Institute* Vol. 179 (ed. Sobel'man, I. I.) 1–50 (Nova Science, Commack, New York, 1988).
9. Contunie, Y. Yaakobi, B., Feldman, U., Daschek, G. A. & Cowan, R. D. *J. opt. Soc. Am.* **71,** 1309–1314 (1981).
10. Keane, C. J., Hammel, B. A., Osterheld, A. L. & Kania, D. R. *Phys. Rev. Lett.* **72,** 3029–3032 (1994).
11. Carlson, T. A., Nestor, C. W. Jr, Wasserman, N. & McDowell, J. D. *Atomic Data* **2,** 63–99 (1970).
12. Augst, S., Strickland, D., Meyerhofer, D. D., Chin, S. L. & Eberly, J. A. *Phys. Rev. Lett.* **63,** 2212–2215 (1989).
13. Boyer, K., Thompson, B. D., McPherson, A. & Rhodes, C. K. *J. Phys.* B (in the press).
14. Thompson, B. D., McPherson, A., Boyer, K. & Rhodes, C. K. *J. Phys.* B (in the press).
15. Boyer, K. & Rhodes, C. K. *J. Phys. B* (in the press).

ACKNOWLEDGEMENTS. The authors thank J. Wright and P. Noel for technical assistance, and S. Guggenheim for the use of his microdensitometer, and A. P. Shevel'ko for measurements with the von Hámos spectrometer. C.K.R. acknowledges discussions with D. Schneider and J. W. Longworth. This work was supported by the US DoE, AFOSR, ONR, SDI/NRL and ARO.

Appendix E: "Relativistic and Charge-Displacement Self-Channeling of Intense Ultrashort Laser Pulses in Plasmas"

Relativistic and charge-displacement self-channeling of intense ultrashort laser pulses in plasmas

A. B. Borisov*
Laboratory for Computer Simulation, Research Computer Center, Moscow State University, 119 899 Moscow, Russia

A. V. Borovskiy
General Physics Institute, Academy of Sciences of Russia, 117 942 Moscow, Russia

O. B. Shiryaev*
Laboratory for Computer Simulation, Research Computer Center, Moscow State University, 119 899 Moscow, Russia

V. V. Korobkin and A. M. Prokhorov
General Physics Institute, Academy of Sciences of Russia, 117 942 Moscow, Russia

J. C. Solem
Theoretical Division, Los Alamos National Laboratory, Los Alamos, New Mexico 87545

T. S. Luk, K. Boyer, and C. K. Rhodes
Department of Physics, University of Illinois at Chicago, Chicago, Illinois 60680
(Received 25 June 1991; revised manuscript received 20 November 1991)

A simple derivation in the Coulomb gauge of the nonlinear Schrödinger equation describing propagation of powerful ultrashort circularly polarized laser pulses in underdense cold inhomogeneous plasmas is presented. Numerical solutions are given for the two-dimensional axisymmetric case for both initially homogeneous plasmas and static preformed plasma columns. These solutions account for (i) diffraction, (ii) refraction arising from variations in the refractive index due to the spatial profile of the electron density distribution, (iii) the relativistic electronic mass shift, and (iv) the charge displacement resulting from the transverse ponderomotive force. The most important spatial modes of propagation corresponding to (1) purely relativistic focusing and (2) the combined action of both the relativistic and charge-displacement mechanisms are described. The latter leads to the formation of stable confined modes of propagation having paraxially localized regions of high intensity and corresponding paraxially situated cavitated channels in the electron density. It is further demonstrated that the dynamical solutions of the propagation tend asymptotically to the lowest eigenmodes of the governing nonlinear Schrödinger equation. Finally, the calculations illustrate the dynamics of the propagation and show that the relativistic mechanism promotes the initial concentration of the radiative energy and that the subsequent charge displacement stabilizes this confinement and produces waveguidelike channels.

PACS number(s): 52.40.Nk, 42.65.Jx, 52.35.Mw, 52.40.Db

I. INTRODUCTION

The interaction of relativistically intense subpicosecond laser pulses with gaseous media has been an area of vigorous research for the past several years. For ultraviolet wavelengths on the order of 200–300 nm, the intensity region of interest, in which relativistic effects become important, lies above $\sim 10^{18}$ W/cm^2. The propagation of radiation in such media, for intensities greater than $\sim 10^{16}$ W/cm^2, naturally causes strong nonlinear ionization in all matter. Hence, the pulse itself, even in regions where the intensity is relatively low compared to the peak value, removes many electrons [1,2] from the atomic or molecular constituents creating a plasma column in which the main high-intensity component of the pulse propagates. Therefore, in a reasonable first approximation, the investigation of the resulting propagation can be divided into two separate and distinct areas. They are (1) the atomic and plasma physics occurring in the field of the intense electromagnetic wave leading to the ionization and (2) the subsequent nonlinear propagation of the radiation in the plasma that is generated. The work described below concerns the latter issue.

To our knowledge, Akhiezer and Polovin published the first treatment of high-intensity electromagnetic waves in a cold plasma [3]. They derived the equations describing the propagation as a function of the single canonical argument $(\omega t - kz)$ appropriate for one-dimensional wave motion, reduced the problem to Lagrangian form with two integrals of motion, and presented either exact or approximate solutions corresponding to particular simplified special cases.

Several subsequent treatments have been devoted to the acceleration of charged particles in either relativistic beat waves or in the tail of a single relativistic pulse. Specifically, Noble [4] applied the equations derived by Akhiezer and Polovin to the study of single- and double-wave propagation. In other work [5] beat waves in hot

plasmas are described kinetically. The excitation of particles in cold plasmas occurring in the tail of a single intense laser pulse has also been investigated [6].

Importantly, this previous work [6], which considered the case of linear polarization, established that harmonics of the fundamental frequency are not produced at a significant power, if the plasma is underdense and the group velocity of light is close to the speed of light.

Utilizing the quasistatic approximation for the fluid equations of cold underdense plasmas, Sprangle, Esarey, and Ting [7] derived the first nonlinear, fully self-consistent set of equations describing the propagation of relativistic laser pulses into plasmas for a one-dimensional geometry. This formulation was used to obtain insight into relativistic self-focusing, including the self-consistent electron-density profiles, wake-field generation, optical guiding, and second-harmonic generation. However, since this treatment was one-dimensional, the multidimensional case remained unsolved.

An important finding of Sprangle, Esarey, and Ting [7] concerned the diffractional erosion of the leading edge of a pulse propagating in the plasma. However, in the work described below, we concentrate on the evolution of the central portion of the pulse as it propagates in the plasma and neglect the associated erosion of the leading edge.

Extensive literature exists on the motion of electrons in radiation fields of certain explicitly given forms. The solution for the case of plane monochromatic waves is known [8], and this result has been considerably extended in subsequent work [9,10]. Of course, the well-established Volkov solution for the Dirac equation also exists [11]. In particular, Bardsley, Penetrante, and Mittleman [12] have numerically simulated the relativistic dynamics of electrons in a one-electron picture that includes the effects of space charge and the spatial distribution of the radiation field.

The first treatment of the relativistic self-focusing in plasmas was developed by Max, Arons, and Langdon [13]. In addition, the general character of the electromagnetic propagation in plasmas has undergone considerable analysis. Schmidt and Horton [14], Hora [15], and Sprangle *et al.* [16,17] have evaluated the thresholds for relativistic self-focusing using analytic methods. Especially germane is the work of Sun *et al.* [18], who, for initially homogeneous plasmas, derived the two-dimensional (r,z) nonlinear Schrödinger equation governing propagation, including consideration of the combined effect of the relativistic nonlinearity and charge displacement. This work presented the lowest eigenmode of the nonlinear Schrödinger equation and included numerical evaluation of the threshold of relativistic self-focusing, the value of which has been approximately estimated in earlier work [14–17]. Finally, this analysis [18] presented the (r,z) dynamics of the propagation for the perturbed lowest eigenmode of the nonlinear Schrödinger equation for cases not involving spatial cavitation of the electron density. We note that Kurki-Suonio, Morrison, and Tajima [19] have also developed the stationary analytic solutions to this equation for a one-dimensional geometry.

Additional related works can be cited in this context. Relativistic self-focusing and beat-wave phase-velocity control in plasma accelerators are kindred subjects [20]. Computations involving particle simulations revealing the initial process of self-focusing and subsequent ponderomotively driven electron motions have been performed [21]. Other calculations analyzing the plasma dynamics and self-focusing in heat-wave accelerators [22], as well as the consideration of the nonlinear focusing of coupled waves [23], have also appeared.

In prior publications, we have (1) investigated the general behavior of two-dimensional (r,z) axisymmetric relativistic self-focusing, (2) presented results on the process of stabilization of laser pulses in plasma columns [24], (3) described, with the use of an analytical model [25], the steady-state characteristics in cavitated channels having overdense walls, (4) reported preliminary results of calculations that evaluated the combined action of the relativistic and charge-displacement mechanisms and indicated the formation of stable confined cavitated modes of propagation [26], and (5) presented the experimental evidence of relativistic and charge-displacement self-channeling of intense subpicosecond ultraviolet radiation in plasmas [27], including specific comparison with the results of this computational model [27].

The current work presents a full description of the theory of nonlinear propagation of intense axisymmetric ultrashort laser pulses in cold underdense plasmas. In this analysis we use the term ultrashort to indicate that the duration of the pulses τ satisfies the inequality $\tau_i \gg \tau \gg \tau_e$, with τ_i and τ_e designating the response times of the ions and electrons, respectively. We consider both homogeneous plasmas and preformed plasma columns. In this study, no attempt is made to establish consistency between the local ionization state and the local laser intensity, the issue outlined in Sec. I. For sufficiently-low-Z materials, such as hydrogen (H_2), this calculation would be unimportant, since full (maximal) ionization would be achieved even in rather low intensity ($\sim 10^{15}$–10^{16} W/cm^2) regions [28]. Since the main regime of interest for this work involves intensities greater than $\sim 10^{18}$ W/cm^2, we believe that the plasma conditions we have chosen for analysis are sufficiently close to the true self-consistent state to be adequate for the intended scope of this study.

The calculations discussed below have been performed with the specific goal of exploring the characteristic dynamics and stability of the propagation, including particularly, the interplay of the relativistic and charge-displacement processes. Therefore, in order to illustrate this behavior, numerical results are presented that portray the propagation and self-focusing action as a consequence of (1) the purely relativistic nonlinearity and (2) the combined action of the relativistic and charge-displacement mechanisms. Although the relativistic influence cannot be truly physically separated from the charge-displacement process, it has been examined separately because this comparison provides insight on the dynamics of the focusing action, specifically the process by which the charge-displacement and the confined propagation in the electronically cavitated channel develop. Since both the relativistic effect and the charge displace-

ment tend to locally produce a reduction in the plasma frequency (ω_p) that is more significant in the high-intensity regions, both of these effects perturb the wave fronts in a manner that encourages convergence of the wave and the formation of localized high-intensity zones. Furthermore, for both the purely relativistic and the combined cases, we have calculated the stationary eigenmodes of the nonlinear Schrödinger equation and show their relationship to the modes of propagation dynamically developed in the plasmas. In particular, it is shown that the charge displacement, especially that resulting in dynamical cavitation, has a very strong effect on the spatial character of the propagation [26].

The calculations indicate that the efficiency of confinement of the propagating energy is potentially high, namely, that a large fraction of the incident power can be trapped in a channeled mode by the combined action of the relativistic and charge-displacement processes. Furthermore, in the asymptotic regime, it is found that the channel is characterized spatially by an intensity profile and electron-density distribution corresponding to the lowest z-independent eigenstate of the nonlinear Schrödinger equation. Overall, the principal conclusion of this work is that, under appropriate conditions, a new dynamical mode of *stable highly confined propagation* naturally evolves for the propagation of sufficiently short ($\tau_i \gg \tau \gg \tau_e$) pulses of coherent radiation in plasmas. By new dynamical modes, we mean the self-channeling of the radiation through the formation of stabilized electronically cavitated paraxial modes, which result from the combined action of the relativistic and charge-displacement mechanisms. Interestingly, for ultraviolet wavelengths in the (200–300)-nm range, the power densities naturally associated with these environments can approach thermonuclear values.

In Sec. II the underlying physical concepts are presented and the governing nonlinear Schrödinger equation is derived. Section III presents the analysis of the eigenmodes of this equation. Representative results of numerical simulations of the two-dimensional axisymmetric propagation are given in Sec. IV. Section IV also contains a comparison with the purely relativistic case. Finally, the conclusions are summarized in Sec. V.

II. GENERAL CONSIDERATIONS

A. Physical model

Several physical phenomena [1–7,14–19,24–26,29] play a role in the nonlinear dynamics governing the propagation of intense coherent radiation under the conditions being examined in this study. They are the following.

(a) The creation of a plasma column by ionization in the temporally early region of the laser pulse.

(b) The influence of the spatial variation of the refractive index arising from the nonlinear response of the dielectric properties of the medium. Two mechanisms are related to the electronic component; specifically, the relativistic shift in electron mass and the ponderomotively driven electron motion which tends to displace electrons from the high-intensity zone. For sufficiently short pulses, only the electrons are expelled from the laser beam and the more massive ions, due to their substantially greater inertia, are regarded as motionless [17,18,25]. A third mechanism is the nonlinear response arising from the induced dipoles of the ions, but this is generally small and negligible [25].

(c) Defocusing mechanisms, caused by diffraction from the finite aperture and refraction by the transverse inhomogeneities in the electron density.

(d) Dissipation of laser-beam energy by (i) motion of the electrons, (ii) ionization of the gas atoms, (iii) generation of harmonic radiation, (iv) production of inverse bremsstrahlung, (v) Compton scattering, and (vi) other amplitudes of nonlinear scattering.

The present work incorporates four phenomena: (1) the nonlinear response of the refractive index of the plasma due to the relativistic increase in the mass of the free electrons, (2) the refractive index variation due to the perturbation of the electron density by the ponderomotive force, (3) the diffraction caused by the finite aperture of the propagating energy, and (4) the refraction generated by the transversely inhomogeneous plasma density associated with the formation of a plasma column. In these calculations, preformed static plasma columns were used in order to approximate the radial distribution of ionization that is expected, if the incident laser pulses were producing the ionization on their temporally leading edge. Finally, the calculations were performed for a length of propagation that is much shorter than the characteristic length for dissipation of the energy of the pulse through ionization or other modes of energy loss.

It should be noted that the relativistic intensities characteristic of the phenomena examined in this work can be currently obtained experimentally [30–32]. In particular, the experimental parameters characteristic of the ranges that would apply to the study of these phenomena are presented in Table I. With the wavelength and range of electron densities shown in Table I, the plasma is always underdense, namely, $(\omega_p/\omega)^2 \ll 1$, where $\omega = 2\pi c/\lambda$ is the angular frequency of the laser radiation and $\omega_p = (4\pi e^2 N_e/m_e)^{1/2}$ is the customary plasma frequency.

B. The propagation equation

Consider the propagation of an intense ultrashort laser pulse in a plasma with an initially radially inhomogeneous electron density, described by the function $f(r)$, so

TABLE I. Experimental parameters characteristic of the ranges that would apply for the study of relativistic and charge-displacement self-focusing of laser pulses in plasmas.

Peak intensity	$I \simeq 10^{18}$–10^{20} W/cm^2
Pulse length	$\tau \simeq 100$–1000 fs
Initial focal spot radius	$r_0 \simeq 1$–3 μm
Wavelength	$\lambda \simeq 0.248$ μm (KrF^* laser light)
Target gas densities	$\rho \simeq 10^{16}$–10^{20} cm^{-3}
Initial unperturbed electron density	$N_e \simeq 10^{17}$–10^{21} cm^{-3}

that $N_e^{(0)}=N_{e,0}f(r)$, $\max f(r)=1$. We denote the vector and the scalar potentials of the electromagnetic fields as $\mathbf{A}$ and ϕ, respectively, and the corresponding electric field as $\mathbf{E}$. Let the momentum of the electrons, the current density, and the charge density be denoted as $\mathbf{P}_e$, $\mathbf{j}$, and ρ, respectively. We assume, for the short timescale of interest, that the ions are inertially frozen in space [17,18,24,25]. Then,

$$\Box\mathbf{A}=c^{-1}\nabla\frac{\partial\phi}{\partial t}-(4\pi/c)\mathbf{j}\ , \tag{1}$$

$$\nabla^2\phi=-4\pi\rho\ , \tag{2}$$

$$(\nabla\cdot\mathbf{A})=0\ , \tag{3}$$

$$\left[\frac{\partial}{\partial t}+(\mathbf{v}_e\cdot\nabla)\right]\mathbf{p}_e=-e\left[-c^{-1}\frac{\partial\mathbf{A}}{\partial t}-\nabla\phi+c^{-1}[\mathbf{v}_e\times(\nabla\times\mathbf{A})]\right]\ , \tag{4}$$

$$\mathbf{j}=-eN_e\mathbf{v}_e,\quad \rho=e(N_e^{(0)}-N_e)\ , \tag{5}$$

$$\mathbf{v}_e=\mathbf{p}_e/m_e,\quad m_e=m_{e,0}\gamma\ ,\quad \gamma=[1+|\mathbf{p}_e|^2/(m_{e,0}c)^2]^{1/2}\ . \tag{6}$$

In the set of statements above, Eqs. (1) and (2), are the Maxwell equations, Eq. (3) is the Coulomb gauge condition, Eq. (4) is the equation of motion of the electrons, Eqs. (5) are the definition of the current density and the charge density ($N_e^{(0)}$ is the initial charge density, while N_e is the dynamical charge density), and Eqs. (6) represent the relativistic relation between the velocity $\mathbf{v}_e$ and the momentum of the electrons. In Eqs. (6), $m_{e,0}$ is the rest electron mass, $\Box=\nabla^2-c^{-2}\partial^2/\partial t^2$.

It is convenient to normalize the values in the equations presented above as follows:

$$\tilde{\mathbf{A}}=(e/m_{e,0}c^2)\mathbf{A},\quad \tilde{\phi}=(e/m_{e,0}c^2)\phi\ ,$$
$$\tilde{\mathbf{E}}=(e/m_{e,0}c^2)\mathbf{E}\ ,\quad \tilde{\mathbf{p}}_e=\mathbf{p}_e/m_{e,0}c\ , \tag{7}$$
$$\tilde{\mathbf{v}}_e=\mathbf{v}_e/c,\quad \tilde{N}_e=N_e/N_{e,0}\ ,$$

with the understanding that, henceforth, the tilde sign will be suppressed. Using the relations $(\mathbf{p}_e\cdot\nabla)\mathbf{p}_e=\nabla|\mathbf{p}_e|^2/2-\mathbf{p}_e\times(\nabla\times\mathbf{p}_e)$ and $\nabla\gamma=\nabla|\mathbf{p}_e|^2/2\gamma$, Eq. (4) becomes

$$\frac{\partial}{\partial t}(\mathbf{p}_e-\mathbf{A})-\mathbf{v}_e\times[\nabla\times(\mathbf{p}_e-\mathbf{A})]=\nabla(\phi-\gamma)\ . \tag{8}$$

In the limit $\tau\gg 2\pi/\omega_p$, the expression $\mathbf{p}_e=\mathbf{A}$ is approximately valid. As we shall see below, this condition means that the electron response can be regarded as adiabatic. Furthermore, assuming the vector potential to be circularly polarized, we write

$$\mathbf{A}(r,z,t)=\tfrac{1}{2}\{(\mathbf{e}_x+i\mathbf{e}_y)a(r,z,t)\exp[i(\omega t-kz)]+\text{c.c.}\}\ . \tag{9}$$

Consistent with the statements made above, we emphasize the use of the assumption that the pulse length in both space and time is much greater than both the plasma ($2\pi c/\omega_{p,0}$) and electromagnetic (λ) wavelengths. This leads to the validity of the inequalities

$$\left|c^{-1}\frac{\partial a}{\partial t}\right|,\left|\frac{\partial a}{\partial z}\right|\ll|ka|,|k_pa|\ ,$$

where $k^2=k_0^2-k_p^2$, $k_0=\omega/c$, and $k_p=\omega_{p,0}/c$. We use the notation $\omega_{p,0}^2=4\pi e^2N_{e,0}/m_{e,0}$ specifically to denote the unperturbed plasma frequency. With the assumptions and approximations stated above, Eqs. (1)–(8) become

$$\Box\mathbf{A}=k_p^2N_e\gamma^{-1}\mathbf{A}\ , \tag{10}$$

$$\nabla^2\phi=k_p^2[N_e-f(r)]\ , \tag{11}$$

$$\nabla(\phi-\gamma)=0\ , \tag{12}$$

$$\gamma=(1+|\mathbf{p}_e|^2)^{1/2},\quad \mathbf{p}_e=\mathbf{A}\ . \tag{13}$$

The term $c^{-1}\partial\nabla\phi/\partial t$ is omitted in Eq. (10), since γ and ϕ, according to Eqs. (9), (12), and (13), do not have a high-frequency dependence. Equations (11) and (12) result in the expression for the electron density,

$$N_e=\max[0,f(r)+k_p^{-2}\nabla^2\gamma]\ . \tag{14}$$

The logical function max(0,) provides for the physically obvious and necessary condition $N_e\geq 0$. The analogous expression for the electron density has been previously derived by Sun *et al.* [18] for the case $f(r)\equiv 1$. It should be noted that Eq. (12) states the condition for the balance of the ponderomotive and the electrostatic forces for the relativistic case. Through combining Eqs. (9), (10), and (14), we establish the equation for the slowly varying complex amplitude of the vector potential $a(r,z,t)$ as

$$\left[\frac{1}{v_g}\frac{\partial}{\partial t}+\frac{\partial}{\partial z}\right]a+\frac{i}{2k}(\nabla_\perp^2a+k_p^2\{1-\gamma^{-1}\max[0,f(r)+k_p^{-2}\nabla_\perp^2\gamma]\}a)=0\ . \tag{15}$$

In accord with the previous assumptions used in deriving Eq. (15), we have neglected the second z and t derivatives in this expression. In Eq. (15), $v_g=c\epsilon_0^{1/2}$ is the group velocity of light in unperturbed plasma, $\epsilon_0=1-(\omega_{p,0}/\omega)^2$ is its corresponding dielectric constant, and $\gamma=(1+|a|^2)^{1/2}$. It should also be noted that the electric field vector $\mathbf{E}$ and the vector potential $\mathbf{A}$ are related through the approximate relation

$$\mathbf{E}(r,z,t)\simeq -ik_0\mathbf{A}(r,z,t)\ .$$

The calculation of the propagating wave form for the central high-intensity region of the pulse is accomplished by considering the solutions of Eqs. (15) along its characteristics. Changing the variable t to $q\equiv t-z/v_g$, Eq. (15) becomes

$$\frac{\partial}{\partial z}a+\frac{i}{2k}(\nabla_1^2 a+k_p^2\{1-\gamma^{-1}\max[0,f(r)+k_p^{-2}\nabla_1^2\gamma\}]a)=0\ , \quad (16)$$

for which we seek solutions of the form $q\equiv$const. We recall that certain solutions of Eq. (16) for the special case $f(r)\equiv 1$ have already been presented [18,19,33].

The results of the computations presented in this work are given with respect to the variables (q,r,z). Specifically, the data presented in the figures below illustrate the propagation of the radiation along the z axis for $q\equiv$const. Equation (16) describes the two-dimensional (r,z) dynamics of propagation for coherent circularly polarized radiation in plasmas having an inhomogeneous transverse (r-dependent) distribution of electron density. The basic physical phenomena explicitly embodied in these equations have been outlined in Sec. II A.

III. STATIONARY SELF-LOCALIZED MODES OF PROPAGATION

Equation (16), in the case of homogeneous plasmas $[f(r)\equiv 1]$, has axisymmetric partial solutions of the form

$$a(r,z)=U_{s,n}(k_p r)\exp[i(k_p^2/2k)(s-1)z]\ , \quad (17)$$

where s is a real-valued dimensionless parameter and the real-valued function $U_{s,n}$ obeys the ordinary differential equation [18]

$$\nabla_1^2 U_{s,n}+[s+F(U_{s,n}^2)]U_{s,n}=0\ . \quad (18)$$

In this discussion the dimensionless argument $\rho=k_p r$ is used and ∇_1^2 in Eq. (18) denotes the Laplacian with the derivatives designated with respect to this variable (ρ).

The nonlinear term in Eq. (18) is

$$F(U_{s,n}^2)=-N_{s,n}/\gamma_{s,n}\ ,$$
$$N_{s,n}=\max(0,1+\nabla_1^2\gamma_{s,n})\ , \quad (19)$$
$$\gamma_{s,n}=(1+U_{s,n}^2)^{1/2}\ .$$

The natural boundary conditions for Eq. (18) are

$$\frac{dU_{s,n}(0)}{d\rho}=0,\quad U_{s,n}(\infty)=0\ . \quad (20)$$

The first condition assures axial symmetry of the solutions, while the second is necessary for the property of finite energy for the solutions. We designate these solutions as "eigenmodes" and their significance is explored below.

Consider initially, however, the eigenmodes corresponding to the purely relativistic case, functions which are obtained from Eqs. (18) and (19) by neglecting the term $\nabla_1^2\gamma_{s,n}$. Since, we are explicitly eliminating the ponderomotive potential and its influence on the motion of the electrons, in this situation the electron density will not be self-consistent. In this restricted case, Eq. (18) can be rewritten in the form

$$\frac{d}{d\rho}\left[\tfrac{1}{2}\left[\frac{dU_{s,n}}{d\rho}\right]^2+V(U_{s,n},s)\right]=-\rho^{-1}\left[\frac{dU_{s,n}}{d\rho}\right]^2\ ,$$

where $V(U_{s,n},s)=(s/2)U_{s,n}^2-(1+U_{s,n}^2)^{1/2}+1$.

The second boundary condition, stated in Eq. (20), ensures finiteness of energy only in the situation where the dynamical system defined by the last two expressions has three rest points, one of them being zero, that is for the case $0<s<1$. Exactly as in the classic theory of cubic media [34,35] for values of the parameter s belonging to this interval, the localized eigenmodes constitute a countable set that is ordered by the number of zeros $-n$ in each of its members for finite values of ρ. Figure 1 illustrates the first four eigenmodes for $s=0.95$.

Consider now the eigenmode corresponding to the unrestricted situation that includes both the relativistic and charge-displacement mechanisms, a case which is found to be fully analogous. The eigenmodes of the equation describing the combined relativistic and charge-displacement processes for the interval $0<s<1$ *also* make a countable set that can be ordered in the same way as the one associated with the purely relativistic case. The zeroth (lowest) eigenmode $U_{s,0}(\rho)$ with $s=0.95$, along with the corresponding electron density $N_{s,0}(\rho)$, given by the second formula in Eq. (19), are depicted in Fig. 2. These two functions have been developed in earlier work [18]. The first and second relativistic and charge-displacement eigenmodes for the value of the parameter $s=0.95$ and the corresponding electron-density eigenmodes $N_{s,1}(\rho)$ and $N_{s,2}(\rho)$ are depicted in Figs. 3 and 4, respectively. These higher eigenmodes exhibit the important feature that cavitation may occur in the electronic component of plasma [see Fig. (4)], *even if it does not occur* in the case of the lower eigenmodes [see Figs. 2 and 3].

A prior study [18] treated the (r,z) dynamics of the evolution of the perturbed lowest eigenmodes for the case in which no cavitation of the electronic component of plasma occurs. The lowest eigenmodes were perturbed by multiplying them by constants in the neighborhood of unity. In this case, the known regime involving oscillatory propagation was observed. However, the instability of the numerical method applied in that work [18] prevented the performance of similar computations for cases involving cavitation. Our calculations show that the analogously perturbed lowest eigenmodes $V_{s,0}(\rho)$ also propagate in the same oscillatory fashion when electronic cavitation occurs, the corresponding density of which is given by $N_{s,0}(\rho)$. It is also found that the same behavior devel-

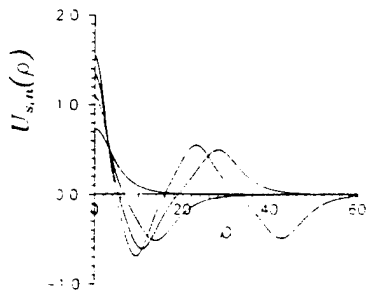

FIG. 1. Stationary axially symmetric eigenmodes with $s=0.95$ corresponding to purely relativistic self-focusing.

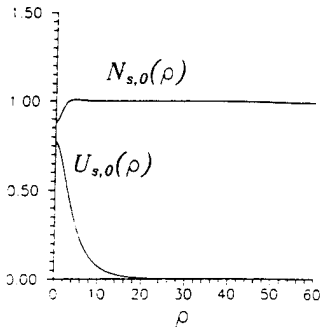

FIG. 2. The zeroth (lowest) axially symmetric stationary eigenmode with $s=0.95$ corresponding to relativistic and charge-displacement self-focusing: the normalized field amplitude distribution $U_{s,0}(\rho)$ and the normalized electron density distribution $N_{s,0}(\rho)$.

ops for the perturbed first eigenmodes, which have one or two cavitated channels in the electronic density described by $N_{s,1}(\rho)$. The results of these simulations can be regarded as evidence of the (r,z) stability of axially symmetric lowest and first eigenmodes against small perturbations in the amplitude. It should be noted, however, that these higher eigenmodes are presumably unstable against small *azimuthal* perturbations, the nature of which violates the assumed axial symmetry of the distributions.

The important consequence of the character of the solutions discussed above is the fact that the power

$$P_s=2\pi\int_0^\infty U_{s,0}^2(\rho)\rho\,d\rho$$

contained in the intensity distribution corresponding to the lowest eigenmode $U_{s,0}(\rho)$, unlike the case of a cubic medium, depends on the parameter s. Namely, this power decreases as s increases.

The infimum of P_s by s, in the internal $0<s<1$, is called the critical power (P_{cr}) of the relativistic and charge-displacement self-focusing. This power equals the critical power of the purely relativistic self-focusing [18,36] and

$$P_{cr}=\inf_{0<s<1}P_s=\lim_{s\to 1-0}P_s\ .$$

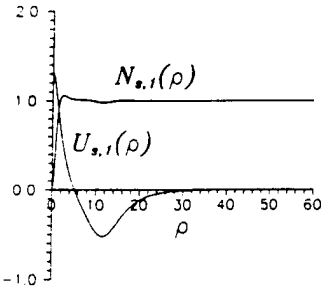

FIG. 3. The first axially symmetric stationary eigenmode with $s=0.95$ corresponding to relativistic and charge-displacement propagation: the normalized amplitude distribution $U_{s,1}(\rho)$ and the normalized electron-density distribution $N_{s,1}(\rho)$.

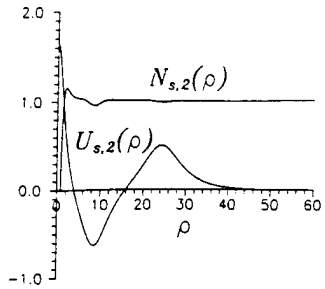

FIG. 4. The second axially symmetric stationary eigenmode with $s=0.95$ corresponding to relativistic and charge-displacement propagation: the normalized amplitude distribution $U_{s,2}(\rho)$ and the normalized electron-density distribution $N_{s,2}(\rho)$.

The explicit evaluation of this critical value is presented below. As $U_{s,0}(\rho)\to 0$, $N_{s,0}(\rho)\to 1$ for $s\to 1-0$; we have [18] therefore,

$$\gamma_{s,0}^{-1}N_{s,0}-1=N_{s,0}(1+U_{s,0}^2)^{-1/2}-1 \underset{s\to 1-0}{\approx}(1+U_{s,0}^2/2)^{-1}-1 \underset{s\to 1-0}{\approx}-U_{s,0}^2/2\ .$$

Furthermore,

$$U_{s,0}(\rho)\underset{s\to 1-0}{\approx}U_0(\rho)\ ,$$

where $U_0(\rho)$ is the positive, monotonically decreasing (reaching zero for no finite value of ρ) solution to the boundary-value problem [18,36]

$$\nabla_\perp^2 U_0-\epsilon U_0+\tfrac{1}{2}U_0^3=0\ ,$$

$$\frac{dU_0}{d\rho}(0)=0,\quad U_0(\infty)=0\ ,$$

with $\epsilon=1-s$. A change of the variables, which is a standard procedure for treating the case of the cubic nonlinearity [37], shows that [36]

$$U_0(\rho)=(2\epsilon)^{1/2}g_0(\epsilon^{1/2}\rho)\ ,$$

where g_0 is the customary Townes mode, i.e., the positive, monotonically vanishing solution to the following boundary-value problem:

$$\nabla_\perp^2 g_0-g_0+g_0^3=0\ ,$$

$$\frac{dg_0}{d\rho}(0)=0,\quad g_0(\infty)=0\ .$$

From the definition of P_{cr} and the relation between $U_0(\rho)$ and $g_0(\rho)$, it follows that

$$P_{cr}=\inf_{0<s<1}P_s=\lim_{s\to 1-0}P_s=2\pi\int_0^\infty U_0^2(\rho)\rho\,d\rho=4\pi\int_0^\infty g_0^2(\rho)\rho\,d\rho=2P_{cr,c}\ ,$$

where $P_{cr,c}\equiv 2\pi\int_0^\infty g_0^2(\rho)\rho\,d\rho$ is the critical power of the Kerr self-focusing in cubic media [34,37].

Using the resulting relation between the normalized values of the critical power of the relativistic and charge-

displacement self-focusing P_{cr} and the critical power of the Kerr self-focusing $P_{cr,c}$ we have the elementary result that

$$P_{cr}=2P_{cr,c} .$$

Finally, by calculating $g_0(\rho)$ numerically, we find the normalized value of P_{cr} with high precision [36] to be

$$P_{cr}=2P_{cr,c}=4\pi\int_0^\infty g_0^2(\rho)\rho\,d\rho\simeq 23.4018 .$$

Hence, we establish the expression for the critical power [36] as

$$P_{cr,1}=(m_{e,0}^2c^5/e^2)\int_0^\infty g_0^2(\rho)\rho\,d\rho(\omega/\omega_{p,0})^2$$
$$\simeq 1.6198\times 10^{10}(\omega/\omega_{p,0})^2\ \mathrm{W} .$$

The constant factor involved in this statement improves on that given previously [18].

The relation between $U_0(\rho)$ and $g_0(\rho)$ enables the development of the asymptotic expressions (in the case $\epsilon\to 0$) for both the peak value of the amplitude of the stationary eigenmode and for the radius of the eigenmode by using the appropriate characteristics of the Townes mode. The results are

$$U_{s,0}(0)\simeq(2\epsilon)^{1/2}g_0(0)$$

and

$$r_s\simeq\epsilon^{-1/2}r_0 ,$$

for $\epsilon\to 0$.

Special computations were performed in order to determine how close the values for $U_{s,0}(0)$ and $U_0(0)=(2\epsilon)^{1/2}g_0(0)$ are in the case where $\epsilon\ll 1$. The calculations show that $|U_{s,0}(0)-U_0(0)|/U_0(0)$ is 2.026×10^{-5} and 2.096×10^{-6} for $\epsilon=10^{-5}$ and 10^{-6}, respectively.

IV. THE TWO-DIMENSIONAL CASE

It is convenient to treat Eq. (16) numerically using the normalized coordinates

$$r_1=r/r_0 ,\quad z_1=z/(2kr_0^2) ,$$
$$u(r_1,z_1)=a_0^{-1}a(r,z) ,$$

where r_0 is a characteristic radius of the initial intensity profile and $a_0=\max|a(r,0)|$ for the selected value of q. For simplicity, we put $f_1(r_1)=f(r)$ and omit below the subscript 1 of r_1 and z_1 for brevity. Thus, the mathematical statements can be expressed in the following set of equations:

$$\frac{\partial u}{\partial z}+i\nabla_1^2u+iF(f_1(r),|u|^2)u=0,\quad z>0 \tag{21}$$

$$u(r,0)=u_0(r),\quad \max_r|u_0|=1 \tag{22}$$

$$\frac{\partial u}{\partial r}(0,z)=0,\quad u(\infty,z)=0 . \tag{23}$$

The nonlinear term F is the real-valued operator

$$F(f_1,\xi)=a_1\{1-(1+a_2\xi)^{-1/2}$$
$$\times\max[0,f_1(r)+a_1^{-1}\nabla_1^2(1+a_2\xi)^{1/2}]\} , \tag{24}$$

and the dimensionless parameters a_1, a_2 are defined as

$$a_1\equiv(r_0k_p)^2,\quad a_2\equiv I_0/I_r,\quad I_0\equiv m_{e,0}^2\omega^2c^3a_0^2/(4\pi e^2) , \tag{25}$$

where I_0 is the peak intensity at the entrance plane ($z=0$) of the medium. The parameter $I_r=m_{e,0}^2\omega^2c^3/(4\pi e^2)$ is known as the relativistic intensity [15].

The ratio of the power of the beam P_0 and the critical power of the relativistic and charge-displacement self-focusing P_{cr}, defined in Sec. III, is an important parameter characterizing Eqs. (21)–(24). In the notations of the present section, the value of P_0/P_{cr} can be expressed in the following way [36]:

$$P_0/P_{cr}=(a_1a_2/B)\int_0^\infty|u_0(r)|^2r\,dr ,$$

with dimensionless constant B given by [36]

$$B=2\int_0^\infty g_0^2(\rho)\rho\,d\rho\simeq 3.724\,51 .$$

When the initial transverse-intensity distribution is Gaussian, namely, $|u_0(r)|^2=\exp(-r^2)$, we have

$$P_0/P_{cr}=a_1a_2/(2B) .$$

We note that in several other studies, the critical power of the relativistic self-focusing is defined alternatively, basically with $B=4.0$. In the present discussion, the expression for P_0/P_{cr} involves a value of $B<4.0$, so that the corresponding ratio P_0/P_{cr} is raised. Therefore, a pulse having a Gaussian initial transverse-intensity distribution and a flat initial wave front with the parameters $a_1=248.6192$ and $a_2=0.031$, undergoes self-focusing. In this case, the ratio P_0/P_{cr}, as defined above, evaluates to 1.0347, namely, $P_0>P_{cr}$. However, using the value $B=4.0$ would give $P_0<P_{cr}$, a statement contradicting the results of the computations.

A. The initial conditions

In this section, we examine the self-focusing of coherent radiation for pulses having Gaussian or hyper-Gaussian transverse and longitudinal intensity distributions [24] of the form

$$I|_{z=0}=I_0(r,t)=I_m\exp[-(t/\tau)^{N_1}-(r/r_0)^{N_2}] ,$$
$$N_1\geq 2,\quad N_2\geq 2 \tag{26}$$

with r and t being dimensional. We assume [24] that $I_m\simeq I_r\gg I^*=10^{16}\ \mathrm{W\,cm^{-2}}$ with I^* designating the approximate value of the threshold for rapid nonlinear ionization [1,2]. The spatial amplitude distribution of the incident radiation, defined by Eq. (26) for the case of a flat incident phase front, is of the form

$$u_0(r)=\exp(-r^{N_2}/2)\ ,\quad N_2\geq 2\ . \tag{27}$$

The dimensionless parameter a_2 in Eq. (25), corresponding to the incident pulse intensity on the axis ($r=0$) of the beam $I_0(t)$, is

$$a_2=I_0(t)/I_r=(I_m/I_r)\exp[-(t/\tau)^{N_1}]\ . \tag{28}$$

The transverse profile of the plasma column, created by the temporally leading edge of the pulse, is simulated by the hyper-Gaussian function

$$f(r)=\exp[-(r/r_*)^{N_3}],\quad N_3\geq 2\ , \tag{29}$$

where r is the radial coordinate. The aperture of the plasma column r_* can be estimated [24] with the use of the relation

$$I_0(r_*,t_0)\equiv I_0(t_0)\exp[-(r_*/r_0)^{N_2}]=I^*\ . \tag{30}$$

For example, in the case of the Gaussian transverse intensity distribution ($N_2=2$), the aperture of the plasma column for $I^*=10^{16}$ W cm^{-2}, $I_r\simeq 0.45\times 10^{20}$ W cm^{-2}, and $I_0(t_0)=(0.1)I_r$, gives $r_*\simeq 2.47r_0$. In this situation, the homogeneous plasma approximation $f(r)\equiv 1$ is valid [24]. In contrast, it follows from Eq. (30) for plateaulike incident-transverse-intensity distributions that the aperture r_* of the simulated plasma column tends to the value of the beam aperture r_0. Therefore, in the example given above for $N_2=8$, we have $r_*\simeq 1.25r_0$. Thus, defocusing of the beam, which is significant because of the near coincidence of the apertures of the laser beam and the plasma column, must be taken into account when the evolution of a beam with a plateaulike incident-transverse-intensity distribution is studied [24].

B. Relativistic self-focusing

Consider the two-dimensional (r,z) solutions of the system of equations embodied in Eqs. (21), (22), and (23) for the purely relativistic nonlinear term, the form of which can be obtained from Eq. (24) by disregarding the term involving $\nabla_\perp^2$. In this case, we find

$$F(f_1,\xi)=a_1[1-f_1(r)(1+a_2\xi)^{-1/2}]\ .$$

The relativistic self-focusing mechanism prevails over the charge-displacement mechanism outside of the focal spot under the conditions $a_1\gg 1$, $a_2\simeq 1$. (Discussion of the conditions for the prevailing of the relativistic self-focusing can also be found in Ref. [33]). The situation represented by Eqs. (21), (22), and (23), with the above nonlinear term, describes self-focusing with a nondissipative saturation of the nonlinearity. The properties of the solutions for this case depend essentially on the values of two conserved integrals given specifically by

$$P_1=\int_0^\infty |u(r)|^2 r\,dr \tag{31}$$

and

$$P_2=\int_0^\infty \left[\left|\frac{\partial u}{\partial r}\right|^2-\phi(r,|u|^2)\right] r\,dr\ , \tag{32}$$

where

$$\phi(r,\xi)=\int_0^\xi F(r,\eta)\,d\eta$$
$$=a_1\{\xi-(2/a_2)f_1(r)[(1+a_2\xi)^{1/2}-1]\}\ . \tag{33}$$

Figure 5 illustrates the nature of the calculated solutions corresponding to this purely relativistic case. The parameters of the incident radiation and plasma, for the examples presented in Fig. 5, are $\lambda=0.248$ μm, $I_r=0.45\times 10^{20}$ W cm^{-2}, $I_0=\frac{2}{3}I_r=3\times 10^{19}$ W cm^{-2}, $r_0=3$ μm, and $N_{e,0}=7.5\times 10^{20}$ cm^{-3}. The corresponding values of the associated dimensionless parameters are $a_1\simeq 2.486\,192\times 10^2$ and $a_2=\frac{2}{3}$.

Figure 5(a) presents the result for purely relativistic propagation in a homogeneous plasma along the z axis for a pulse having an incident Gaussian transverse intensity distribution and a flat wave front [$N_2=2$ in Eq. (27)] for the value of q defined in Sec. II B, corresponding to $I_0=\frac{2}{3}I_r$. Figure 5(b) presents the analogous graph for a plateau like incident transverse intensity distribution [$N_2=8$ in Eq. (27)]. We conclude from these results that the solution is critically dependent upon the initial condition represented by the detailed character of the incident transverse intensity distribution.

The ratio of the beam power (P_0) to the critical power (P_{cr}) of the relativistic self-focusing for the given values of the parameters a_1 and a_2 yields $P_0/P_{cr}=22.252$ in the case of the Gaussian initial transverse intensity distribution [$N_2=2$ in Eq. (27), Fig. 5(a)] and $P_0/P_{cr}=20.168$ in the latter example of the plateaulike [$N_2=8$ in Eq. (27), Fig. 5(b)] initial transverse intensity distribution.

Note that for the values of the parameters a_1,a_2 and incident wave forms studied, we have from Eq. (32) $P_2<0$. In this situation, the following inequality is valid:

$$\max_r|u(r,z)|^2>(4/a_1a_2)|P_2|/P_1\ , \tag{34}$$

namely, with respect to the radial coordinate r, the maximum beam intensity has a positive lower bound *independent* of z. This conclusion can be established in the same way that Zakharov, Sobolev, and Synakh [37] demonstrated the analogous result in their earlier work on self-focusing. Therefore, a powerful relativistic beam, which self-focuses in a homogeneous nonabsorbing plasma ($\mu=0$, Ref. [24]), results in a field distribution representing a pulsing waveguide when $P_2<0$. Figures 5(a) and 5(b) explicitly illustrate the formation of such a regime. These pulsing waveguides consist of alternations of ring structures and focal spots on the axis of the beam. The power confined in these complex modes represents approximately 50% and 90% of the total incident power for the cases depicted in Figs. 5(a) and 5(b), respectively. It should be noted that oscillating periodic solutions of this type have also been presented by other workers [17].

In the case $P_2\geq 0$, an inequality comparable to Eq. (34) cannot be obtained. Following the method of Zakharov, Sobolev, and Synakh [37], we simulate the case $P_2\geq 0$ by considering a beam initially focused or defocused by a lens at the entrance plane ($z=0$) of the medium. Let the focusing (or defocusing) length of this lens be $R=kr_0^2R_f$

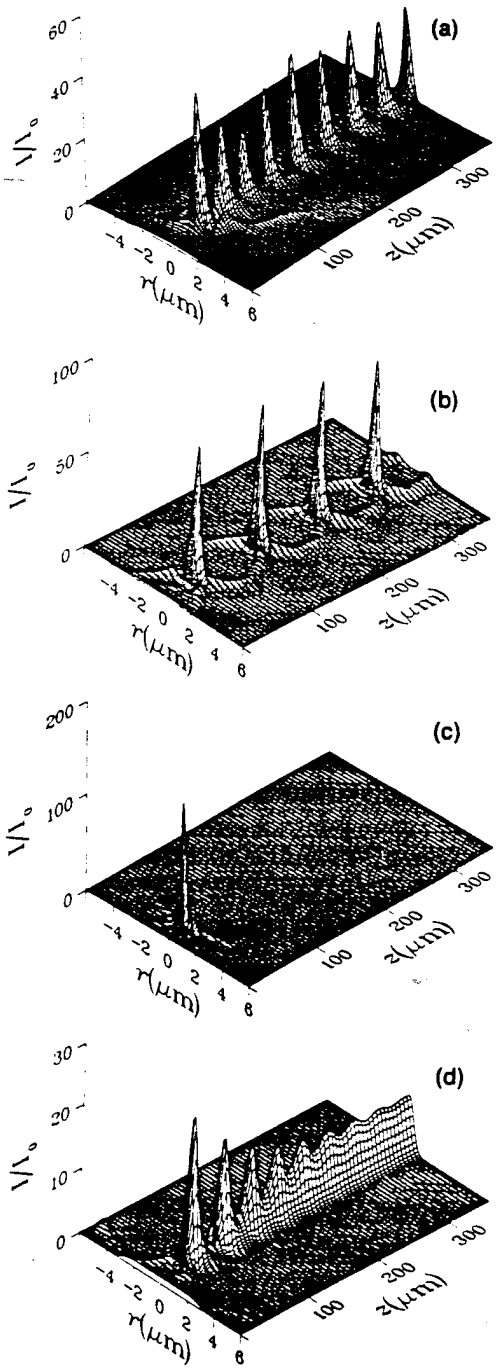

FIG. 5. Purely relativistic propagation with $I_0=3\times10^{19}$ W/cm^2, $r_0=3$ μm, $\lambda=0.248$ μm, and $N_{e,0}=7.5\times10^{20}$ cm^{-3}. (a) The formation of the pulsing waveguide regime in the case of the relativistic self-focusing of a pulse with a flat incident wave front; Gaussian initial transverse-intensity distribution [$N_2=2$ in Eq. (27)], homogeneous plasma. (b) The formation of the pulsing waveguide regime in the case of the relativistic self-focusing of a pulse with a flat incident wave front; hyper-Gaussian initial transverse-intensity distribution [$N_2=8$ in Eq. (27)], homogeneous plasma. (c) The single-focus regime in the case of the relativistic self-focusing of an initially focused pulse [$R_f=R_{f,0}/2$ in Eq. (35)]; Gaussian incident-transverse-intensity distribution [$N_2=2$ in Eq. (35)], homogeneous plasma. (d) The formation of the quasistabilized regime in the case of the relativistic self-focusing of a pulse with a flat incident wave front in a plasma column [$N_3=8$, $r_*=r_0$ in Eq. (29)]; hyper-Gaussian initial transverse-intense distribution [$N_2=8$ in Eq. (27)].

(R_f dimensionless). The condition $R_f>0$ signifies that the pulse is initially focused and $R_f<0$ indicates that it is initially defocused. Then, the corresponding initial condition can be written as

$$u_0(r)=\exp[-r^{N_2}/2+ir^2/(2R_f)],\quad N_2\geq 2\ . \tag{35}$$

Furthermore, let $P_2=0$ for $|R_f|=R_{f,0}$. We note that the case $P_2>0$ corresponds physically to a high degree of the initial focusing or defocusing: $R_{f,0}>|R_f|>0$. Moreover, when $R_{f,0}<|R_f|\leq\infty$, $P_2<0$.

Figures 5(a) and 5(c) display the calculated intensity distributions for the case of relativistic self-focusing in homogeneous plasma of beams with Gaussian incident-transverse-intensity distributions and values of R_f given by $R_f=\infty$ (flat wave front) and $R_{f,0}/2$, respectively. A more detailed study of the dynamics of the transition from the pulsing waveguide regime [see Fig. 5(a)], to the single-focus regime [see Fig. 5(c) representing the propagation of an initially sufficiently sharply focused beam)] can be found in Ref. [38]. Importantly, the computations show that the value $P_2=0$ is *not* the threshold separating these two regimes of relativistic self-focusing. This transition occurs as the first focus gains power and is shifted closer to the entrance of the medium ($z=0$), while the remaining foci are shifted in the opposite direction and, in the limit of large displacement, become diffused. Note that single-focus regimes of propagation have also been observed by Sprangle, Tang, and Esarey [17].

Defocused beams can evolve in a different fashion. Initially sufficiently sharply defocused pulses ($R_f<0$, $|R_f|\lesssim R_{f,0}/2$, $P_2>0$) propagating in the relativistic regime monotonically diffuse on the radial periphery and do not exhibit the phenomenon of self-focusing.

The detailed spatial character of the plasma column can have a strong influence on the evolution of the propagation. Figure 5(d) illustrates the relativistic propagation in a plasma column along the z axis for a pulse corresponding to $N_2=8$ in Eq. (27). The transverse profile of the plasma column is given by $f(r)$ as defined by Eq. (29) with $N_3=8$ and $r_*=r_0$. The comparison between Figs. 5(b) and 5(d) demonstrates that the defocusing of a hyper-Gaussian beam in a plasma column, with an aperture close to the radius of the beam, fundamentally alters the spatial dynamics of the propagating energy [24]. The defocusing causes a fraction of the beam to spread away from the column, but the remaining energy of the beam resolves into a state that balances the relativistic self-focusing, defocusing, and diffraction. The power trapped in this quasistabilized state so formed is approximately 25% of the incident power.

Previous analytical estimates [38] have shown that the relativistic self-focusing length is minimal when the incident pulse intensity on the axis of the beam satisfies the condition $I_0(t)=2I_r$. Moreover, specific computations also show that this inference remains valid for the case of the relativistic self-focusing of pulses with flat initial phase fronts and Gaussian incident-transverse-intensity distributions in homogeneous plasmas.

The locus of the first focus for the case of the relativistic self-focusing has been presented previously [24]. In

that study, the beam initially had both a flat phase front and a Gaussian transverse-intensity distribution. The parameters were the same as those applying to Fig. 5(a), and the duration of the pulse corresponded to $\tau=0.5\times10^{-13}$ s. The minimal z of the locus is reached when $I_0(t)=2I_r$. If the maximum intensity on the axis of the beam is such that $I_m>2I_r$, then the trajectory of the first focus executes a path that has three reversal points. Two of them, corresponding to an identical value of z, are due to the condition $I_0(t)=2I_r$. The central one, corresponding to a greater value of z, arises when $I_0(t)=I_m$. In principle, this behavior makes it possible to distinguish the process of relativistic self-focusing from that associated with the Kerr nonlinearity, since the latter results in a locus of the first focus having only a single reversal point.

C. Relativistic and charge-displacement self-channeling

This section is devoted to the description of the self-channeling occurring when both the relativistic and charge-displacement mechanisms are included in the interaction. This situation is described by Eqs. (21)–(24) and includes the important nonlinear term involving $\nabla_1^2\gamma$ appearing in Eq. (24). The numerical results show that sufficiently intense short duration ($\tau_i\gg\tau\gg\tau_e$) axisymmetric pulses readily undergo self-channeling in plasmas over a rather broad range of conditions. Moreover, it is found that a large fraction of the total incident power of the beam can be trapped in a stabilized mode confined to the axis of propagation.

A specific example is informative in representing the general behavior exhibited by the propagation in the regime in which the influence of relativity and charge displacement are both significant. These results are exhibited in Fig. 6. In the case of propagation of an initially Gaussian transverse wave form incident in a homogeneous plasma, with the parameters $\lambda=0.248$ μm, $I_0=\frac{2}{3}I_r=3\times10^{19}$ W cm^{-2}, $r_0=3\mu$m, and $N_{e,0}=7.5\times10^{20}$ cm^{-3} ($a_1=248.6192$, $a_2=\frac{2}{3}$, $P_0/P_{cr}=22.252$), the numerical computations show that, as soon as the first focus on the axis of propagation is formed, electronic cavitation occurs. Specifically, this leads to *complete expulsion* of the electronic component of plasma from the paraxial domain [Fig. 6(b)]. This process results in a quasistabilized cavitated channel in the electron distribution which extends along the entire axis of propagation past the location of the initial focus [26]. We note that some of the lowest stationary solutions corresponding to the relativistic and charge-displacement problem, including cavitation, were developed by Sun *et al.* [18]. The analysis shows that the first focus involves about 45% of the total incident power of the propagating energy. A fraction of the remaining power is dissipated through diffraction on the periphery, while another component is temporarily involved in the formation of a pulsing ring-shaped structure [Fig. 6(a)]. Subsequent energy exchange between the ringlike feature and the paraxial zone is observed, and as a consequence of this interaction, a certain part of the energy of the pulsing ring is diffracted away while the remaining power joins the paraxial domain.

In finer detail, the following aspects of the evolution of the radiative energy are also revealed by the calculations. As described above, after the formation of the first focus, considerable power is transferred from the paraxial focal zone to the ring-shaped feature, which, at this stage in the evolution of the pulse, contains approximately 68% of its total initial power. This intense ring, which spreads away from the paraxial domain, produces a corresponding ring-shaped cavity in the electronic distribution [see Fig. 6(b)]. The refraction resulting from this strongly perturbed electron-density profile, together with the relativistic self-focusing mechanism, causes the wave to return energy to the core of the beam. Thus, the charge displacement produces a potent additional self-focusing action, which leads to the formation of a confined paraxial mode of high intensity stabilized along the axis of

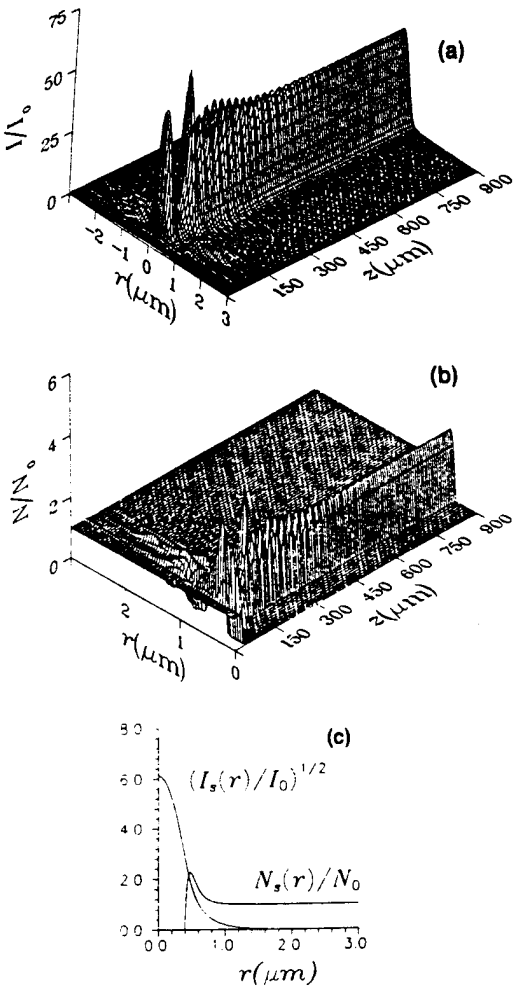

FIG. 6. The self-channeling of a pulse with a Gaussian initial transverse-intensity distribution [$N_2=2$ in Eq. (27)] and a flat incident wave front in initially homogeneous plasma in the case of the relativistic and charge-displacement propagation with $I_0=3\times10^{19}$ W/cm^2, $r_0=3$ μm, $\lambda=0.248$ μm, and $N_0=N_{e,0}=7.5\times10^{20}$ cm^{-3}. (a) The distribution of the normalized intensity. (b) The distribution of the normalized electron density. (c) Radial dependence of the asymptotic solutions for the normalized amplitude $[I_s(r)/I_0]^{1/2}$ and the normalized electron density $N_S(r)/N_0$ for $s=0.554$.

propagation. This phenomenon of confined propagation is designated as self-channeling. It should be noted that the calculations of the electrostatic energy associated with the charge displacement, which is given by the expression $W=4^{-1}\int_0^{r_c}\mathbf{E}_c^2 r\,dr$, with the electrostatic field $\mathbf{E}_c$ defined by the equation $\nabla\mathbf{E}_c=-4\pi\rho$ and r_c designating the radial extent of the channel, show that this energy can be relatively small. Specifically, for the conditions represented in Fig. 6(b) [$z=95.4$ μm], the electrostatic energy (W) accounts for only 0.18% of the total energy of the laser radiation per unit length.

The essential finding of these calculations is that the combined action of the relativistic and charge-displacement mechanisms produces a strong tendency for the generation of spatially highly confined modes of propagation which are *stabilized* along the axis of propagation. Furthermore, the study of a range of other cases indicates that these modes are exceptionally stable and that a considerable fraction of the incident power can be confined in them. The result is the controlled generation of a very high peak intensity in these channeled modes with values reaching $\sim 10^{21}$ W/cm^2 for the range of conditions studied.

Important characteristics of the asymptotic behavior of these confined modes have also been established. It has been shown that the distribution of the amplitude $u(r,z)$, for large values of z, tends asymptotically to the *lowest eigenmode* of the nonlinear Schrödinger equation (see Sec. III). Specifically, for the example discussed above, the computations have demonstrated that the asymptotic radial amplitude distribution corresponds to the lowest eigenmode with $s\simeq 0.554$. In this case, the asymptotic intensity distribution $I_s(r)=U_{s,0}^2(r)$ contains 46% of the total incident power.

The normalized asymptotic field amplitude $[I_s(r)/I_0]^{1/2}$ and the corresponding normalized asymptotic plasma electron density $N_s(r)/N_0$ are depicted in Fig. 6(c). It should be noted that the profiles of the intensity $I(r,z)$ and the electron density $N(r,z)$, obtained as the results of the dynamical calculations of the propagation for $z\simeq 900$ μm, differ from $I_s(r)$ and $N_s(r)$ for $s=0.554$ by much less than 1%. In addition, we observe that the energy of charge displacement for $r_c=2.5$ μm in the asymptotic state accounts for a fraction of 9.45×10^{-4} of the total energy of the beam per unit length. We observe that this tendency for a solution of a nonlinear Schrödinger equation involving a saturable nonlinearity to converge to the lowest stationary solution was originally discovered by Zakharov, Sobolev, and Synakh [37].

For the range of parameters studied, the calculations clearly show that the charge displacement has a very strong influence on the character of the propagation after the first focus is formed. The pulsing intensity structure, consisting of alternating foci on the axis of propagation and peripheral focal rings, which is the usual behavior for the purely relativistic self-focusing [see Figs. 5(a) and 5(b)], is converted into a stabilized and uniform channel. Collaterally, a stabilized cavitated channel in the electron density is also formed. We remark that the periodic intensity structure characteristic of the relativistic self-focusing occurs for great values of z and, therefore, may be regarded as the corresponding asymptotic solution of the purely relativistic case. The charge displacement leads to the formation of the asymptotic amplitude distribution represented by the corresponding lowest eigenmode $U_{s,0}(r)$ instead of this pulsing structure.

Computations have been also performed for the propagation of incident plateaulike wave forms with flat incident phase fronts in both homogeneous plasmas and plasma columns. Additional calculations, have also examined the behavior of focused Gaussian and plateaulike incident wave forms as well as defocused Gaussian incident wave forms in homogeneous plasmas (see Figs. 7–11). It is found that the main features described

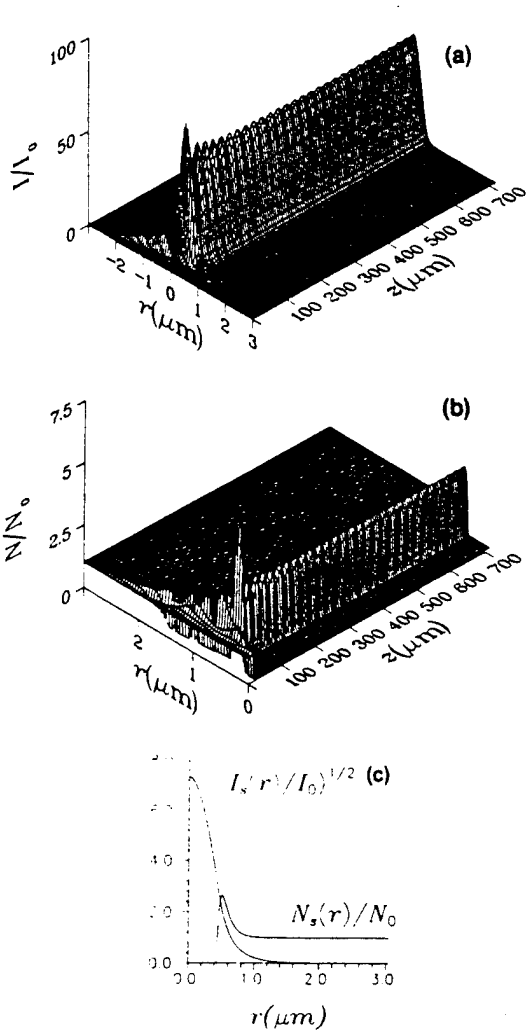

FIG. 7. The self-channeling of a pulse with a hyper-Gaussian incident-transverse-intensity distribution [$N_2=8$ in Eq. (27)] and a flat initial wave front in initially homogeneous plasma for the case of a relativistic and charge-displacement propagation with $I_0=3\times 10^{19}$ W/cm^2, $r_0=3$ μm, $\lambda=0.248$ μm, and $N_0=N_{e,0}=7.5\times 10^{20}$ cm^{-3}. (a) The distribution of the normalized intensity. (b) The distribution of the normalized electron density. (c) Radial dependence of the asymptotic solutions for the normalized amplitude $[I_s(r)/I_0]^{1/2}$ and the normalized electron density $N_s(r)/N_0$ for $s=0.515$.

above, namely (1) self-channeling, (2) stabilization of the mode of propagation, (3) the confinement of a substantial fraction of the incident power, and (4) the formation of paraxial cavitated channels in the electron distribution are common aspects of the dynamics over a wide range of conditions.

The character of these findings is now illustrated with five representative examples. For the propagation of a beam with an incident plateaulike transverse-intensity profile, given by Eq. (27) with $N_2=8$, which has a flat initial wave front incident on an initially homogeneous plasma (the values of the parameters have been adopted from above and $P_0/P_{cr}=20.168$), the asymptotic radial profile of the intensity distribution contains approximately 77% of the incident power [Fig. 7(a)]. The corresponding asymptotic amplitude is the lowest eigenmode of the nonlinear Schrödinger equation with $s\simeq 0.515$. The propagation of the same wave form in a plasma column, with the initial electron distribution defined by Eq. (29) with $N_3=8$ and $r_*=r_0$, results in a quasistabilized intensity distribution containing 34% of the incident power [Fig. 8(a)]. The purely relativistic propagation of incident plateaulike pulses [$N_2=8$ in Eq. (27)] in plasma columns [$N_3=8$ and $r_*=r_0$ in Eq. (29)] also results in the formation of quasistabilized regimes which, in this case, arise dynamically from the defocusing action of the refraction generated by the transverse profiles of the electron density [24]. For this situation, approximately 25% of the total incident power is confined [Fig. 5(d)]. The comparison of these cases with the two examples discussed above involving the charge-displacement mechanism indicates that the increase in the value of the confined power stems principally from the substantial additional focusing action arising from the inhomogeneous electron distribution produced by the ponderomotive force.

Overall, the computations reveal that the charge displacement, which generally results in electronic cavitation, plays an important role in stabilizing the mode of confined propagation that develops dynamically. This stabilization naturally occurs by refraction of the radia-

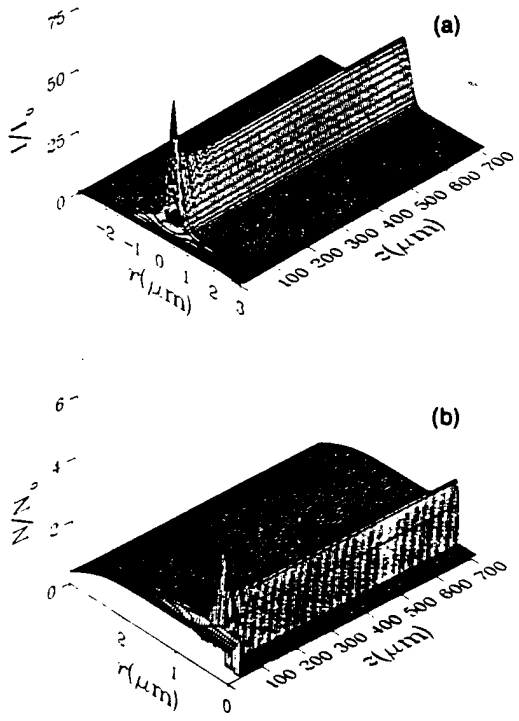

FIG. 8. The self-channeling of a pulse with a hyper-Gaussian incident-transverse-intensity distribution [$N_2=8$ in Eq. (27)] and a flat initial wave front in a preformed column-shaped plasma [$N_3=8$, $r_*=r_0$ in Eq. (29)] for the case of relativistic and charge-displacement propagation with $I_0=3\times10^{19}$ W/cm,^{2} $r_0=3$ μm, $\lambda=0.248$ μm, and $N_0=N_{e,0}=7.5\times10^{20}$ cm^{-3}. (a) The distribution of the normalized intensity. (b) The distribution of the normalized electron density.

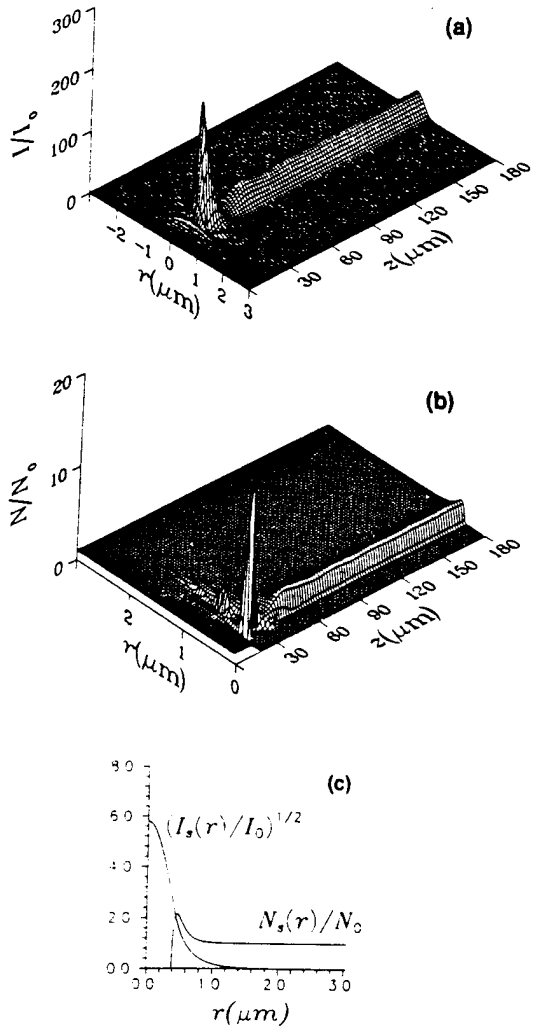

FIG. 9. Self-channeling of an initially focused [$R_f=R_{f,0}/2$ in Eq. (35)] pulse with a Gaussian incident-transverse-intensity distribution [$N_2=2$ in Eq. (35)] in initially homogeneous plasma for the case of relativistic and charge-displacement propagation with $I_0=3\times10^{19}$ W/cm^2, $r_0=3$ μm, $\lambda=0.248$ μm, and $N_0=N_{e,0}=7.5\times10^{20}$ cm^{-3}. (a) The distribution of the normalized intensity. (b) The distribution of the normalized electron density. (c) Radial dependence of the asymptotic solutions for the normalized amplitude $[I_s(r)/I_0]^{1/2}$ and the normalized electron density $N_s(r)/N_0$ for $s=0.566$.

tion into the central paraxial region. Indeed, the influence of the charge displacement on the propagation is so strong that self-channeling occurs even in the cases of *extremely* focused and defocused incident wave forms. The results of the corresponding calculations for extremely focused incident wave forms, for $R_f = R_{f,0}/2$ [Eq. (35)], with both Gaussian [$N_2 = 2$ in Eq. (35)] and plateaulike [$N_2 = 8$ in Eq. (35)] incident-transverse-intensity distributions, are depicted in Figs. 9 and 10, respectively (the parameters of beam and plasma being the same as the other examples above). In these two cases, the asymptotic transverse profiles of the amplitude and the electron density are found to correspond to the lowest eigenmodes of the nonlinear Schrödinger equation with values of the parameter $s \simeq 0.566$ (Fig. 9) and $s \simeq 0.505$ (Fig. 10). Note, in strong contrast to the situation involving charge displacement, the analogously strongly focused incident wave forms for the purely relativistic case propagate in the single-focus regime [Fig. 5(c)], and stable confinement does not develop.

Figure 11 illustrates the relativistic and charge-displacement propagation of an initially strongly defocused wave form [$R_f = -R_{f,0}/2$ in Eq. (35)] having a Gaussian initial transverse-intensity distribution [$N_2 = 2$ in Eq. (35)]. After the initial stage of the defocusing, this pulse evolves into a paraxial structure that is analogous to those described above. Furthermore, in this example the asymptotic transverse profiles of the amplitude and the electron density are found to correspond to the lowest eigenmode of the nonlinear Schrödinger equation with

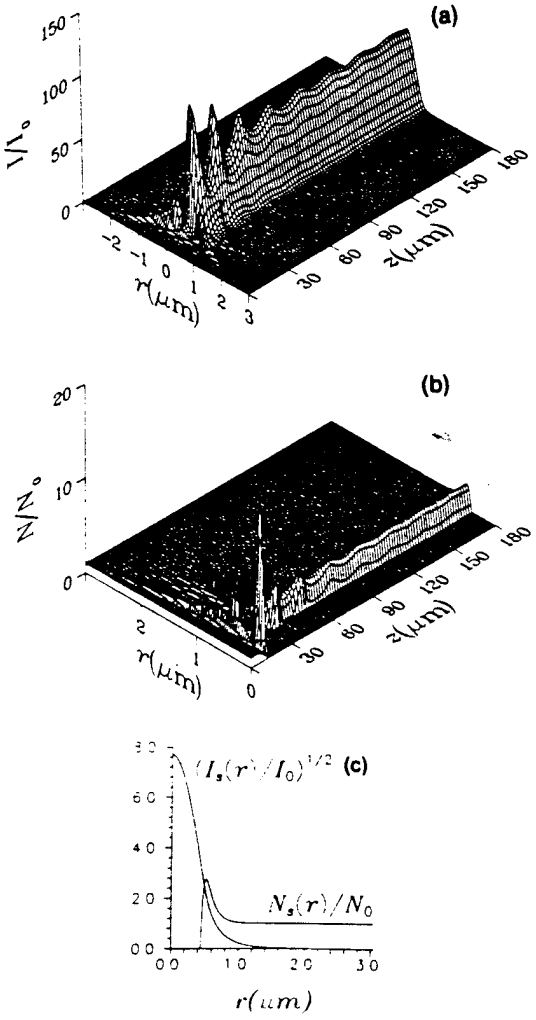

FIG. 10. The self-channeling of an initially focused [$R_f = R_{f,0}/2$ in Eq. (35)] pulse with a hyper-Gaussian incident-transverse-intensity distribution [$N_2 = 8$ in Eq. (35)] in initially homogeneous plasma for the case of relativistic and charge-displacement propagation with $I_0 = 3 \times 10^{19}$ W/cm^2, $r_0 = 3$ μm, $\lambda = 0.248$ μm, and $N_0 = N_{e,0} = 7.5 \times 10^{20}$ cm^{-3}. (a) The distribution of the normalized intensity. (b) The distribution of the normalized electron density. (c) Radial dependence of the asymptotic solutions for the normalized amplitude $[I_s(r)/I_0]^{1/2}$ and the normalized electron density $N_s(r)/N_0$ for $s = 0.505$.

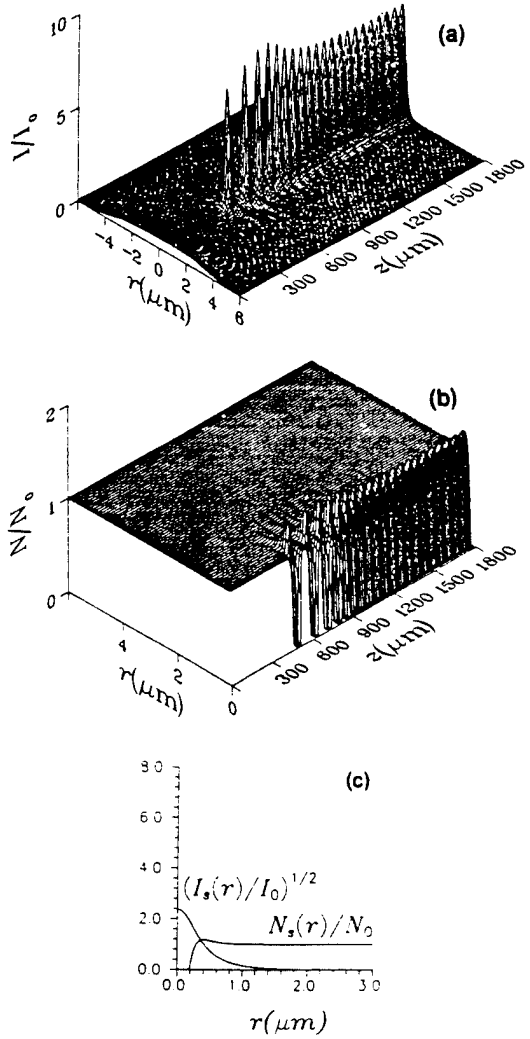

FIG. 11. The self-channeling of an initially defocused [$R_f = -R_{f,0}/2$ in Eq. (35)] pulse with a Gaussian incident-transverse-intensity distribution [$N_2 = 2$ in Eq. (35)] in initially homogeneous plasma for the case of relativistic and charge-displacement propagation with $I_0 = 3 \times 10^{19}$ W/cm^2, $r_0 = 3$ μm, $\lambda = 0.248$ μm, and $N_0 = N_{e,0} = 7.5 \times 10^{20}$ cm^{-3}. (a) The distribution of the normalized intensity. (b) The distribution of the normalized electron density. (c) Radial dependence of the asymptotic solutions for the normalized amplitude $[I_s(r)/I_0]^{1/2}$ and the normalized electron density $N_s(r)/N_0$ for $s = 0.800$.

$s \simeq 0.800$.

For these values of the dimensionless parameters assumed in these examples (Figs. 9–11) ($a_1 = 248.6192$, $a_2 = \frac{2}{3}$, that is $P_0/P_{cr} = 22.252$ for Gaussian incident wave form), the magnitude of the quantity $R_f = R_{f,0}/2$, the factor determining the degree of the initial focusing (defocusing), is 0.124. For $\lambda = 0.248$ μm and $r_0 = 3$ μm, the focusing distance $R = kr_0^2 R_{f,0}/2$, used in the examples above, has a magnitude of 28.35 μm. The fact that the self-channeling of such extremely focused or defocused distributions occurs (Figs. 9–11) means the self-channeling should be expected to be nearly independent of the initial conditions of focusing or defocusing.

A critical power P_{cr} for self-channeling arising from the relativistic charge-displacement mechanism can be defined. We now discuss this issue with a model developed in an earlier study. The threshold power P_{cr} is defined as the power that separates the asymptotic behavior, with respect to large distance of propagation (z), into two distinct classes. Since its definition rests on an asymptotic property, it can only exist in the limiting case of vanishing losses ($\mu = 0$ in Ref. [24]). For a power $P < P_{cr}$, the asymptotic transverse-intensity profile tends to zero at large z. In contrast, for $P \geq P_{cr}$ the asymptotic profile of the intensity tends to the lowest eigenmode of the governing nonlinear Schrödinger equation. Additionally, the normalized value of this critical power is exactly *twice* the corresponding normalized value of the critical power for the Kerr effect self-focusing found in cubic media for initially flat wave forms [34,37]. The expression corresponding to this critical power [36] for the relativistic and charge-displacement mechanism is

$$P_{cr} = (m_{e,0}^2 c^5/e^2) \int_0^\infty g_0^2(\rho) \rho \, d\rho (\omega/\omega_{p,0})^2 \simeq 1.6198 \times 10^{10} (\omega/\omega_{p,0})^2 \text{ W} , \tag{36}$$

where $g_0(\rho)$ is the Townes mode [34].

It has also been shown that the value of the relativistic and charge-displacement self-channeling threshold power, in cases involving initially focused or defocused beams, exceeds P_{cr} and depends on the degree of the initial focusing or defocusing. For a given magnitude of the curvature of the wave front, the value of the threshold power for initially defocused beams is greater than that for initially focused beams. Finally, it has been shown both analytically and numerically that for self-channeling of an arbitrary wave form to occur, it is sufficient that the Hamiltonian of the purely relativistic case, considered as a functional of the initial transverse amplitude distribution, should be negative [36]. The precise statement for this condition is

$$P_2(u_0) = \int_0^\infty \left\{ \left| \frac{du_0}{dr} \right|^2 - a_1 \{ |u_0|^2 - (2/a_2)[(1 + a_2 |u_0|^2)^{1/2} - 1] \} \right| r \, dr < 0 . \tag{37}$$

We now comment on the behavior of pulses having initial amplitude distributions $U_0(r)$ close to higher eigenmodes $V_{s,n}(r)$, $n \geq 1$. These higher modes generally are associated with electronically cavitated channels. The self-channeling in these cases could result in asymptotic distributions of intensity and electron density corresponding to certain higher eigenfunctions $I_{s,n}(r) = V_{s,n}^2(r)$, $N_{s,n}(r)$, $n \geq 1$. In particular, this conjecture has established an initial amplitude distribution $U_0(r)$, which is close to the first eigenmode $V_{s,1}(r)$ with $s = 0.544$. Direct numerical calculations showed that the asymptotic distributions of both intensity and electron density that evolved in this case correspond to the first eigenmode $I_{s,r}(r) = V_{s,r}^2(r)$, $N_{s,1}(r)$ with s essentially equal to 0.544. It should be additionally noted, however, that these higher eigenmodes ($n \geq 1$) are quite possibly unstable against small azimuthal perturbations that destroy their axial symmetry.

The principal result of this section is the finding that the combined action of the relativistic and charge-displacement mechanisms can result in self-channeling with the formation of stabilized paraxial modes over a rather wide range of physical conditions. Moreover, these spatially confined modes are generally associated with corresponding cavitated channels in the electron density. Finally, the characteristics of these channeled modes have asymptotic behavior that is described by the appropriate lowest eigenmodes of the governing nonlinear Schrödinger equation.

V. CONCLUSIONS

A theoretical approach suitable for the numerical investigation of the two-dimensional (r,z) dynamics of propagation of coherent ultrashort ($\tau_i \gg \tau \gg \tau_e$) relativistic laser pulses in cold underdense plasmas has been developed. Four basic physical phenomena are included within the scope of this method. They are (1) the nonlinear dependence of the index of refraction due to the relativistic increase in the mass of the electrons, (2) the variation of the index of refraction resulting from the perturbation of the electron density by the ponderomotive force, (3) the diffraction of the radiation, and (4) the refraction caused by nascent transversely inhomogeneous electron-density distributions. The equations studied in this work may be regarded as the generalization of those treated previously in other studies [18,19,33] involving initially inhomogeneous plasmas. Further studies are continuing with an extension of this analysis, which includes the azimuthal coordinate in the description of the propagation.

The main conclusions stemming from the calculations are the following.

(1) The cooperative effect of the relativistic and charge-displacement mechanisms leads asymptotically to stable high-intensity z-independent modes of self-channeling, and a major fraction of the incident power can be confined in these paraxial modes. Stable cavitation of the electron density is a general feature of these spatially confined modes.

(2) The z-independent modes, to which the solutions of the equation describing the relativistic and charge-displacement propagation tend asymptotically, are recognized as the *lowest* eigenmodes of the governing nonlinear Schrödinger equation.

(3) A separate study of purely relativistic propagation shows that beams with flat incident phase fronts exhibit a pulsing behavior in homogeneous plasmas but can undergo quasistabilization in suitably configured plasma columns. However, sufficiently sharply initially focused beams generally exhibit the development of only a single focus. In significant contrast, the present study shows that with both the relativistic and charge-displacement mechanisms, initially focused beams also generally lead to confined modes of propagation. Finally, it should be noted that the equation for relativistic self-focusing can be considered as a general model equation of propagation in saturable nonlinear media.

ACKNOWLEDGMENTS

The authors acknowledge fruitful discussions with A. R. Hinds, R. R. Goldstein, and A. McPherson. Support for this research was provided by the U.S. Air Office of Scientific Research, the U.S. Office of Naval Research, the Strategic Defense Initiative Organization, the Army Research Office, the Department of Energy, and the National Science Foundation under Grant No. PHY-9021265.

*Present address: Department of Physics, University of Illinois at Chicago, Chicago, Illinois 60680.

[1] U. Johann, T. Luk, H. Egger, and C. K. Rhodes, Phys. Rev. A **34**, 1084 (1986).

[2] T. S. Luk, U. Johann, H. Egger, H. Pummer, and C. K. Rhodes, Phys. Rev. A **32**, 214 (1985); K. Boyer, T. S. Luk, J. C. Solem, and C. K. Rhodes, *ibid.* **39**, 1186 (1989).

[3] A. I. Akhiezer and R. V. Polovin, Zh. Eksp. Teor. Fiz. **30**, 915 (1956) [Sov. Phys. JETP **3**, 696 (1956)].

[4] R. Noble, Phys. Rev. A **32**, 460 (1985).

[5] A. Magneville, J. Plasma Phys. **44**, 231 (1990).

[6] S. V. Bulanov, V. I. Kirsanov, and A. S. Sakharov, Fiz. Plasmy **16**, 935 (1990) [Sov. J. Plasma Phys. **16**, 543 (1990)].

[7] P. Sprangle, E. Esarey, and A. Ting, Phys. Rev. Lett. **64**, 2011 (1990); P. Sprangle, C. M. Tang, and E. Esarey, Phys. Rev. A **41**, 4663 (1990); A. Ting, E. Esarey, and P. Sprangle, Phys. Fluids **B2**, 1390 (1990).

[8] L. D. Landau and E. M. Lifshits, *The Classical Theory of Fields* (Pergamon, New York, 1971).

[9] E. S. Sarachik and G. T. Schappert, Phys. Rev. D **1**, 2738 (1970).

[10] J. Krüger and M. Bovyn, J. Phys. A **9**, 1841 (1976).

[11] D. M. Volkov, Z. Phys. **34**, 250 (1935).

[12] J. N. Bardsley, B. M. Penetrante, and M. H. Mittleman, Phys. Rev. A **40**, 3823 (1989).

[13] C. Max, J. Arons, and A. B. Langon, Phys. Rev. Lett. **33**, 209 (1974).

[14] G. Schmidt and W. Horton, Comments Plasma Phys. Controlled Fusion **9**, 85 (1985).

[15] H. Hora, *Physics of Laser-Driven Plasmas* (Wiley, New York, 1981).

[16] P. Sprangle and C. M. Tang, in *Laser Acceleration of Particles (the Norton Simon Malibu Beach Conference Center of the University of California, Los Angeles)*, Proceedings of the Second Workshop on Laser Acceleration of Particles, edited by C. Joshi and T. Katsouleas, AIP Conf. Proc. No. 130 (AIP, New York, 1985), p. 156.

[17] P. Sprangle, C. M. Tang, and E. Esarey, IEEE Trans. Plasma **PS-15**, 145 (1987).

[18] Gou-Zheng Sun, E. Ott, Y. C. Lee, and P. Guzdar, Phys. Fluids **30**, 526 (1987).

[19] T. Kurki-Suonio, P. J. Morrison, and T. Tajima, Phys. Rev. A **40**, 3230 (1989).

[20] E. Esarey, A. Ting, and P. Sprangle, Appl. Phys. Lett. **53**, 1266 (1988).

[21] W. B. Mori, C. Joshi, J. M. Dawson, D. W. Forslund, and J. M. Kindel, Phys. Rev. Lett. **60**, 1298 (1988).

[22] P. Gibbon and A. R. Bell, Phys. Rev. Lett. **61**, 1599 (1988).

[23] C. J. McKinstrie and D. A. Russel, Phys. Rev. Lett. **61**, 2929 (1988).

[24] A. B. Borisov, A. V. Borovskiy, V.V. Korobkin, A. M. Prokhorov, C. K. Rhodes, and O. B. Shiryaev, Phys. Rev. Lett. **65**, 1753 (1990).

[25] J. C. Solem, T. S. Luk, K. Boyer, and C. K. Rhodes, IEEE J. Quantum Electron. **25**, 2423 (1989).

[26] A. B. Borisov, A. V. Borovskiy, V. V. Korobkin, A. M. Prokhorov, O. B. Shiryaev, T. S. Luk, J. C. Solem, K. Boyer, and C. K. Rhodes (unpublished); A. B. Borisov, A. V. Borovskiy, V. V. Korobkin, A. M. Prokhorov, O. B. Shiryaev, J. C. Solem, K. Boyer, and C. K. Rhodes (unpublished); A. B. Borisov, A. V. Borovskiy, V. V. Korobkin, A. M. Prokhorov, O. B. Shiryaev, and C. K. Rhodes, Kratkie Soobsheniya po Fizike, No. 9, 3 (1991) (in Russian).

[27] A. B. Borisov, A. V. Borovskiy, V. V. Korobkin, A. M. Prokhorov, O. B. Shiryaev, X. M. Shi, T. S. Luk, A. McPherson, J. C. Solem, K. Boyer, and C. K. Rhodes (unpublished).

[28] T. S. Luk and C. K. Rhodes, Phys. Rev. A **38**, 6180 (1988).

[29] G. A. Askaryan, Zh. Eksp. Teor. Fiz. **42**, 1567 (1962) [Sov. Phys. JETP **15**, 1088 (1962)].

[30] T. S. Luk, A. McPherson, K. Boyer, and C. K. Rhodes, Opt. Lett. **14**, 1113 (1989).

[31] A. J. Taylor, C. R. Tallman, J. P. Roberts, C. S. Lester, T. R. Gosnell, P. H. Y. Lee, and G. A. Kyrala, Opt. Lett. **15**, 39 (1990).

[32] P. Maine, D. Strickland, P. Bado, M. Pessot, and G. Mourou, IEEE J. Quantum Electron. **24**, 398 (1988).

[33] P. Sprangle, A. Zigler, and E. Esarey, Appl. Phys. Lett. **58**, 345 (1991).

[34] R. Y. Chiao, E. Garmire, and C. H. Townes, Phys. Rev. Lett. **13**, 479 (1964).

[35] H. A. Haus, Appl. Phys. Lett. **8**, 128 (1966).

[36] A. B. Borisov, A. V. Borovskiy, V. V. Korobkin, A. M. Prokhorov, O. B. Shiryaev, and C. K. Rhodes, J. Laser Phys. **1**, 103 (1991).

[37] V. E. Zakharov, V. V. Sobolev, and V. S. Synakh, Zh. Eksp. Teor. Fiz. **60**, 136 (1971) [Sov. Phys. JETP **33**, 77 (1971)].

[38] A. B. Borisov, A. V. Borovskiy, V. V. Korobkin, C. K. Rhodes, and O. B. Shiryaev (unpublished); A. B. Borisov, A. V. Borovskiy, V. V. Korobkin, C. K. Rhodes, and O. B. Shiryaev, in *Short Wavelength Lasers and Their Applications,* edited by V. V. Korobkin and M. Yu. Romanovskiy (Nova Science, Commack, NY, 1992), p. 261.

Appendix F: "Observation of Relativistic and Charge-Displacement Self-Channeling of Intense Subpicosecond Ultraviolet (248 nm) Radiation in Plasmas"

Observation of Relativistic and Charge-Displacement Self-Channeling of Intense Subpicosecond Ultraviolet (248 nm) Radiation in Plasmas

A. B. Borisov,[1] A. V. Borovskiy,[2] V. V. Korobkin,[2] A. M. Prokhorov,[2] O. B. Shiryaev,[1] X. M. Shi,[3] T. S. Luk,[3] A. McPherson,[3] J. C. Solem,[4] K. Boyer,[3] and C. K. Rhodes[3]

[1]*Laboratory for Computer Simulation, Research Computer Center, Moscow State University, Moscow, 119899, Russia*
[2]*General Physics Institute, Academy of Sciences of Russia, Moscow, 117942, Russia*
[3]*Department of Physics, University of Illinois at Chicago, Chicago, Illinois 60680*
[4]*Theoretical Division, Los Alamos National Laboratory, Los Alamos, New Mexico 87545*

(Received 13 November 1991)

Experimental studies examining a new relativistic regime of high-intensity short-pulse propagation in plasmas have been performed which present evidence for the formation of a stable mode of spatially confined (channeled) propagation. For an electron density of $\sim 1.35\times10^{21}$ cm^{-3} and a power of $\sim 3\times10^{11}$ W, the results indicate a channel radius < 1 μm and a peak intensity $\sim 10^{19}$ W/cm^2. Comparison of these findings with a dynamical theory yields agreement for both the longitudinal structure and the radial extent of the propagation observed.

PACS numbers: 52.40.Db, 42.25.−p, 42.65.Jx

A fundamentally new regime of electromagnetic propagation is expected to arise in plasmas for short-pulse radiation at sufficiently high intensity. Calculations of the propagation in plasmas, incorporating both relativistic [1,2] and charge-displacement mechanisms [3–7], indicate that the combined action of these processes can lead to a new stable form of spatially confined (channeled) propagation. This Letter (1) reports the results of the first experimental study probing the physical regime relevant to the observation of relativistic and charge-displacement self-channeling and (2) presents the initial comparison of these experimental findings with matching theoretical calculations performed with the computational procedures described in Ref. [7].

The experimental arrangement used in these studies is illustrated in Fig. 1(a). The source of radiation was a subpicosecond KrF* ($\lambda = 248$ nm) laser that has been described elsewhere [8]. It delivered a linearly polarized power of $\sim 3\times10^{11}$ W (~ 150 mJ, pulse duration ~ 500 fs) in a beam with a diameter of ~ 42 mm. When this radiation was focused into the chamber with lens $L1$ ($f/7$), a focal radius $r_0 \sim 3.5$ μm was measured, giving a maximum intensity $I_0 \sim 8.6\times10^{17}$ W/cm^2. The medium was provided by filling the chamber statically with gas [He, Ne, Ar, Kr, Xe, N_2, CO_2, or a mixture of Xe (4%) and N_2 (96%)] up to a maximum density of $\sim 1.89\times10^{20}$ cm^{-3}.

The diffracted 248-nm radiation was measured as a function of the angle (Θ) with respect to the direction of the incident radiation. The incident laser beam was blocked by a metal disk on the output window of the chamber and lens $L2$ imaged the region near the focal zone on a fluorescent screen S. The diaphragm D in front of lens $L2$ restricted the collection of the diffracted light to a solid angle of $\sim 5°$ while simultaneously increasing the depth of field. The angle between the axis of the lens $L2$ and the axis of the incoming laser radiation could be readily varied up to a maximum angle of $\Theta \sim 15°$. Two flat mirrors coated for high reflection ($\sim 99\%$) at 248 nm, both having a spectral bandwidth of ~ 10 nm, served in reflection as spectral filters (F) for the diffracted laser radiation so that only the scattered 248-nm radiation could illuminate the screen. An attenuator A was employed to adjust the intensity on the screen and the images formed were recorded through the visible fluores-

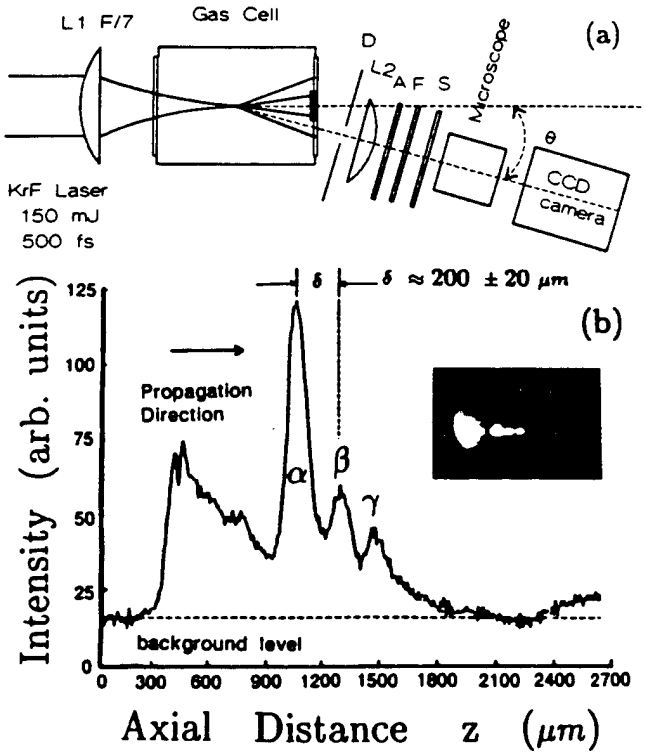

FIG. 1. (a) Experimental apparatus used in studies of propagation. See text for description. (b) Data concerning the pattern of propagation observed with a single pulse in N_2 at a density of $\sim 1.35\times10^{20}$ cm^{-3}. The maximum intensity is half the detector (CCD) saturation. The radiation is incident from the left. Inset: Photographic data with a vertical spatial resolution of ~ 10 μm. The graph illustrates the one-dimensional axial profile taken along the direction of propagation (z) of the photographic data (inset). The spacing of the maxima, $\delta = 200 \pm 20$ μm, is indicated.

cence produced with a microscope and a charge-coupled-device (CCD) camera.

The characteristic behavior observed is well illustrated by the data recorded with N_2. The measured result, shown in Fig. 1(b), corresponds to a density $\rho_{N_2} \sim 1.35 \times 10^{20}$ cm^{-3}. To the left, in the photographic inset, a relatively large cone of light Rayleigh scattered from the plasma is visible at all angles as the energy propagates toward the focal point of the lens, while, in the region to the right of the conical apex, a narrow filament developed. The diameter of this filament is not greater than 10 μm, the measured spatial resolution of the imaging system. The distribution of intensity observed along the filament exhibited several bright features attributed to diffraction because they could not be seen for $\Theta > 20°$. Since the axis of the imaging lens corresponded to an angle $\Theta = 7.5°$, the scale along the abscissa of the photographic data is reduced by almost eightfold, giving the maximum length of the filament as ~ 1 mm. The graph in Fig. 1(b) represents a one-dimensional axial profile, taken along the direction of propagation (z), of the observed intensity pattern (inset). Three peaks (α, β, γ) are visible with a a spatial separation of $\delta = 200 \pm 20$ μm. The normal Rayleigh range for the focal geometry used was ~ 200 μm.

The diameter of the filamentary channel is an important dynamical variable, which we estimated by measuring the maximum angular deviation of the diffracted light. The experimental value ϕ of this diffracted cone was $\phi \sim 20°$, a magnitude indicating a radius $r_\phi \sim 0.9$ μm though the relation $\phi = 1.22\lambda/r_\phi$. Filaments of this general nature were observed at densities above $\sim 1.35 \times 10^{20}$ cm^{-3} in N_2, Ne, Ar, Kr, CO_2, and a mixture of Xe (4%) and N_2 (96%), but not in He and Xe, two materials discussed further below.

Two mechanisms exist that could modify the refractive index of the medium and lead to the observed behavior. They are (1) the Kerr effect stemming from the ions and (2) the relativistic and charge-displacement process [7]. Since the pulse duration is very short (~ 500 fs), the motion of the ions is negligible [3], and no contribution can arise from expulsion of the plasma from the high-intensity zone. An implication of the estimate of the channel radius ($r_\phi \sim 0.9$ μm) is that the observed propagation is associated with intensities in the 10^{18}–10^{19} W/cm^2 range. Under these conditions, available experimental evidence [9,10] on multiphoton ionization indicates that He should be fully ionized and the C, N, and O atoms constituting the molecular materials would retain, at most, only $1s$ electrons.

Consider explicitly the case of N_2, which has estimated [9,10] threshold intensities for the production of N^{5+}, N^{6+}, and N^{7+} of 1.6×10^{16}, 6.4×10^{18}, and 1.3×10^{19} W/cm^2, respectively. Hence, the volume of the channel would be largely ionized to N^{5+}, with certain localized high-intensity regions contributing some N^{6+}. Two consequences of this pattern of ionization follow, namely, (i) the Kerr effect arising from the ions is small, since the polarizabilities of the remaining $1s$ electrons are low, and (ii) the electron density (n_e) initially produced in the focal region is nearly uniform. Therefore, $n_e \simeq 1.35 \times 10^{21}$ cm^{-3} for the data on N_2 shown in Fig. 1(b).

A critical power P_{cr} for self-channeling, arising from the relativistic and charge-displacement mechanism, can be defined [11] as

$$P_{cr} = (m_e^2 c^5/e^2) \int_0^\infty g_0^2(r) r\, dr\, (\omega/\omega_{p,0})^2 \simeq 1.62 \times 10^{10} (n_{cr}/n_e)\ \mathrm{W}, \quad (1)$$

where m_e, e, and c have their customary identifications, ω is the laser angular frequency, $\omega_{p,0}$ is the plasma frequency for the uniform unperturbed plasma with electron density n_e, n_{cr} is the critical electron density (for $\lambda = 248$ nm, $n_{cr} = 1.82 \times 10^{22}$ cm^{-3}), and $g_0(r)$ is the Townes mode [12].

The critical powers associated with the experimental conditions, for He and N_2 at a medium density $\rho = 1.35 \times 10^{20}$ cm^{-3}, are 1.08×10^{12} and 2.19×10^{11} W, respectively. Therefore, since the incident power was $P \simeq 3 \times 10^{11}$ W, no filament was expected in He, a prediction conforming with the observation of none. Moreover, the diffracted cone of radiation was also absent with He. In contrast, $P/P_{cr} \simeq 1.37$ for N_2, a condition that held generally ($P/P_{cr} > 1$) for all materials which exhibited evidence for channel formation. We note, however, that some contribution from the Kerr effect may be present, even for the light materials (Ne, N_2, and CO_2), in the early stage of channel formation prior to the development of a substantial level of ionization, and that the heavier gases (Ar, Kr, and Xe) may involve a more significant influence from the Kerr process. A specific estimate of the nonlinear index change arising from both N^{5+} and N^{6+} at an intensity of $\sim 10^{19}$ W/cm^2 indicates that their contribution is less than 10^{-3} that of the free electrons; hence the ionic contribution can be neglected in N_2 for the conditions studied.

A direct comparison will now be made between the theoretical analysis, fully described in Ref. [7], and the experimental findings for N_2. This comparison can be accomplished for both the longitudinal intensity profile and the radial extent of the channel. Figure 2(a) illustrates the intensity profile $I(r,z)/I_0$ calculated with physical parameters corresponding to those of the experiment (i.e., $P \simeq 3 \times 10^{11}$ W, $r_0 = 3.5$ μm, $n_e = 1.35 \times 10^{21}$ cm^{-3}, and $P/P_{cr} = 1.37$). Importantly, *all* of these parameters are based on *independent* measurements of (1) the laser pulse involving determinations of the energy and power (P), (2) the focal radius (r_0) of the incident radiation, and (3) the characteristics of the multiphoton ionization [10] generating the electron density (n_e). Therefore, this comparison does *not* involve a fit with a free parameter. The normalized electron density calculated is presented in Fig. 2(b), from which it is seen that electronic cavitation occurs only near the positions of the maxima in the intensity profile [Fig. 2(a)]. Curve A in Fig. 2(c) represents

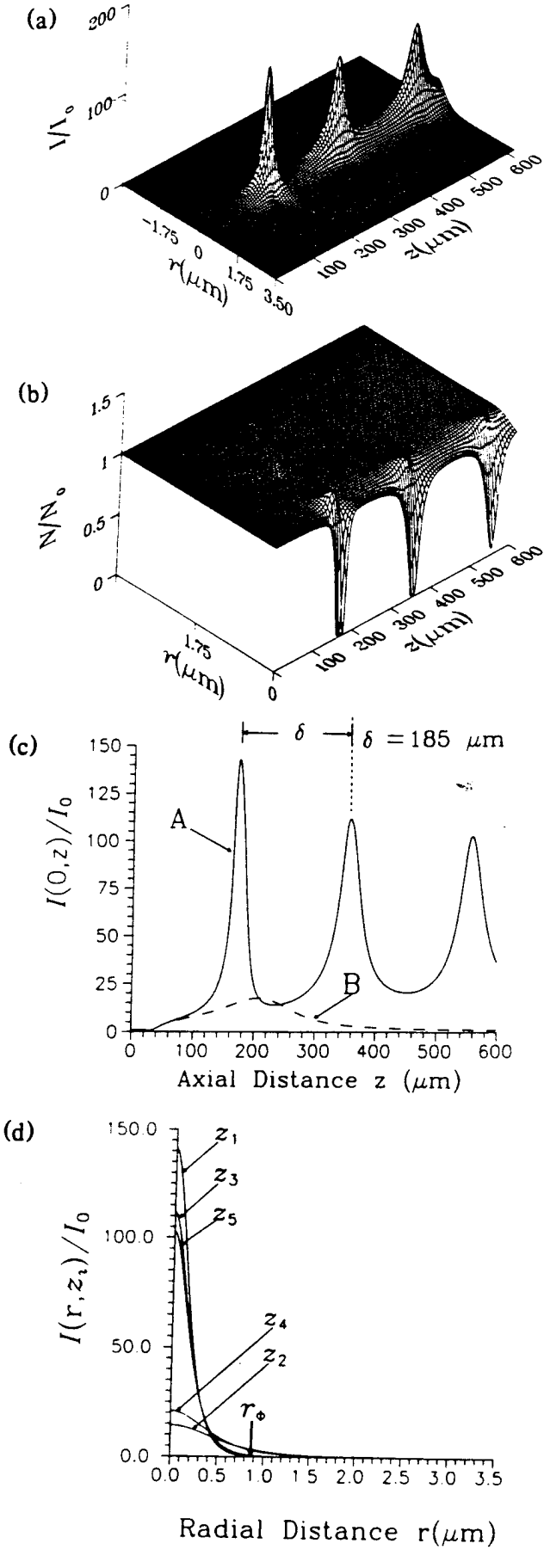

the one-dimensional axial intensity profile $I(0,z)/I_0$ corresponding to the calculated distribution shown in Fig. 2(a). The spacing (δ) of the maxima is seen to be $\delta \sim 185$ μm, a value in close agreement with the experimental figure ($\delta = 200 \pm 20$ μm) illustrated in Fig. 1(b). Furthermore, analysis has shown that the spacing δ is quite sensitive to the power P_0 and electron density n_e, particularly in the region close to the threshold [see Eq. (1)]. With respect to the results illustrated in Fig. 2(c), an increase in n_e by less than 5% causes a reduction in the spacing δ by approximately 25%. Therefore, substantial changes in the physical parameters would grossly alter the comparison of the experimental and theoretical results.

Theoretical studies [3–7,11] indicate that the charge displacement plays a very important dynamical role. In order to test this hypothesis, identical calculations were made for N_2 for the purely relativistic case [2] which explicitly neglects the charge-displacement term, namely, elimination of the term $(c^2/\omega_{p,0}^2 r_0^2)\Delta_\perp(1+I/I_r)^{1/2}$ in Eq. (24) of Ref. [7]. Significantly, the resulting axial profile [curve *B* in Fig. 2(c)] exhibits only a *single* relatively weak maximum, for $0 \le z \le 600$ μm, an outcome sharply at variance with both the full theoretical analysis and the experimental observation. Although the expected charge displacement is highly localized [Fig. 2(b)], this comparison reveals the strong influence it has on the propagation [3,7,11]. At a greater incident power ($P/P_{cr} \sim 10$), a continuous channel in the electron distribution is expected to develop [7].

The measurements indicated an approximate value of $r_\phi \simeq 0.9$ μm for the radial extent of the channel, a result that can be compared with the corresponding theoretical figure. Figure 2(d) illustrates five radial intensity profiles $I(r,z_i)/I_0$ of the distribution pictured in Fig. 2(a). Since the measurement of this angularly scattered radiation did not correspond to a known longitudinal position, this comparison can only be qualitative, but the radial distributions shown indicate that the expected value lies in the interval $0.5 \le r \le 1.0$ μm, a range that comfortably includes the experimental value r_ϕ.

The results observed with Xe deserve additional discussion, since those experiments did not give evidence for the formation of a channel. In significant contrast to the case involving N_2, the electron density n_e produced by the multiphoton ionization [10] in Xe is expected to be very

FIG. 2. Calculations for N_2 with $P = 3\times10^{11}$ W, $r_0 = 3.5$ μm, $n_e = 1.35\times10^{21}$ cm^{-3}, and $I_0 = 8.6\times10^{17}$ W/cm^2. (a) Normalized intensity $I(r,z)/I_0$. (b) Normalized electron density $N(r,z)/N_0$ for N_2 with $N_0 = n_e$. (c) Normalized one-dimensional axial intensity profiles $I(0,z)/I_0$. Curve *A*, full theory for data in panel (a), $\delta = 185$ μm. Curve *B*, calculation with charge-displacement term neglected. (d) Normalized radial intensity profiles $I(r,z_i)/I_0$ corresponding to panel (a). Longitudinal positions $z_1 = 172$ μm, $z_2 = 245$ μm, $z_3 = 358$ μm, $z_4 = 441$ μm, and $z_5 = 559$ μm and $r_\phi = 0.9$ μm.

nonuniform spatially. For intensities spanning 10^{16}–10^{18} W/cm^2, the corresponding density n_e would vary by over a factor of 2. Since this nonuniformity would tend to reduce the refractive index locally in the central high-intensity region, a significant defocusing action is expected which could suppress the channel formation.

Finally, we note (1) that the intensity distribution is not expected to depend strongly on the state of polarization [13,14] and (2) that losses to the plasma may be significant, particularly at electron densities close to n_{cr}.

The first experiments examining a new relativistic regime of high-intensity pulse propagation in plasmas have been performed and the findings indicate the formation of a channeled mode of propagation over a length considerably greater than the Rayleigh range. Specific comparisons of the experimental observations with a dynamical theory, which explicitly includes both the influence of the relativistic mass shift and the displacement of the electronic component of the plasma, produce excellent agreement for both the longitudinal structure of the intensity profile and the radial extent of the channel. While the present channel contains several foci, a continuous channel is predicted to develop at higher power. Finally, the intrinsically very high concentration of power associated with this mechanism of channeled propagation provides an efficient and general method for the production of conditions necessary for x-ray amplification [15].

The authors acknowledge the expert technical assistance of J. Wright and P. Noel in addition to fruitful conversations with A. R. Hinds, R. R. Goldstein, and B. Bouma. Support for this research was partially provided under Contracts No. AFOSR-89-0159, (ONR) No. N00014-91-J-1106, (SDI/NRL) No. N00014-91-K-2013, (ARO) No. DAAL 3-91-G-0174, (DOE) No. DE-FG02-91ER12108, and (NSF) No. PHY-9021265.

[1] C. Max, J. Arons, and A. B. Langdon, Phys. Rev. Lett. **33**, 209 (1974).
[2] A. B. Borisov, A. B. Borovskiy, V. V. Korobkin, A. M. Prokhorov, C. K. Rhodes, and O. B. Shiryaev, Phys. Rev. Lett. **65**, 1753 (1990).
[3] J. C. Solem, T. S. Luk, K. Boyer, and C. K. Rhodes, IEEE J. Quantum Electron. **25**, 2423 (1989).
[4] P. Sprangle, E. Esarey, and A. Ting, Phys. Rev. Lett. **64**, 2011 (1990); P. Sprangle, C. M. Tang, and E. Esarey, Phys. Rev. A **41**, 4463 (1990); A. Ting, E. Esarey, and P. Sprangle, Phys. Fluids B **2**, 1390 (1990).
[5] G. Z. Sun, E. Ott, Y. C. Lee, and P. Guzdar, Phys. Fluids **20**, 526 (1987).
[6] T. Kurki-Suonio, P. J. Morrison, and T. Tajima, Phys. Rev. A **40**, 3230 (1989).
[7] A. B. Borisov, A. V. Borovskiy, O. B. Shiryaev, V. V. Korobkin, A. M. Prokhorov, J. C. Solem, T. S. Luk, K. Boyer, and C. K. Rhodes, Phys. Rev. A (to be published).
[8] T. S. Luk, A. McPherson, G. Gibson, K. Boyer, and C. K. Rhodes, Opt. Lett. **14**, 1113 (1989).
[9] S. Augst, D. Strickland, P. D. Meyerhofer, S. L. Chin, and J. H. Eberly, Phys. Rev. Lett. **63**, 2212 (1989).
[10] G. Gibson, T. S. Luk, and C. K. Rhodes, Phys. Rev. A **41**, 5049 (1990).
[11] A. B. Borisov, A. V. Borovskiy, V. V. Korobkin, A. M. Prokhorov, O. B. Shiryaev, and C. K. Rhodes, J. Laser Phys. **1**, 103 (1991).
[12] R. Y. Chiao, E. Garmire, and C. H. Townes, Phys. Rev. Lett. **13**, 479 (1964).
[13] P. Avan, C. Cohen-Tannoudji, J. Dupont-Roc, and C. Fabre, J. Phys. (Paris) **37**, 993 (1976).
[14] S. V. Bulanov, V. I. Kirsanov, and A. S. Sakharov, Fiz. Plazmy **16**, 935 (1990) [Sov. J. Plasma Phys. **16**, 543 (1990)].
[15] K. Boyer, A. B. Borisov, A. V. Borovskiy, O. B. Shiryaev, D. A. Tate, B. E. Bouma, X. M. Shi, A. McPherson, T. S. Luk, and C. K. Rhodes, "Method of Concentration of Power in Materials for X-Ray Amplification" (to be published).

Appendix G: "Ultrahigh Power Compression for X-Ray Amplification: Multiphoton Cluster Excitation Combined with Nonlinear Channeled Propagation"

ULTRAHIGH POWER COMPRESSION FOR X-RAY AMPLIFICATION: MULTIPHOTON CLUSTER EXCITATION COMBINED WITH NONLINEAR CHANNELED PROPAGATION*

A. B. Borisov, A. McPherson, B. D. Thompson, J. W. Longworth†,
K. Boyer, and C. K. Rhodes

Laboratory for Atomic, Molecular, and Radiation Physics
Department of Physics, M/C 273, University of Illinois at Chicago
845 W. Taylor Street, Room 2136, Chicago, IL 60607-7059
Phone: (312) 996-4868
FAX: (312) 996-8824
E-mail: Rhodes@uic.edu

---

† Permanent address, Department of Physics, Illinois Institute of Technology, Chicago, IL 60616

* J. Phys. B, in press

ABSTRACT

The ability to apply power densities controllably at or above vigorous thermonuclear levels ($> 10^{19}$ W/cm^3) in materials is the basic issue for achieving efficient amplification of X-rays. Recent experimental and theoretical findings concerning (1) the multiphoton production of X-rays from clusters and (2) high-intensity modes of channeled propagation in plasmas indicate an entirely new method for producing the conditions necessary for strong amplification in the multi-kilovolt range. These two new nonlinear phenomena are being united to produce and control the imperative power compression; the multiphoton mechanism serves to establish the condition locally while the confined propagation provides the required spatial organization. The present work, which experimentally demonstrates the first combined expression of these two complex nonlinear processes through direct X-ray imaging of Xe(M) emission ($\sim$ 1 keV) in stable self-trapped channels, (α) reveals the exceptional compatibility of their mutual scaling for realizing the necessary power density, (β) provides confirming evidence for the action of a superstrong coherent multi-electron intense-field interaction in the X-ray generation from the Xe clusters, and (γ) furnishes new detailed information on the dynamics of the radial intensity distributions associated with the channeled propagation. The resulting knowledge of the scaling relations underlying these phenomena enables the optimum conditions for amplification to be specified up to a quantum energy of $\sim$ 5 keV. The harmonious use of these new nonlinear processes is expected to lead to an advanced generation of extraordinarily bright X-ray sources in the multi-kilovolt region having a peak brightness of $\sim 10^{31}$-10^{33} γs^{-1} (mrad)$^{-2}$ (mm)$^{-2}$ (0.1 % BW)$^{-1}$, a level sufficient for biological holographic imaging capable of providing a high resolution visualization of the molecular anatomy of cells, tissues, and organisms in the natural state.

Stable channeled propagation of subpicosecond (248 nm) radiation arising from relativistic-charge-displacement nonlinearities [1] has been observed [2,3] in underdense plasmas. Experimental tests [4] of a concept [5] for a molecular design associated with multiphoton X-ray production induced by a strong nonlinear interaction have shown that copious Xe(M), Kr(L), and Xe(L) emission can be generated with corresponding Kr and Xe clusters in the 1-5 keV region [4,6-8]. The experiments demonstrated that high X-ray yields could be readily produced from gaseous targets and estimates stemming from the observed X-ray spectra indicated the achievement of maximal atom-specific energy transfer rates of ~ 0.1-1.0 W/atom.

The present work (1) demonstrates a compatible unification of the physical conditions governing the combined expression of these two highly nonlinear phenomena, (2) provides data corroborating the presence of a superstrong multiphoton interaction in the X-ray production from the clusters [6-9], and (3) gives important new information on the properties of the radial intensity profiles produced by the nonlinear propagation. The outcome is a congruous picture of the mutual scaling of these processes that enables a general specification of the optimum conditions necessary for amplification up to a quantum energy of ~ 5 keV.

Calculations have shown that the observed characteristics of the channeled propagation [1] can be put in close correspondence [2,3] with a theoretical picture incorporating relativistic [10,11] and charge-displacement [12-18] mechanisms. In particular, those studies indicated that intensities as high as ~ 10^{20} W/cm^2 were dynamically produced in the narrow channels formed [2,3], a value sufficient for the copious multiphoton generation of multi-kilovolt X-ray emission from Kr and Xe clusters [4-8]. Therefore, the use of a medium composed of Kr or Xe clusters presents the opportunity for a study combining the dynamics of the confined propagation and the

properties of the nonlinear cluster excitation through direct X-ray imaging of the high-intensity zones produced by the channeling. We describe below the results obtained by using Xe(M) emission ($\sim$ 1 keV) generated from Xe clusters in channels produced with subpicosecond 248 nm radiation.

The experimental arrangement used to conduct spectroscopic studies of rare gas clusters has been described elsewhere [6]. The laser [19] used had a wavelength of 248 nm, a pulse width of $\sim$ 300 fs, a power of $\sim$ 0.7 TW, and was focused to a maximum intensity of $\sim 10^{19}$ W/cm^2 with an f/3 off-axis parabolic mirror in a gas target. This target was hydrodynamically produced by a cooled high-pressure pulsed-valve fitted with a circular sonic nozzle having a diameter of $\sim$ 0.5 mm. In order to eliminate distortion and absorption of the incident beam as it approached the focal zone through the outer regions of the material produced by the nozzle [20], a barrier with a $\sim$ 100 μm hole was positioned near the opening of the nozzle as shown in the inset in Fig. 2(b). The focus of the f/3 mirror was then placed at the position of the opening in the barrier so that the initial conditions of medium density and laser intensity corresponding to the launching of the wave were well defined.

Previous spectroscopic studies [6] have demonstrated that bright Xe(M) emission spanning the 9.5-16 Å region is readily produced from Xe clusters. In order to record the spatial pattern of the propagation, this emission was observed with an X-ray "pinhole" (CCD) camera. The camera was an Electrum EDC1000 using a video chip having a 196 $\times$ 165 pixel array with an individual pixel size of 13.5 μm $\times$ 16 μm. The X-ray images were obtained by viewing the region excited by the focused 248 nm radiation directly below the pulsed-jet in a direction transverse to the propagation of the 248 nm beam. For images of the Xe(M) emission,

the camera was equipped with a filter with the composition (2000 Å Al + 1 μm polycarbonate + 10 μm Be) and, consequently, detected all radiation with a quantum energy $\hbar\omega_x \gtrsim 700$ eV. When the camera was equipped with a $\sim$ 25 μm pinhole and positioned to give a magnification factor of 1.18, the brightness of the Xe(M) emission was sufficiently high that recordings of single-shot exposures could be obtained. Given the magnification used and the geometry of the pixel, the pinhole camera has a predicted limiting spatial resolution $\Delta \sim 30$ μm, a property verified by the observed characteristics of the images described below.

Examples of the X-ray images recorded for two different densities of the Xe medium are illustrated in Figs. 1(a) and 2(a), respectively. The former shows a strongly longitudinally modulated distribution while the latter demonstrates that a highly uniform distribution can be produced under appropriate conditions. The corresponding axial X-ray intensity distributions (radius r = 0 line-outs of these data), which are represented in Figs. 1(b) and 2(b), are found to be in good correspondence with the matching theoretical distributions shown in Figs. 1(c) and 2(c). Significantly, as in the earlier study [2], all the parameters involved in the computed distributions are based on quantities derived from independent measurements, so that the comparisons with the experimental results are sharply defined and do not involve a fit with any free parameters. Importantly, the conditions of these experiments also corresponded to the zone of stable confined propagation previously found in an analysis of the response of the channeled power distribution to small azimuthal perturbations [16,18], a point shown explicitly below. Furthermore, all the computed results illustrated in Figs. 1 and 2 allow for the variation of the density of the medium caused by the hydrodynamic expansion from the nozzle [21].

Of chief interest in the present context is the radial dependence of the X-ray images,

since the behavior of the transverse dimension of the emitting region represents a sensitive probe of both the dynamics of the propagation and the mechanism of excited state production in the clusters. Consider the image shown in Fig. 2(a), which has a transverse width of ~ 120 μm at its midpoint ($z \cong 1050$ μm). This width is considerably greater than the resolution ($\Delta \sim 30$ μm) of the camera and both the observed and calculated values [~ 2 μm] associated with the confined propagation of the 248 nm radiation [2,3]. Consequently, the measurement shows unambiguously that X-rays are being produced well outside the small central core of the channel that confines the propagation of the 248 nm energy. In addition, the image shown in Fig. 1(a) clearly demonstrates that the radial extent of the X-ray emission can have a significantly structured longitudinal (z) dependence.

The existence of a bright emitting zone having a diameter of ~ 100 μm and the observed longitudinal signature in the radial structure is inconsistent with either (a) collisional excitation arising from energetic electrons produced in the core of the channel or (b) recombination into excited states of highly ionized ions which migrate radially from the central region. At the outset we see that the largest observed radial dimension in Fig. 2(a) is greater than the corresponding maximum value in Fig. 1(a), although the density of the medium in the former is significantly higher than in the latter. This trend is exactly the opposite of that expected for the range of energetic charged particles, either electrons or ions, in matter. Furthermore, if the origin of the X-ray emission were to arise from collisional excitation by electrons expelled from the channel through the effect of the ponderomotive potential, then it should be possible to relate the observed radial size of the emitting region to an estimate of the maximum range of electrons [22] in materials with the known range-energy [23] relationships. Specifically, since the data in

Figs. 1(c) and 2(c) show that the peak intensity in the channel is expected to fall in the 10^{19}-10^{20} W/cm^2 region, for electrons having kinetic energies on the scale of the ponderomotive potential ($\sim$ 100-500 keV), the expected range would be $\sim$ 100 mg/cm^2. The corresponding distance would exceed several centimeters for the prevailing experimental conditions, a value in clear conflict with the data. Of course, only a rather small fraction of electrons would be expected to behave in this fashion, since the energy associated with the charge separation would otherwise be too great.

Energetic ions can also be ruled out as the source of the extended region of emission. It can be readily seen from data on ion ranges in materials [24] that the Xe ion kinetic energy necessary to produce the observed depth of penetration ($\sim$ 100 μg/cm^2) is $\sim$ 0.5-1.0 MeV. This required energy is far above the value that could be produced by the coulomb explosion of a cluster under our experimental conditions. For example, the maximum kinetic energy of Xe ions generated in the disintegration of a Xe_{125} cluster irradiated at $\sim$ 10^{19} W/cm^2 would be $\leq$ 60 keV.

The remaining possibility is direct excitation of the clusters throughout the observed radiating zone, a mechanism requiring fulfillment throughout that region of the conditions specified by the allowed zones governing prompt X-ray emission [4-6]. The threshold intensity for the generation of Xe(M) emission from Xe clusters has been independently determined experimentally [6] to be $\sim$ 3 x 10^{15} W/cm^2. Significantly, this experimental value was found to be substantially lower than the minimum value predicted ($\sim$ 4 x 10^{16} W/cm^2) with the original formulation of the multiphoton cluster interaction [5], a conclusion that followed independent of the distribution of cluster sizes involved in the study [6,9]. Since the full

ponderomotive potential of a free electron is considerably less than 100 eV at an intensity of ~ 3×10^{15} W/cm^2 for irradiation with a wavelength of 248 nm, the available energy of a single electron is well below the threshold energy [25,26] (M_5 ~ 675 eV) needed for M-shell ionization in Xe. However, a generalization of the cluster interaction, incorporating an enhancement in the coupling strength for inner-shell excitation arising from the coherent motion [9,27,28] of the (Z) field-ionized [29] electrons induced by the external driving field, reduced the required threshold intensity to ~ 3.8×10^{15} W/cm^2, a value agreeing with the experimental determination within the uncertainty of measurement [6]. Physically, the extension of the allowed region to lower intensities arises, because the Z (field-ionized) coherently driven electrons, individually having a mass m, act like a quasi-particle [6,8,9,27] with mass Zm and charge Ze. In this situation, the single particle energies add [27] so that the required excitation energy [5] of the inner-shell state ϵ_e can be shared in the interaction. Consequently, this feature of the interaction leads to a Z-fold reduction in the necessary single-particle energy, thereby, substantially extending the allowed zone by lowering the threshold condition [6] to the boundary I_0' shown in Fig. 3. Since the radial extent of the X-ray emission from the channels can be directly related to this threshold intensity (I_0'), the minimum value of which is designated as $I_{\beta'}$ in Fig. 3, images of the emitting region can give critical information on the existence and properties of the coherent interaction.

An evaluation of the radial distance over which conditions exist corresponding to the allowed zone for Xe(M) emission requires knowledge of the radial profile of the intensity distribution of the 248 nm radiation supported by the channeled propagation. The characteristic form of this radial intensity distribution, for conditions corresponding to the Xe(M) emission

shown in Fig. 2(a) at z = 1050 μm, is illustrated in Fig. 4. This distribution, evaluated as a function of longitudinal position (z), can be used to determine the radial locus of the threshold intensity for Xe(M) emission. It is important to note that, since the confined 248 nm radiation propagates in a channel that acts as a dielectric waveguide, a substantial field can exist at radial positions far exterior to the narrow high-intensity core. This important characteristic is plainly exhibited by the radial intensity profile illustrated in Fig. 4. Indeed, for a threshold value of I_{th} $\sim 3 \times 10^{15}$ W/cm^2, Fig. 4 indicates a maximum radius of $\sim$ 27 μm, a value more than ten-fold the radius of the central high intensity zone [2,3]. This radial characteristic of the propagating field greatly enlarges the effective volume of the channel for X-ray generation and, consequently, is a crucial feature of the joint action of these two nonlinear processes.

Three significant comparisons of the experimental data with corresponding theoretical findings can be made through referral to the radial dependence shown in Fig. 4. The three indicated situations concerning the threshold intensity for Xe(M) radiation are the following: (α) The experimentally determined threshold [$I_{th}(\alpha) \cong 3 \times 10^{15}$ W/cm^2] is shown, a value which agrees closely with the theoretical magnitude $I_{\beta'}$ shown in Fig. 3 that arises with the inclusion of the coherent electronic motions [6,9]. This choice, as noted above, corresponds to a maximum radius of r(α) $\sim$ 27 μm. (β) The threshold intensity that would apply [5], if the coherent interaction were absent, is $I_{th}(\beta) \cong 4 \times 10^{16}$ W/cm^2. This case corresponds to a relatively small radial extent of r(β) $\sim$ 2 μm. (γ) The value [$I_{th}(\gamma) \cong 9.5 \times 10^{13}$ W/cm^2] is also shown, the threshold determined by matching the observed radial size [r(γ) $\sim$ 60 μm] of the X-ray emitting region to the computed distribution.

The theoretical radial loci for the former two threshold intensities (α and β) are compared

to the corresponding experimental data in Figs. 1(d) and 2(d). Particularly significant is the strong dependence experimentally observed at z ~ 1250 μm (locus A) in Fig. 1(d) and the matching feature that is clearly present in the computed locus (B) for the threshold [$I_{th}(\alpha)$] incorporating the coherent electronic process. In contrast, the locus (C) in Fig. 1(d), which corresponds to the threshold [$I_{th}(\beta)$] that would apply without the coherent process, does not exhibit this structure and differs grossly in magnitude and in form from both the experimental measurements (A) and that calculated with the threshold involving the coherent coupling (B). Finally, as seen from Fig. 4, a channel radius of r(γ) ~ 60 μm, the magnitude matching the measured value, could only result if the threshold intensity [$I_{th}(\gamma)$] were reduced to ~ 10^{14} W/cm^2. However, since the ponderomotive potential is ~ 1 eV at this intensity and measurements have shown that electron heating plays a negligible role in producing the observed X-ray emission [7], there exists no physical basis for a threshold this low and this possibility is ruled out. Therefore, it is not possible to reconcile either the shapes or the magnitudes of the calculated radial loci with the experimental measurements without the enhanced coupling characteristic of the coherent mechanism [6,9].

The results illustrated in Fig. 1(d) and 2(d) show that the calculated radial loci for the case involving the coherent motion [$I_{th}(\alpha)$ in Fig. 4] fall consistently below the measured values by a factor of ~ 2. Since the field occurring in the region exterior to a dielectric waveguide is sensitive to the detailed structure of the radial index profile [30], small inaccuracies in the computation of the electron hydrodynamics and the resulting radial electron density distributions could cause the observed differences. In the current formulation, the theory [1] calculates the electron density by assuming the instantaneous establishment of a force balance between the

radially outward ponderomotive force and the oppositely directed electrostatic restoring force. Since the true electronic motions are not instantaneous [31], this computational procedure has the proclivity to maximize the displaced charge and, consequently, to overestimate the refractive confinement of the channel. The outcome is the collateral tendency to underestimate the field intensity outside the radial zone carrying the main channeled power. The effects of electron collisions and an electron temperature $T_e > 0$, which are also neglected, would produce a similar influence.

The present experiment is a particularly discriminating probe of the dynamics of the electron density, since the radial extent of the Xe(M) emission is highly sensitive to variations in the radial intensity profile of the channeled 248 nm radiation. As shown in Fig. 4, there generally exists a broad second maximum (I_m) in the intensity profile. When $I_{th} \sim I_m$, the situation corresponding to the case $I_{th}(\alpha)$ involving the coherent interaction, a modest change in the value of I_m can lead to relatively large changes in the radius of the emitting zone. Specifically, a decrease in the value of I_m by a factor of only ~ 3 leads to a fourteen-fold reduction in the radius of the emitting region; the transverse dimension of the emitting zone collapses.

It has been possible to establish experimental conditions under which this radial collapse can be controlled and Fig. 5(a) illustrates a demonstration of this phenomenon. Since the plasma density n_e will slowly pass through a maximum as the propagating channel transverses the spatially inhomogeneous hydrodynamically produced target, and since the critical power P_{cr} depends inversely on n_e [1], it is possible to produce the conditions $\eta_o < 1$, $\eta_o \geq 1$ with $I_m < I_{th}(\alpha)$, and $\eta_o < 1$ sequentially along the path of propagation. Under these circumstances,

the observed X-ray emission will suddenly undergo radial collapse as the channel forms, exhibit a narrow extended zone of propagation because $I_m < I_{th}(\alpha)$, and abruptly resume the expanded profile when the critical condition ($\eta_o \geq 1$) for confined propagation again fails to be satisfied. This pattern of emission conforms to the observed distribution shown in Fig. 5(a). Figure 5(b) illustrates the radial profile of the Xe(M) emission at a point ($z = 956\ \mu m$) in the narrow region, the characteristic width of which matches the estimated spatial resolution limit of the measurement $\Delta_m \sim \Delta \sim 30\ \mu m$.

For the sensitive conditions of this study, the difference of a factor of ~ 2 between the calculated and observed radii shown in Figs. 1(d) and 2(d) indicates that the level of approximation used to calculate the electron distribution is sufficiently good that it leads to a reasonable assessment of the intensity profile of the propagating mode. Although further study is required to verify these hypotheses concerning the electron hydrodynamics, we tentatively attribute the difference in the calculated and observed loci to the specific approximations used in calculating the distribution of the displaced charge that is dynamically generated by the channeled propagation.

The information on the scaling relationships governing the cluster excitation and the confined propagation revealed in these studies has exceptionally important implications for their effective cooperative action. The results show how a judicious design can harness these two very different nonlinear processes to produce harmoniously conditions ideal for X-ray amplification. Specifically, in order to convert a substantial quantity of energy efficiently, we require (1) that the range of intensities characteristic of the propagating channel conform to the span of intensities specified by the corresponding allowed zone for core-state excitation of the

clusters [4-6] and (2) that this overlap in conditions involving the propagating energy encompass a large spatial volume. The simultaneous fulfillment of these two requirements constitutes a specification of the optimum conditions for X-ray amplification.

In order to illustrate the procedure involved in establishing this optimum, we will refer to the information concerning the Xe(M) emission presented in Figs. 3 and 4. It is known from the analysis [1] of relativistic and charge-displacement self-channeling that a critical power P_{cr} and a normalized radius of the lowest eigenmode ρ_{eig} exist which enable the peak intensity in the channel I_{ch} to be expressed as

$$I_{ch} = \left(\frac{4\pi\eta_{ch}}{\rho_{eig}^2}\right)\left(\frac{m^2c^5}{e^2\lambda^2}\right)\int_0^\infty g_o^2(\rho)\rho d\rho \qquad (1)$$

where $\eta_{ch} \equiv P_{ch}/P_{cr}$ and P_{ch} represents the power in the channel [32]. Furthermore, since the normalized radius of the eigenmode [3] is nearly constant ($\rho_{eig} \cong 1.7$) over the range of principal interest ($1.4 \leq \eta_{ch} \leq 10$), Eq. (1) reduces to the simple expression

$$I_{ch} \approx 7 \times 10^{18}\frac{\eta_{ch}}{\lambda^2} \quad W/cm^2 \qquad (2)$$

with λ given in units of micrometers. The computed value of I_{ch} for the conditions corresponding to the data shown in Fig. 2 ($\lambda = 0.248\ \mu m$, $\eta_{ch} = 1.36$) is indicated on Fig. 4. Furthermore, it was generally found that for conditions of interest the ratio [1] η_{ch}/η_o was restricted to the narrow range $0.5 \leq \eta_{ch}/\eta_o \leq 0.7$.

Since we seek ideally to bound the upper intensity produced in the channel with the maximum of the allowed zone shown in Fig. 3, we desire the condition

$$I_{ch} \approx I_{max}(N). \qquad (3)$$

Moreover, since the relevant $I_{max}(j)$ [e.g. $I_{max}(N)$] can be readily determined [5] for any

shell(j) for any atom from a tunneling picture involving known atomic parameters [29], Eq. (3) can be simply and generally evaluated. For a given atomic shell, this results in a relationship between the wavelength (λ) and the atomic number of the atom.

The analysis of the radial dependence of the observed X-ray emission discussed above showed that a large increase ($\sim 10^2$) in the volume is obtained if the condition

$$I_{\beta'} < I_m \tag{4}$$

holds, the actual situation illustrated in Fig. 4 for the Xe(M) emission. The threshold intensity $I_{\beta'}$ can be evaluated from the known constraints on the allowed zone [5,6,33], a procedure which involves atomic spectroscopic data, the interatomic spacing r_o in the cluster, and the wavelength λ. The corresponding value of I_m is determined by the dynamics of the propagation, a calculation [1-3] which incorporates the electron density n_e, the wavelength λ, and the incident power P_o. Although highly nonlinear, fast numerical methods can readily determine the optimal zone of the multidimensional problem stated by Eqs. (3) and (4) subject to the sole constraint that the plasma is underdense, a condition necessary for propagation to occur. The outcome, for a specific atomic shell and a given incident power P_o, is a specification of the wavelength λ, the plasma density n_e, and the cluster structural parameter r_o.

Explicit calculations have revealed important characteristics of this procedure for optimization. We consider the special situation involving a fixed wavelength (λ = 248 nm) and a power $P_o \sim 1$ TW, since these experimental parameters can be practically produced [19] and data for these conditions exist. The two principal features of the scaling that emerged are (1) the existence of a short wavelength limit λ_x that can be amplified under the optimized conditions and (2) the strong tendency for the optimum conditions to occupy a small zone in the available

space of parameters. Concerning the former, a limiting value of λ/λ_x is expected to exist arising from the natural physical bounds on plasma density and intensity associated with the production of stable channels [16,18] with radiation at wavelength λ. Exploration of this question has led to the limit $\lambda/\lambda_x \sim 10^3$. A good example of a system representing this limiting behavior concerns the generation of U(M) emission [34-36] in the 4-6 keV range from U clusters.

Analysis of the conditions representing optimization following the procedure outlined above, which concentrated on transitions in the ~ 0.7 keV to ~ 5 keV range, led to the result shown in Fig. 6. The optimal zone is circumscribed by the small rectangle near the center of the stable channeling region [16,18]. Points A and B correspond to optimization of Xe(M) emission from Xe clusters (r_0 = 4.4 Å) with radiation at 248 nm having P_0 = 1 TW and P_0 = 1.5 TW, respectively. Consideration of the variation of the atomic and molecular parameters for other systems showed that the resulting optimum condition was weakly dependent on these variations over the relatively narrow ranges physically possible. Hence, the optimal zone is highly localized and the rectangular region in Fig. 6 is drawn to indicate its estimated extent. The chief result is that the optimal conditions for amplification up to ~ 5 keV occupy a relatively small zone that is centrally located in the stable region.

The conditions corresponding to the experimental data shown in Fig. 1 and Fig. 2 are designated in Fig. 6 by points E1 and E2, respectively, both of which are at locations significantly removed from the optimal region. However, comparison of the images shown in Figs. 1(a) and 2(a) clearly shows that significantly greater emission occurs for the latter (E2). This result is fully consistent with the analysis given above, since as one travels from E1 to E2

in Fig. 6, the movement is directly toward the specified optimal zone.

In conclusion, the ability to controllably apply power densities comparable to thermonuclear levels is a fundamental requirement for achieving the amplification of X-rays. Two new nonlinear phenomena involving (1) the multiphoton production of X-rays from clusters and (2) channeled propagation are being united to produce and control the required power density. Experiments showing the first combined expression of these two complex nonlinear processes have provided confirming evidence for the action of a superstrong coherent multi-electron intense-field interaction in the X-ray generation from the clusters and furnished new detailed information on the dynamics of the propagation. A crucial result is the demonstration of the exceptional compatibility of the mutual scaling of these phenomena for realizing the conditions necessary for efficient amplification in the multi-kilovolt spectral region. Most importantly, the knowledge obtained in these studies shows explicitly how the optimum conditions for amplification can be easily, generally, and narrowly specified up to a quantum energy of $\sim$ 5 keV. The combined use of these nonlinear processes is expected to lead to an advanced generation of extraordinarily bright X-ray sources in the multi-kilovolt region having a peak brightness of $\sim 10^{31}$-10^{33} γs^{-1} $(mrad)^{-2}$ $(mm)^{-2}$ $(0.1\ \%\ BW)^{-1}$, a level sufficient for the performance of microholographic assays of living cells, tissues, and organisms.

ACKNOWLEDGEMENTS

The authors acknowledge the expert technical assistance of J. Wright and P. Noel. Support for this research was provided under contracts with DoE, AFOSR, SDI/NRL, ARO and NSF. MCR Technology Corporation is also acknowledged for partial support of the computational research.

REFERENCES

1. A. B. Borisov, A. V. Borovskiy, O. B. Shiryaev, V. V. Korobkin, A. M. Prokhorov, J. C. Solem, T. S. Luk, K. Boyer, and C. K. Rhodes, Phys. Rev. A 45, 5830 (1992). Confinement of the propagating energy results from the compensation of normal diffraction by the refractive focusing generated by relativistic effects and the ponderomotively radially displaced electron density. Generally, the conditions for the channel formation can be represented in the plane of two dimensionless coordinates. They are $\eta_o = P_o/P_{cr}$, the incident peak power P_o normalized to the critical power P_{cr}, and a parameter $\rho_o = R_o\omega_p/c$ which incorporates the initial focal radius R_o of the incident beam, the unperturbed plasma frequency ω_p, and the speed of light c. Channeled propagation can develop in the region $\eta_o > 1$. The critical power is given by $P_{cr} = 1.62 \times 10^{10}(n_{cr}/n_e)$ W in which n_e and n_{cr} represent the electron density and the critical plasma density, respectively.

2. A. B. Borisov, A. V. Borovskiy, V. V. Korobkin, A. M. Prokhorov, O. B. Shiryaev, X. M. Shi, T. S. Luk, A. McPherson, J. C. Solem, K. Boyer, and C. K. Rhodes, Phys. Rev. Lett. 68, 2309 (1992).

3. A. B. Borisov, X. Shi, V. B. Karpov, V. V. Korobkin, O. B. Shiryaev, J. C. Solem, A. McPherson, K. Boyer, and C. K. Rhodes, "Stable Self-Channeling of Intense Ultraviolet Pulses in Underdense Plasma Producing Channels Exceeding 100 Rayleigh Lengths", J. Opt. Soc. Am. B 11, 1941 (1994).

4. A. McPherson, T. S. Luk, B. D. Thompson, A. B. Borisov, O. B. Shiryaev, X. Chen, K. Boyer, and C. K. Rhodes, Phys. Rev. Lett. 72, 1810 (1994).

5. A. McPherson, T. S. Luk, B. D. Thompson, K. Boyer, and C. K. Rhodes, Appl. Phys. B 57, 337 (1993). This concept is based on a classical formulation of the work done by

an intense external wave on an initially ionized free electron in the cluster or molecule and involves matching the conditions of excitation to both the spectroscopic structure of the atomic constituents of the molecule and their interatomic spacings. In this way, the energetics of intra-cluster inelastic electron-atom (ion) collisions can be adjusted to lead selectively to inner-shell excited states.

6. K. Boyer, B. D. Thompson, A. McPherson, and C. K. Rhodes, J. Phys. B 27, 4373 (1994).

7. A. McPherson, B. D. Thompson, A. B. Borisov, K. Boyer, and C. K. Rhodes, Nature (London) 370, 631 (1994).

8. B. D. Thompson, A. McPherson, K. Boyer, and C. K. Rhodes, J. Phys. B 27, 4391 (1994).

9. K. Boyer and C. K. Rhodes, "Superstrong Coherent Multi-Electron Intense-Field Interaction," J. Phys. B 27, L633 (1994).

10. C. Max, J. Arons, and A. B. Langdon, Phys. Rev. Lett. 33, 209 (1974).

11. A. B. Borisov, A. V. Borovskiy, V. V. Korobkin, A. M. Prokhorov, C. K. Rhodes, and O. B. Shiryaev, Phys. Rev. Lett. 65, 1753 (1990).

12. J. C. Solem, T. S. Luk, K. Boyer, and C. K. Rhodes, IEEE J. Quantum Electron. 25, 2423 (1989).

13. P. Sprangle, E. Esarey, and A. Ting, Phys. Rev. Lett. 64, 2011 (1990); P. Sprangle, C. M. Tang, and E. Esarey, Phys. Rev. A 41, 4463 (1990); A. Ting, E. Esarey, and P. Sprangle, Phys. Fluids B 2, 1390 (1990).

14. G. Z. Sun, E. Ott, Y. C. Lee, and P. Guzdar, Phys. Fluids 20, 526 (1987).

15. T. Kurki-Suonio, P. J. Morrison, and T. Tajima, Phys. Rev. A 40, 3230 (1989).

16. A. B. Borisov, O. B. Shiryaev, A. McPherson, K. Boyer, and C. K. Rhodes, "Stability

Analysis of Relativistic and Charge-Displacement Self-Channeling of Intense Laser Pulses," in OSA Proceedings on Shortwavelength V, Vol. 17, edited by P. B. Corkum and M. D. Perry (Optical Society of America, Washington, D.C., 1993) p. 58.

17. X. L. Chen and R. N. Sudan, Phys. Rev. Lett. 70, 2082 (1993).

18. A. B. Borisov, O. B. Shiryaev, A. McPherson, K. Boyer, and C. K. Rhodes, "Stability Analysis of Relativistic and Charge-Displacement Self-Channeling of Intense Laser Pulses in Underdense Plasmas," Plasma Phys. Control. Fusion 37, XXX (1995).

19. B. Bouma, T. S. Luk, K. Boyer, and C. K. Rhodes, J. Opt. Soc. Am. B 10, 1180 (1993).

20. Ernst E. Fill, J. Opt. Soc. Am. B 11, 2241 (1994).

21. David R. Miller, "Free Jet Sources," in Atomic and Molecular Beam Methods, Vol. I, edited by G. Scoles (Oxford University Press, Oxford, 1988) p. 14.

22. A. McPherson, T. S. Luk, G. Gibson, J. C. Solem, K. Boyer and C. K. Rhodes, "Studies of Strong-Field Effects in Multiphoton Subpicosecond Excited Plasmas: Soft X-Ray Fluorescence and Propagation," Fundamentals of Laser Interactions II, edited by F. Ehlotzky, (Springer-Verlag, Berlin, 1989) p. 93.

23. R. D. Evans, The Atomic Nucleus (McGraw-Hill, New York, 1955) p. 624.

24. U. Littmark and J. F. Ziegler, Range Distributions for Energetic Ions in All Elements Vol. 6 (Pergamon Press, New York, 1980) p. 99.

25. K-N. Huang, M. Aoyagi, M. H. Chen, B. Crasemann, H. Mark, At. Data Nucl. Data Tables 18, 243 (1976).

26. E. F. Plechaty, D. E. Cullen, R. J. Howerton, "Tables and Graphs of Photon-Interaction Cross Sections from 0.1 keV to 100 MeV Derived from the LLL Evaluated-Nuclear-Data Library," UCRL-50400, Vol. 6, Rev. 3, 11 November 1981.

27. K. Boyer and C. K. Rhodes, Phys. Rev. Lett. 54, 1490 (1985).

28. J.-P. Connerade and K. Dietz, J. Phys. B 25, 1185 (1992).

29. S. Augst, D. Strickland, D. D. Meyerhofer, S. L. Chin, and J. H. Eberly, Phys. Rev. Lett. 63, 2212 (1989).

30. J. D. Jackson, Classical Electrodynamics (Wiley, New York, 1962).

31. E. Esarey, J. Krall and P. Sprangle, Phys. Rev. Lett. 72, 2887 (1994).

32. In Eq. (1) m, c, e, and λ are the electron mass, the speed of light, the electronic charge, and the propagating wavelength, respectively. $\rho_{ch} = r_{ch}\omega_p/c = \rho_{eig}$ is the dimensionless radius of the channel (ρ_{eig}), with ω_p the plasma frequency, r_{ch} the physical radius of the channel, and $g_0(\rho)$ the Townes mode given in R. Y. Chiao, E. Garmire, and C. H. Townes, Phys. Rev. Lett. 13, 479 (1964).

33. K. Boyer, X. Chen, A. McPherson, B. D. Thompson, and C. K. Rhodes, Proceedings of the Sixth International Conference: Multiphoton Processes, D. K. Evans and S. L. Chin (eds.), (World Scientific, Singapore, 1994) p. 467.

34. P. Mandelbaum, J. F. Seely, C. M. Brown, D. R. Kania, and R. L. Kauffman, Phys. Rev. A 44, 5752 (1991).

35. R. Schuch, D. Schneider, D. Knapp, D. DeWitt, J. McDonald, M. H. Chen, M. W. Clark, and R. E. Marrs, Phys. Rev. Lett. 70, 1073 (1993).

36. R. L. Kauffman, "X-Ray Conversion Efficiency," in 1986 Laser Program Annual Report, Lawrence Livermore National Laboratory, UCRL-50021-86, 1987, p. 3-9.

FIGURE CAPTIONS

Fig. 1: Data and calculations associated with images of Xe(M) emission. Stagnation pressure 65 psia and plenum temperature 233 K. (a) Pinhole camera single-exposure recording. The color scale is defined by black (zero), red through violet ascending intensity, and white (maximum). The Rayleigh range (28.5 μm) is indicated. (b) Axial (radius r = 0) line-out of X-ray image shown in panel (a). The distance $\delta \cong 200$ μm separating two adjacent peaks in the longitudinal (z) direction is indicated. (c) Computed normalized intensity profile of channeled 248 nm radiation corresponding to experimental conditions for data illustrated in panel (a). $I_o = 9.4 \times 10^{18}$ W/cm^2, $P_o = 0.6$ TW, and $n_e = 6.5 \times 10^{20}$ cm^{-3}. The initial condition for the calculation used a focal diameter of 3 μm. The distance $\delta \cong 214$ μm separating two adjacent peaks in the longitudinal (z) direction is indicated, a value that is close to the experimental magnitude shown in panel (b). (d) Comparison of the transverse structures of the observed Xe(M) emission: **A** Observed radial locus corresponding to data shown in panel (a). **B** Computed radial locus corresponding to $I_{th}(\alpha) \cong 3 \times 10^{15}$ W/cm^2. **C** Computed radial locus corresponding to $I_{th}(\beta) \cong 4 \times 10^{16}$ W/cm^2. See text for details.

Fig. 2: Data and calculations associated with images of Xe(M) emission. Stagnation pressure 95 psia and plenum temperature 233 K. (a) Pinhole camera single-exposure recording. The color scale is defined by black (zero), red through violet ascending intensity, and white (maximum). The Rayleigh range (28.5 μm) is indicated. (b) Axial (radius r = 0) line-out of X-ray image shown in panel (a). The inset shows the relative positions of the 0.5 mm nozzle and the barrier with

the ~ 100 μm opening. (c) Computed normalized intensity profile of channeled 248 nm radiation corresponding to experimental conditions for data illustrated in panel (a). $I_o = 9.4 \times 10^{18}$ W/cm^2, $P_o = 0.6$ TW, and $n_e = 9.6 \times 10^{20}$ cm^{-3}. The initial condition for the calculation used a focal diameter of 3 μm. (d) Comparison of the transverse structures of the observed Xe(M) emission: **A** Observed radial locus corresponding to data shown in panel (a). **B** Computed radial locus corresponding to $I_{th}(\alpha) \cong 3 \times 10^{15}$ W/cm^2. **C** Computed radial locus corresponding to $I_{th}(\beta) \cong 4 \times 10^{16}$ W/cm^2. See text for details.

Fig. 3: Representation of the allowed zone (shaded) for production of prompt Xe M-shell emission from Xe clusters as a function of intensity of irradiation and cluster size for excitation with a wavelength of 248 nm. The upper boundary $I_{max}(N)$ is established by the intensity required to fully ionize the Xe N-shell as found with a tunneling picture [Ref. (27)]. The lower boundaries [I_o' and I_n(248 nm)] are determined by a classical formulation of the work done by an intense external wave on an initially ionized free electron in the cluster Refs. [4-6]. The effect of coherent electron motion is included [Ref. (6)]. The point β' is specified by $n_{\beta'} \cong 3$ and $I_{\beta'} \cong 3.8 \times 10^{15}$ W/cm^2.

Fig. 4: Transverse distribution of channeled 248 nm intensity distribution shown in Fig. 2(c) for longitudinal position z = 1050 μm. The three levels (i = α, β, γ) for the threshold intensities [I_{th}(i)] are indicated. Corresponding radial parameters $r(\alpha) \cong 27$ μm, $r(\beta) \cong 2$ μm, and $r(\gamma) \cong 60$ μm are also shown. See text for discussion. The peak intensity in the channel I_{ch}, defined in Eq. (2), and the intensity I_m representing the broad second maximum of the distribution are designated. The characteristic intensities $I_{max}(N)$ and $I_{\beta'}$, transferred from Fig.

3, are also indicated. The magnitudes are such that $I_{th}(\alpha) \cong I_{\beta'}$. The intensity representing the initial condition for the calculated distribution is $I_0 = 9.4 \times 10^{18}$ W/cm^2.

Fig. 5: (a) Image of Xe(M) emission with pinhole camera having a 25 μm pinhole for a 1:2 (Xe:He) mixture with a stagnation pressure of 90 psia and a plenum temperature of 293 K. Unlike the images shown in Figs. 1(a) and 2(a), the nozzle had a diameter of 0.8 mm and the barrier illustrated in Fig. 2(b) was removed. The arrow specifies the longitudinal position ($z = 956$ μm) of the transverse distribution shown in panel (b). The color scale is defined by black (zero), red through violet ascending intensity, and white (maximum). (b) Transverse Xe(M) intensity profile at $z = 956$ μm with a measured width $\Delta_m \cong 30$ μm, a value in agreement with the estimated resolution limit $\Delta \sim 30$ μm.

Fig. 6: Stability map for the propagation in initially homogeneous plasmas of pulses having perturbed Gaussian incident transverse intensity distributions as computed in Ref. (16). $\rho_0 = R_0\omega_p/c$ with R_0 = radius of the incident Gaussian profile, ω_p the plasma frequency, and c the speed of light. $\eta_0 = P_0/P_{cr}$, the incident peak power P_0 normalized by the critical power defined in Ref. 1. The optimal zone is designated by the small rectangle. Points A and B correspond to optimization of Xe(M) emission with 248 nm radiation with $P_0 = 1$ TW and $P_0 = 1.5$ TW, respectively. Point E1 ($\eta_0 = 1.32$, $\rho_0 = 6.84$) corresponds to the experimental data shown in Fig. 1. Point E2 ($\eta_0 = 1.94$, $\rho_0 = 8.31$) corresponds to the experimental data shown in Fig. 2. The eigenmode curve is shown in addition to the areas representing stable and unstable (shaded) propagation.

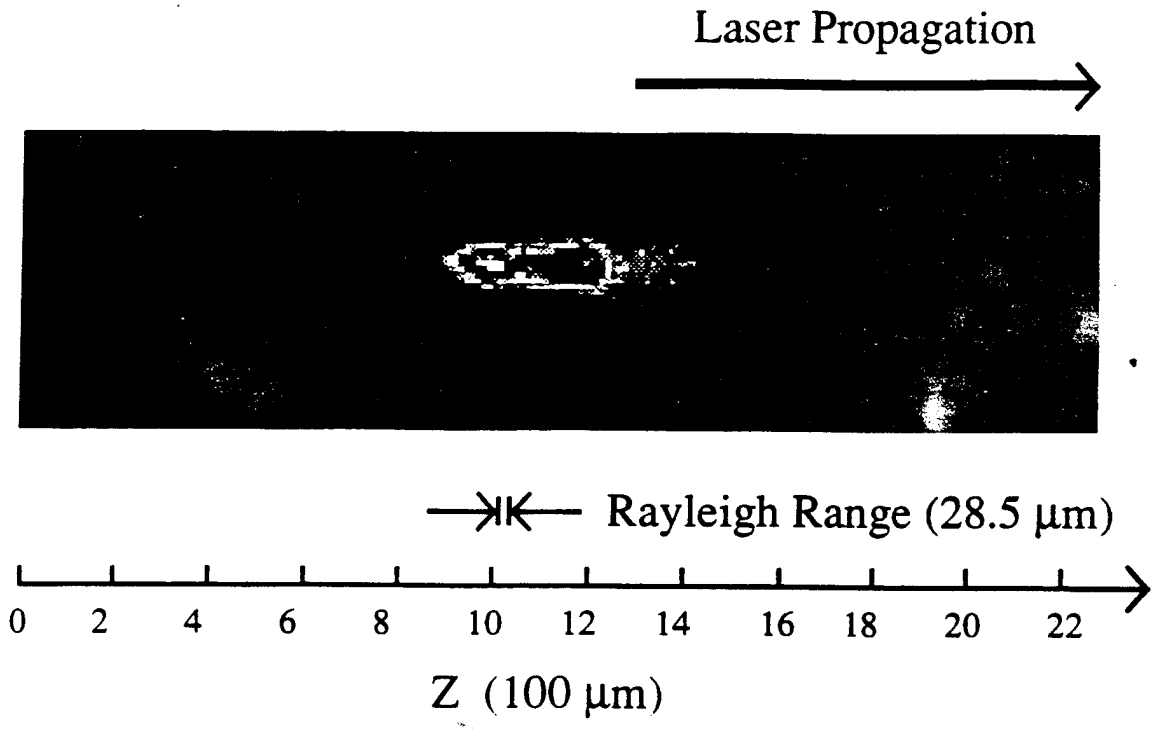
Laser Propagation
Rayleigh Range (28.5 μm)
0 2 4 6 8 10 12 14 16 18 20 22
Z (100 μm)

Fig. 1(a)

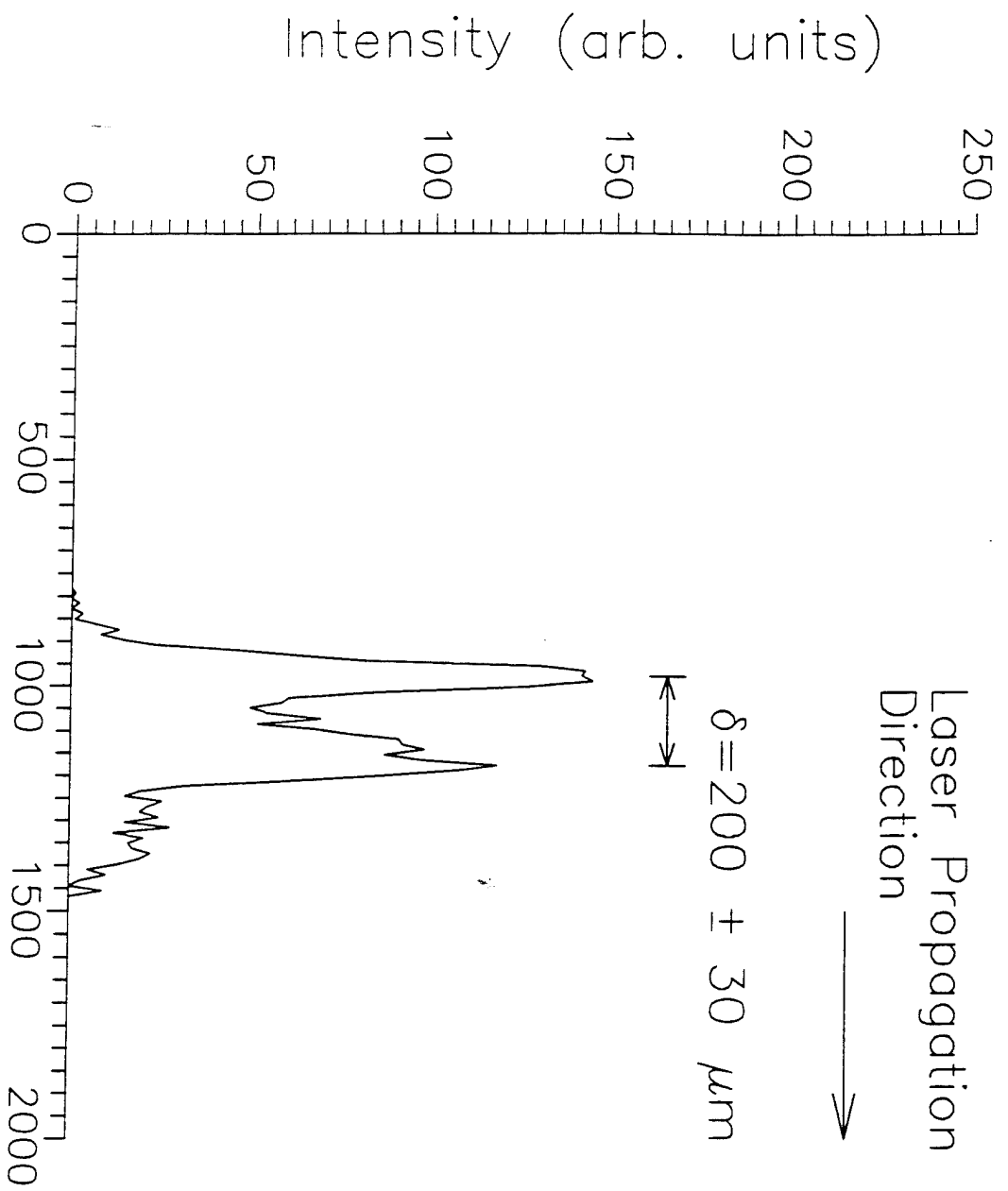
Intensity (arb. units)
0
50
100
150
200
250
0
500
1000
1500
2000
Axial Distance z (μm)
δ=200 ± 30 μm
Laser Propagation Direction

Fig. 1(b)

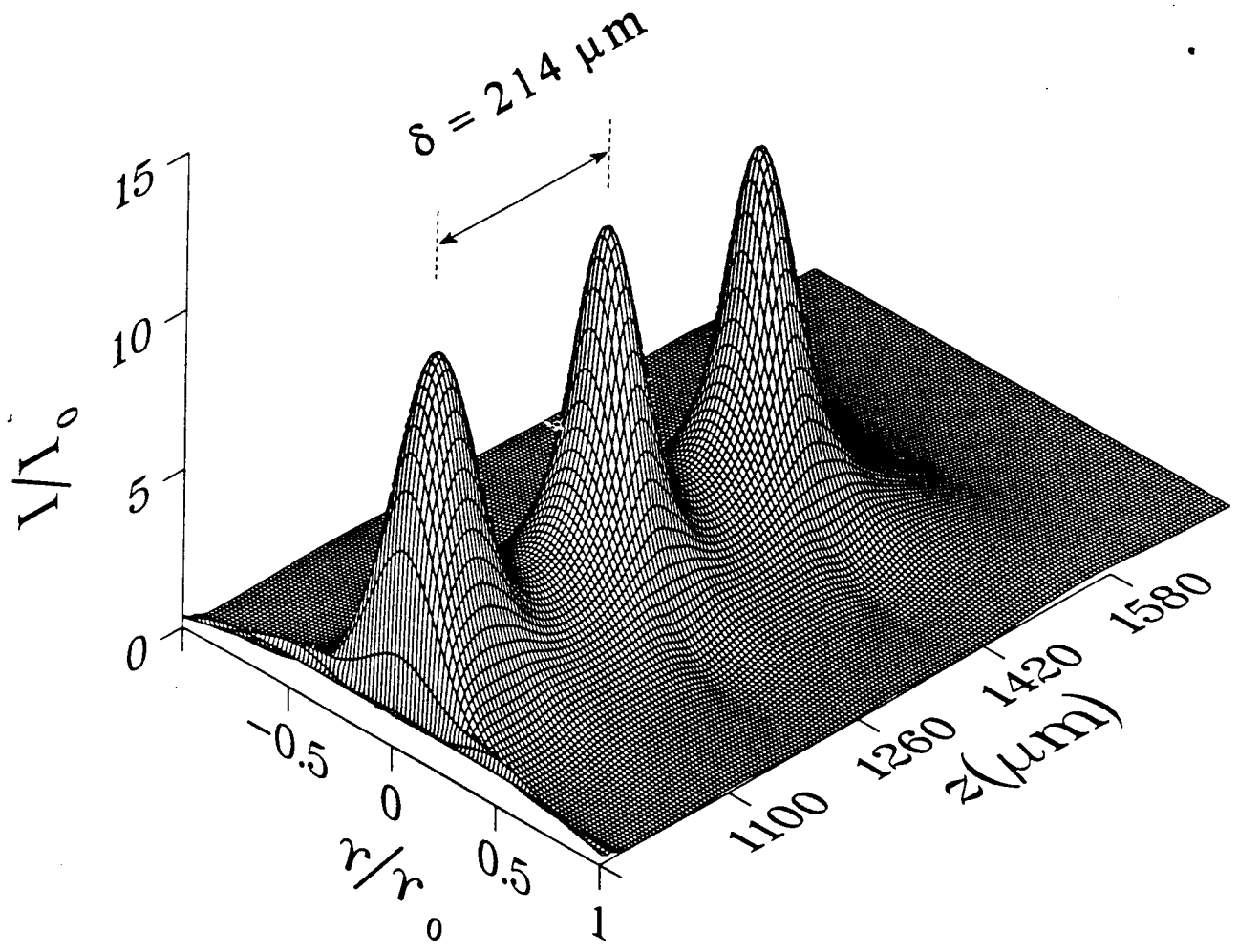

Fig. 1(c)

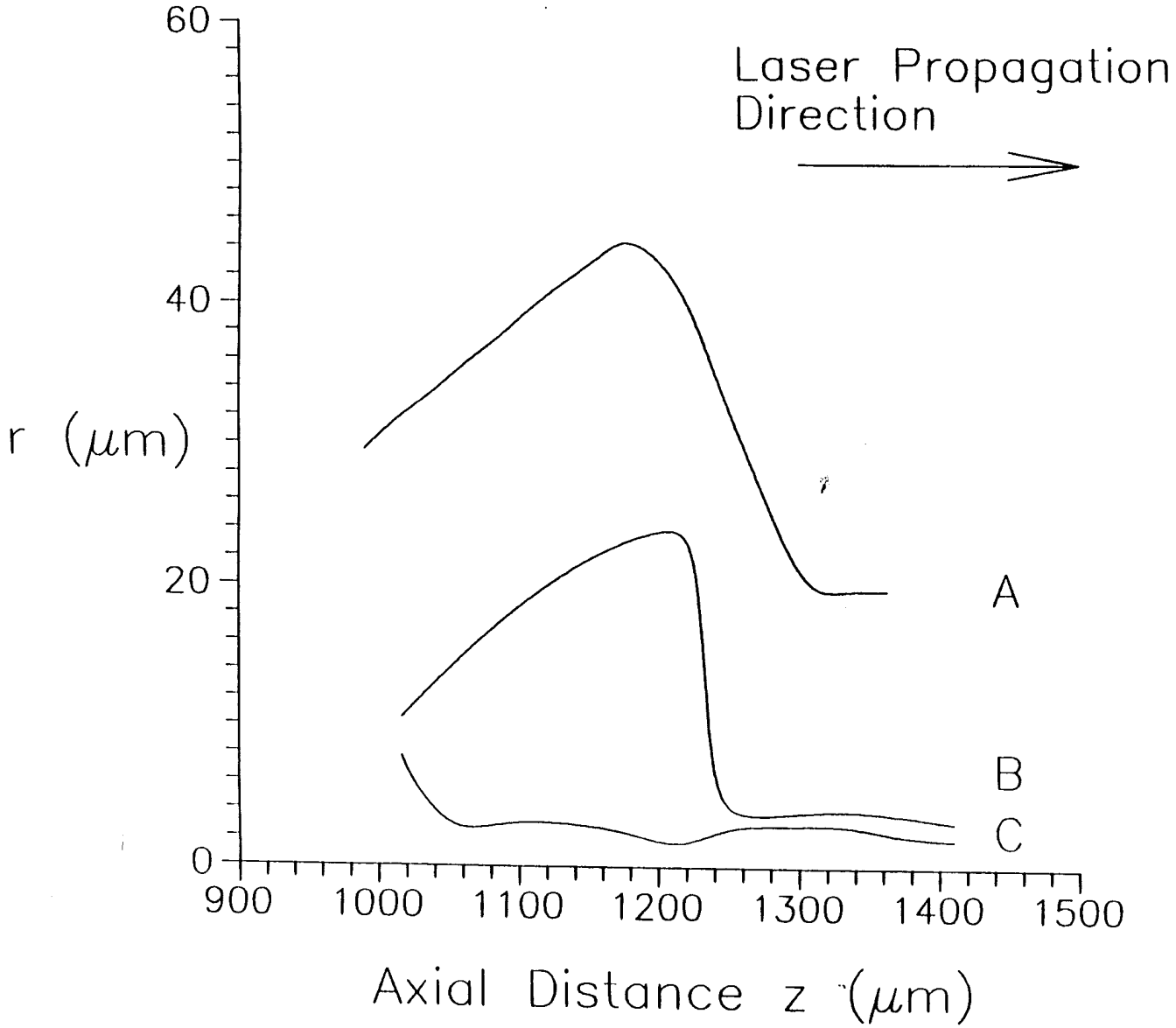
60
40
20
0
r (μm)
Laser Propagation
Direction
A
B
C
900
1000
1100
1200
1300
1400
1500
Axial Distance z (μm)

Fig. 1(d)

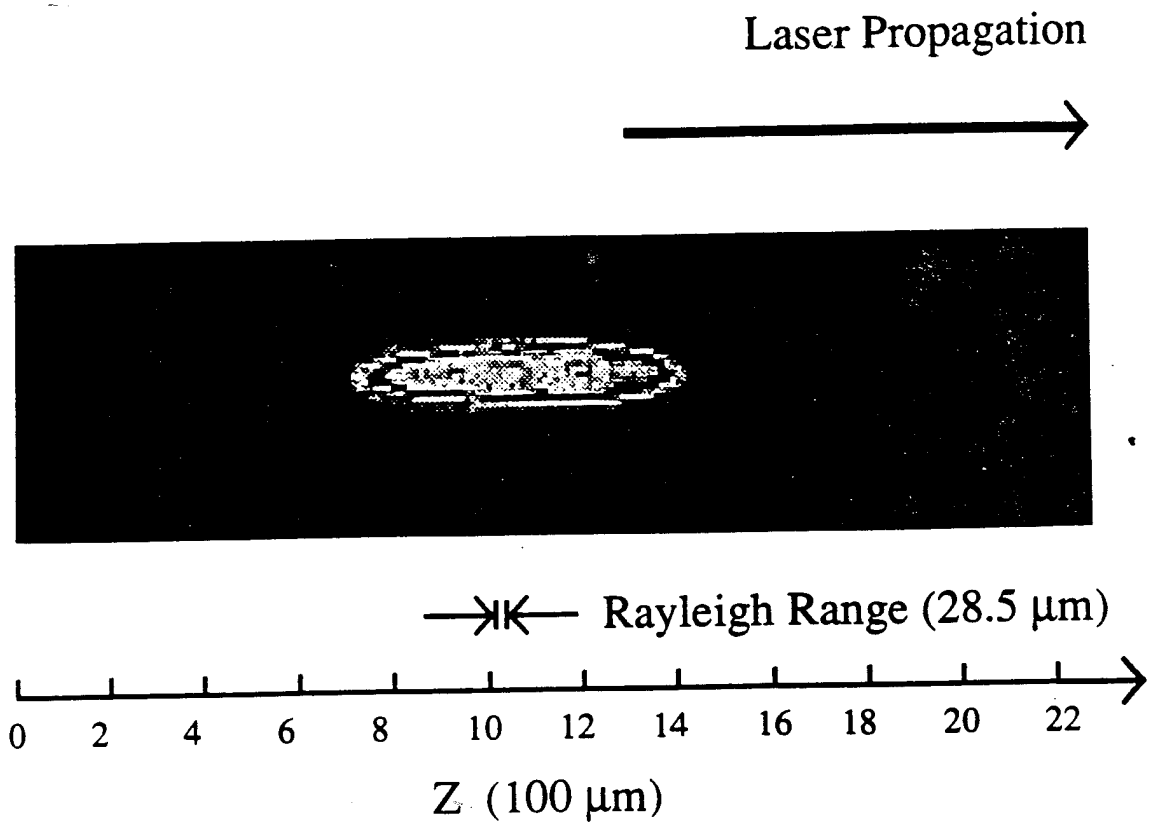
Laser Propagation
Rayleigh Range (28.5 μm)
0 2 4 6 8 10 12 14 16 18 20 22
Z (100 μm)

Fig. 2(a)

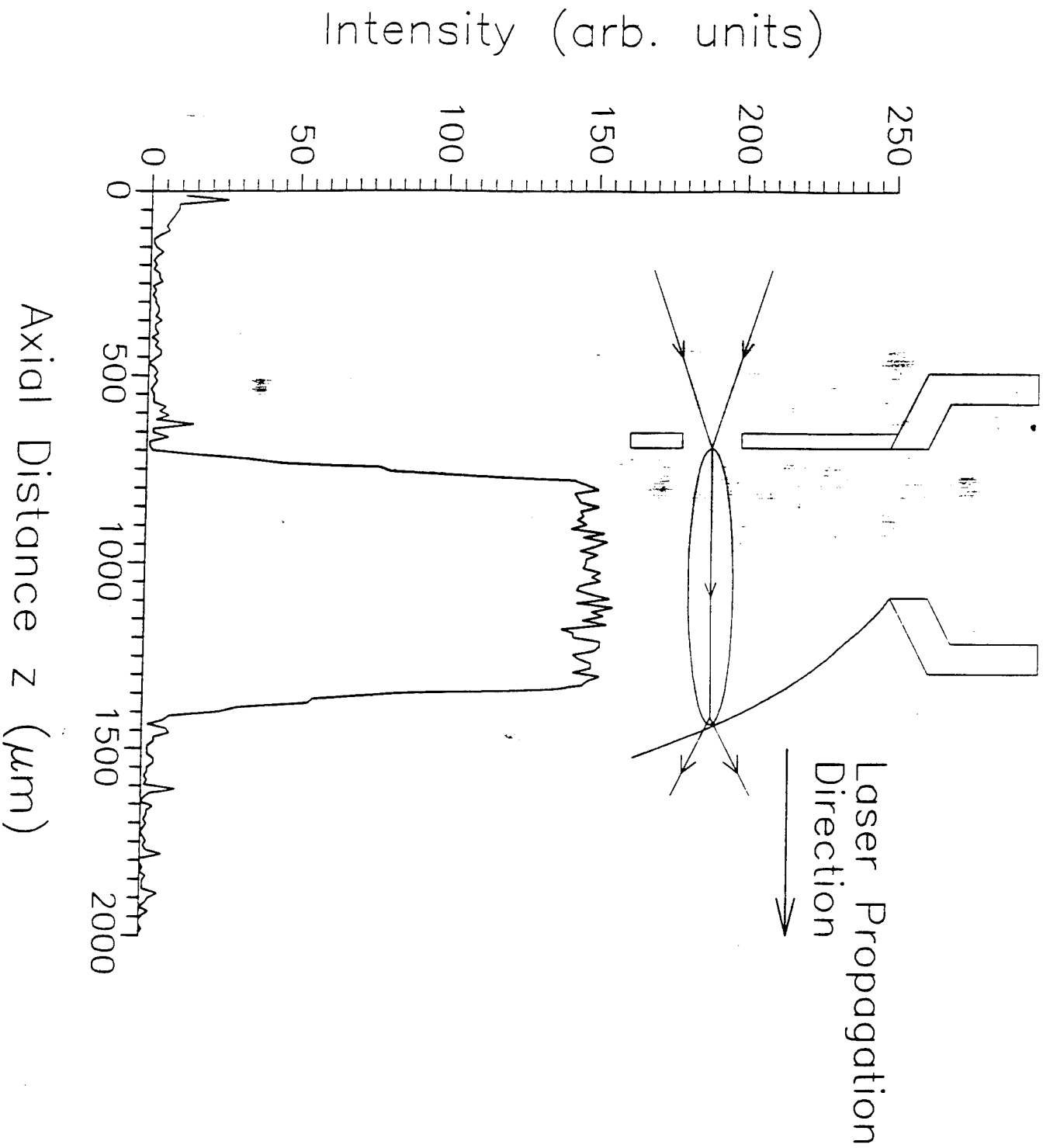
Intensity (arb. units)
0
50
100
150
200
250
0
500
1000
1500
2000
Axial Distance z (μm)
Laser Propagation Direction

Fig. 2(b)

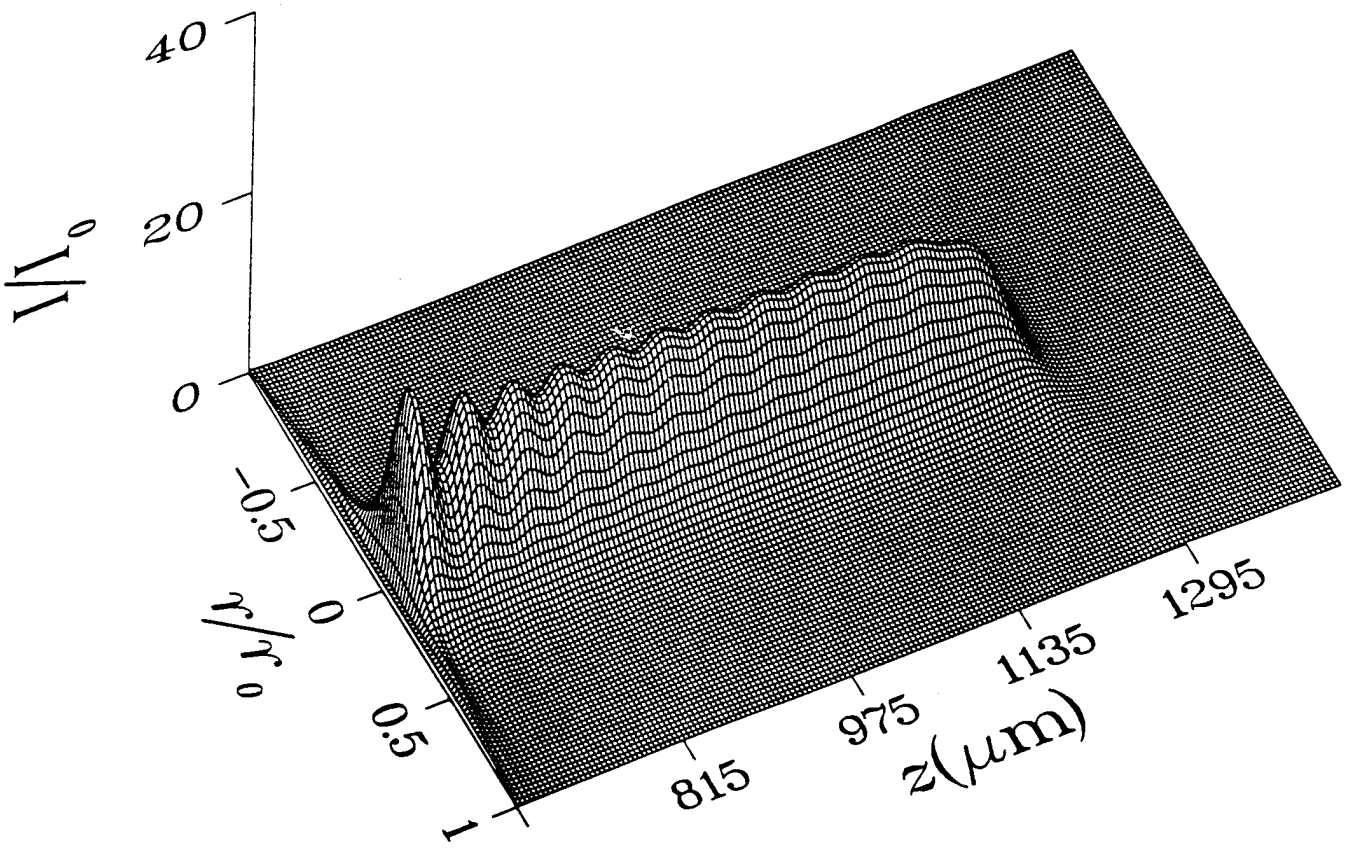

Fig. 2(c)

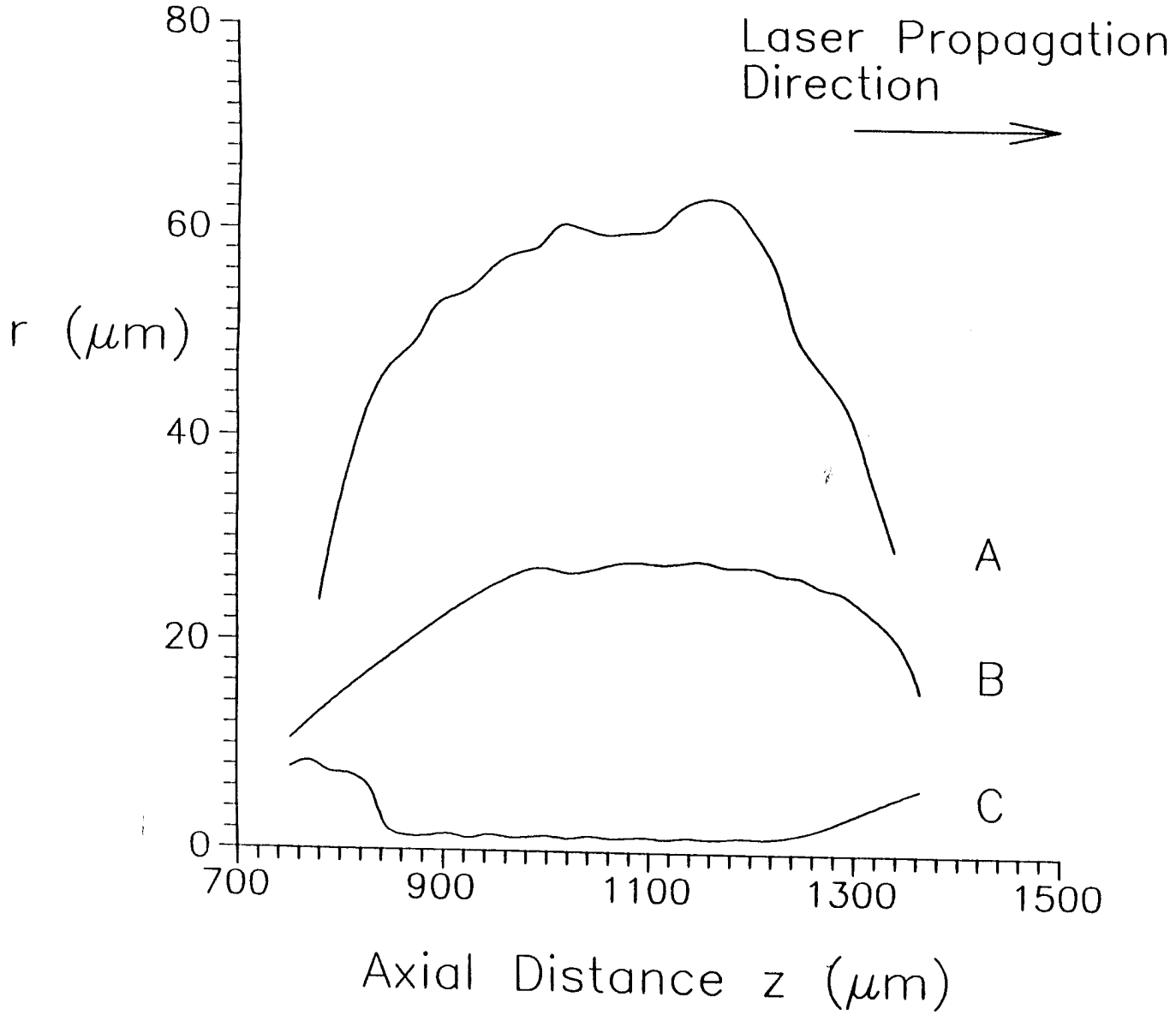
Laser Propagation Direction
80
60
40
20
0
r (μm)
A
B
C
700
900
1100
1300
1500
Axial Distance z (μm)

Fig. 9(d)

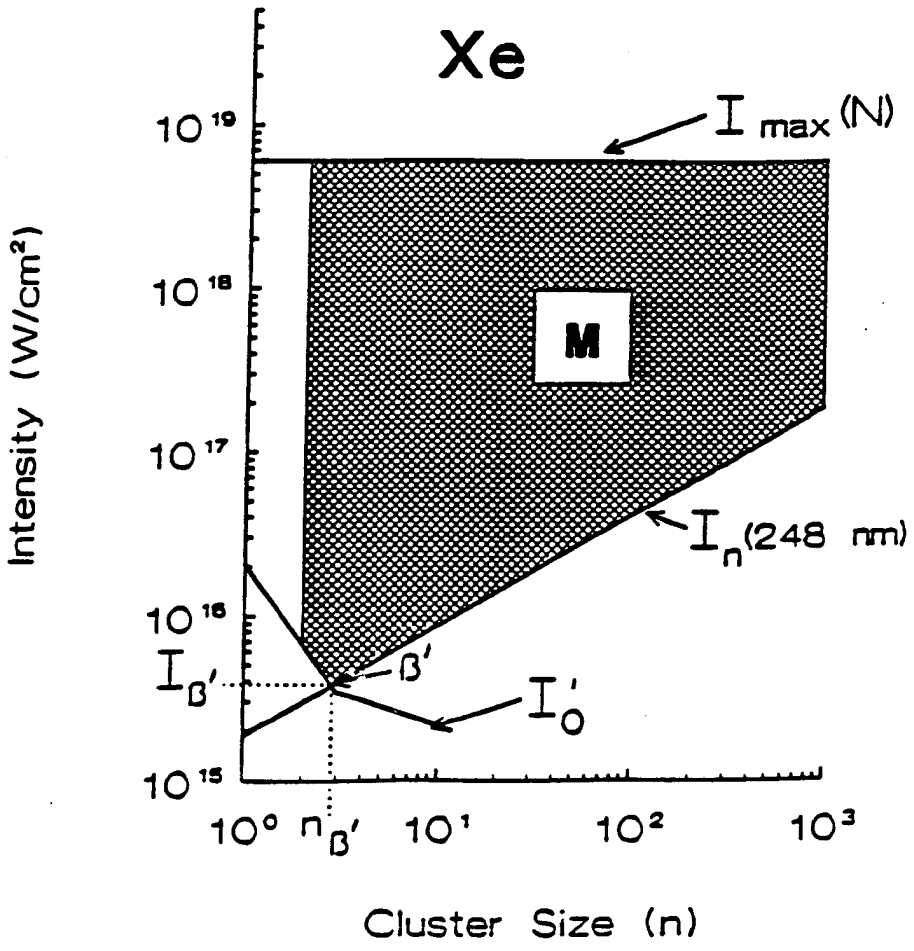
Xe
I_{max} (N)
10^{19}
10^{18}
10^{17}
10^{16}
10^{15}
M
I_n(248 nm)
$I_{\beta'}$
β'
I'_0
10^0 $n_{\beta'}$ 10^1 10^2 10^3
Intensity (W/cm^2)
Cluster Size (n)

Fig. 3

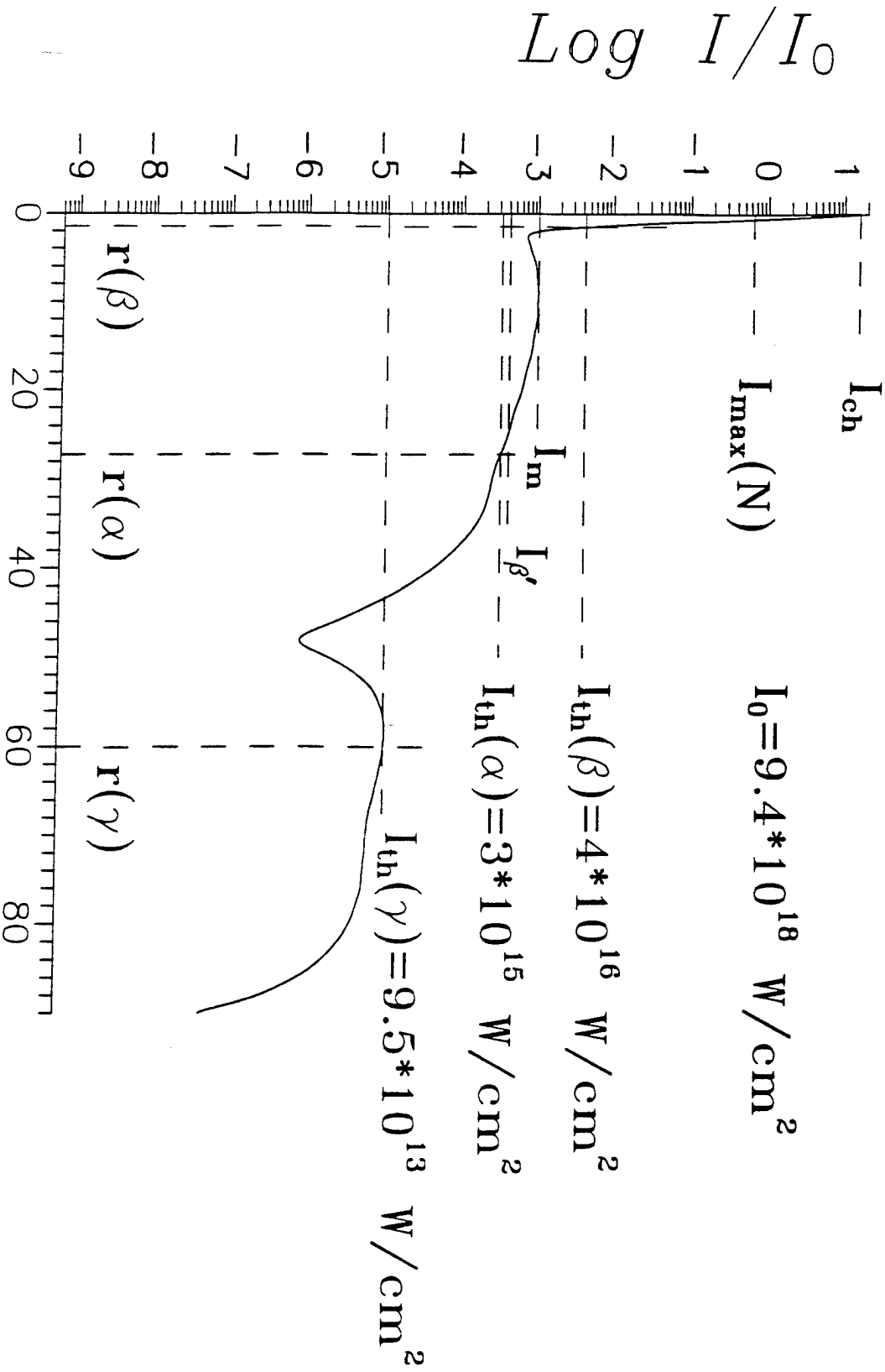
Log I/I0
1
0
−1
−2
−3
−4
−5
−6
−7
−8
−9
Ich
Imax(N)
Im
Iβ′
Ith(β)=4*10^16 W/cm^2
Ith(α)=3*10^15 W/cm^2
Ith(γ)=9.5*10^13 W/cm^2
I0=9.4*10^18 W/cm^2
r(β)
r(α)
r(γ)
0
20
40
60
80
r(μm)

Fig. 4

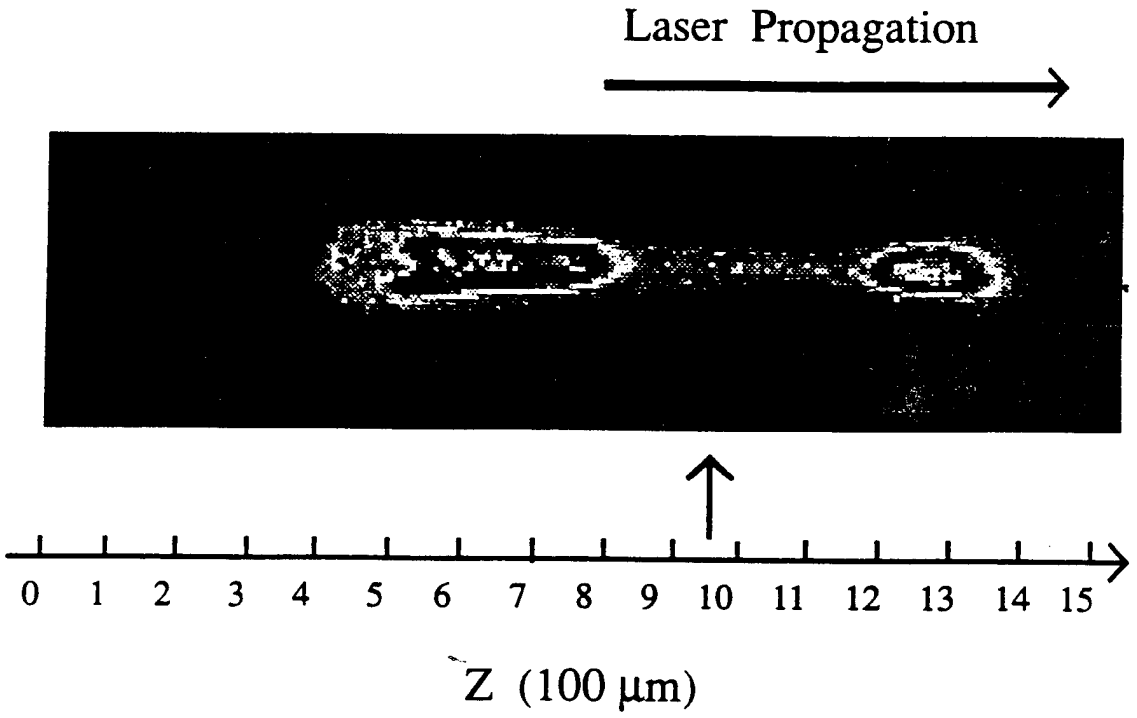

Fig. 5(a)

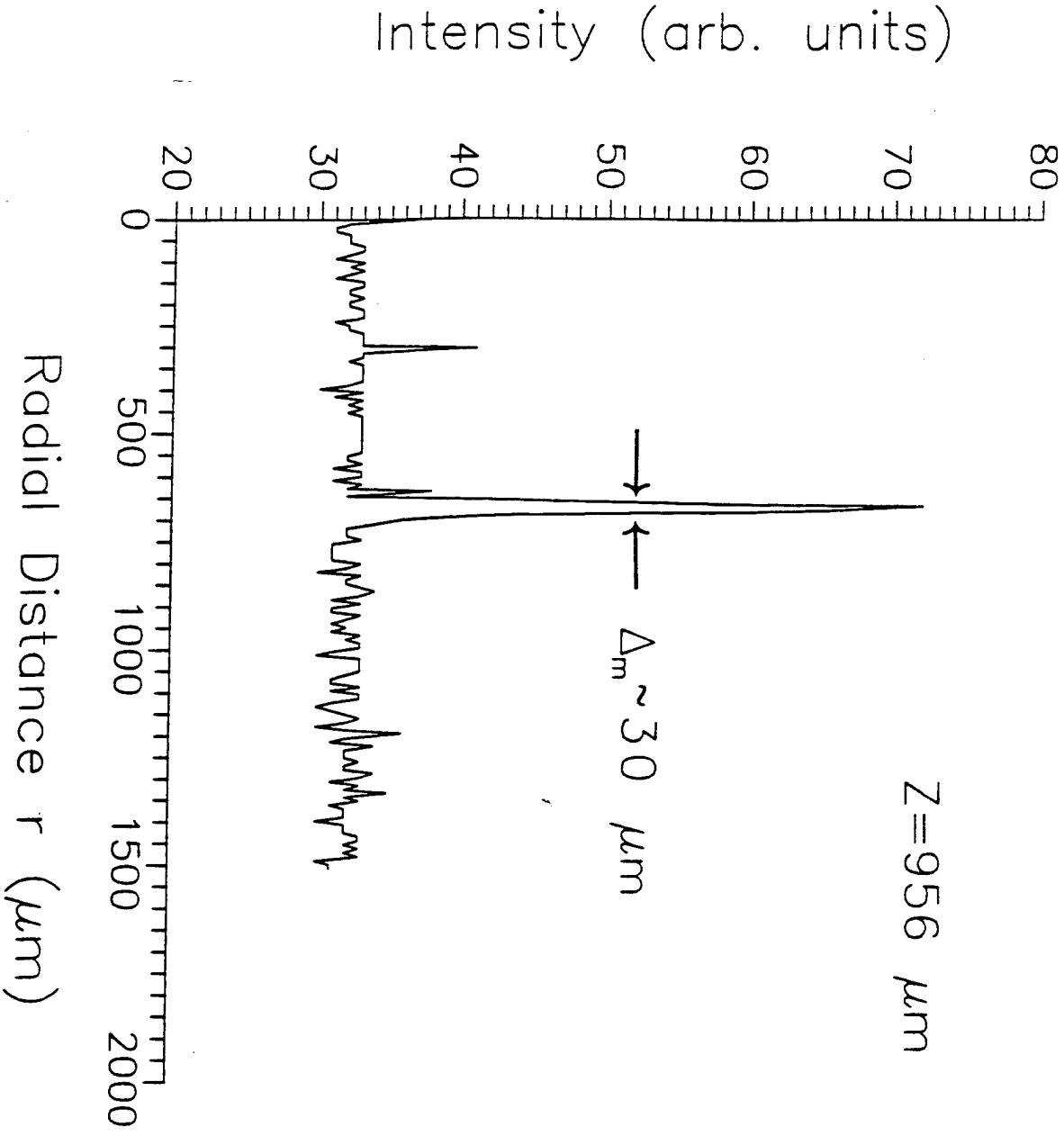
Intensity (arb. units)
20
30
40
50
60
70
80
0
500
1000
1500
2000
Radial Distance r (μm)
Δm ~ 30 μm
Z=956 μm

Fig. 10(b)

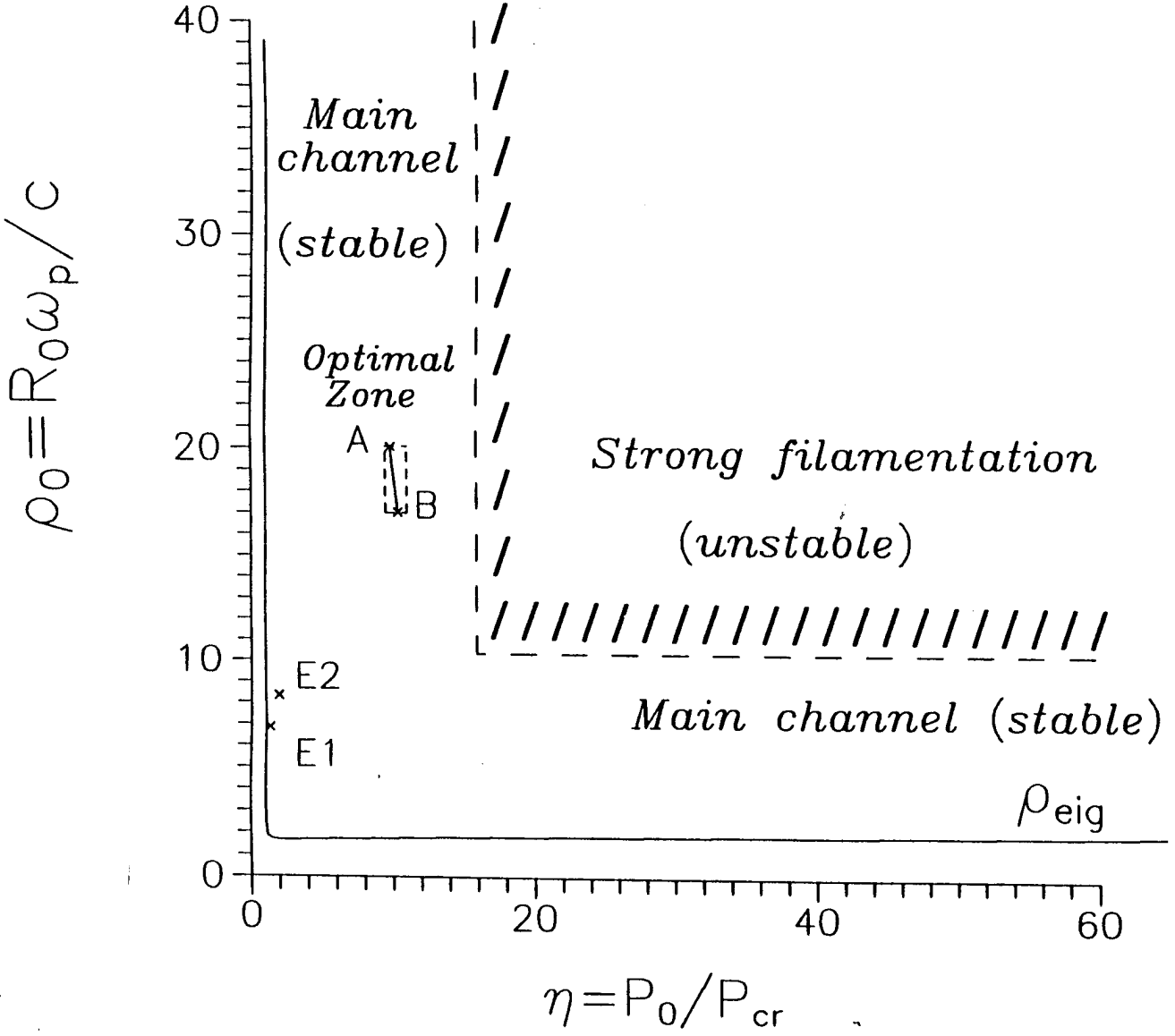
40
30
20
10
0
0
20
40
60
$\rho_0 = R_0\omega_p/c$
$\eta = P_0/P_{cr}$
Main channel (stable)
Optimal Zone
A
B
E2
E1
Strong filamentation (unstable)
Main channel (stable)
ρ_{eig}

Fig. 602

Appendix H: "X-Ray Amplifier Energy Deposition Scaling with Channeled Propagation"

REPRINTED FROM THE PROCEEDINGS OF THE INTERNATIONAL CONFERENCE ON LASERS '91, DECEMBER 9-13, 1991

X-RAY AMPLIFIER ENERGY DEPOSITION SCALING WITH CHANNELED PROPAGATION

K. Boyer*, T. S. Luk*, A. McPherson*, X. Shi*, J. C. Solem**, C. K. Rhodes*, A. B. Borisov†, A. V. Borovskiy††, O. B. Shiryaev†, V. V. Korobkin ††

* Department of Physics, University of Illinois at Chicago, Chicago, IL 60680, USA.

** Theoretical Division, Los Alamos National Laboratory, Los Alamos, NM 87545, USA.

† Laboratory for Computer Simulation, Research Computer Center, Moscow State University, Moscow, 119899, RUSSIA

†† General Physics Institute, Academy of Sciences RUSSIA, Moscow, 117942, RUSSIA.

Abstract

The spatial control of the energy deposited for excitation of an x-ray amplifier plays an important role in the fundamental scaling relationship between the required energy, the gain and the wavelength. New results concerning the ability to establish confined modes of propagation of short pulse radiation of sufficiently high intensity in plasmas lead to a sharply reduced need for the total energy deposited, since the concentration of deposited power can be very efficiently organized.

I. Discussion of Research

Recent theoretical[1,2] and experimental[3] studies have led to a fundamental development concerning the generation of high-brightness x-ray sources. These results affect our ability to controllably apply very high power densities in materials, the basic issue for the creation of bright and efficient sources of radiation in the x-ray range. The main significance of this work is the establishment of the scaling law concerning the energy requirements for x-ray amplification in the kilovolt range shown in Fig. 1. Importantly, the parameters represented in Fig. 1, and which define the relationship presented, are based on both theoretical and experimental information.

The critical governing issue, which determines the scaling relationship between the required excitation energy (E) and the amplifier gain (G) of x-ray lasers, is the spatial control of the deposited energy. The information presented in Fig. 2 shows that optimizing the gain (G) per unit energy (E) calls for the guided mode of propagation in order to optimally control the deposition of the energy.[4] Overall, in comparison to traditional forms of excitation, for a fixed x-ray energy output (E_X) and wavelength (λ_X), a reduction of several orders of magnitude in the necessary energy (E) results, as shown in Fig. 1, if this form of confined (channeled) propagation can be achieved. Therefore, if this scaling holds, a relatively small and useful laboratory-scale technology becomes feasible.

Recent experiments,[3] which are supported by carefully developed theoretical analysis,[1-2] have demonstrated the basic physics of a new form propagation exactly of the type necessary for the implementation of x-ray lasers of a fundamentally new regime of electromagnetic propagation is expected to arise in plasmas for short-pulse radiation at sufficiently high intensity. Dynamical calculations of the propagation in plasmas, incorporating both relativistic[1,5] and charge-displacement mechanisms,[2,6-9] indicate that the combined action of these processes can lead to a new stable form of spatially channeled propagation. Specifically, these experimental studies which have examined a new relativistic regime of high-intensity short-pulse propagation in plasmas, present evidence for the information of such a stable mode of spatially confined (channeled) propagation. For an electron density of ~ 1.35×10^{21} cm^{-3} and a power of ~ 3×10^{11} W, the results indicate a channel radius < 1 μm and a peak intensity ~ 10^{19} W/cm^2. Comparison of these findings with

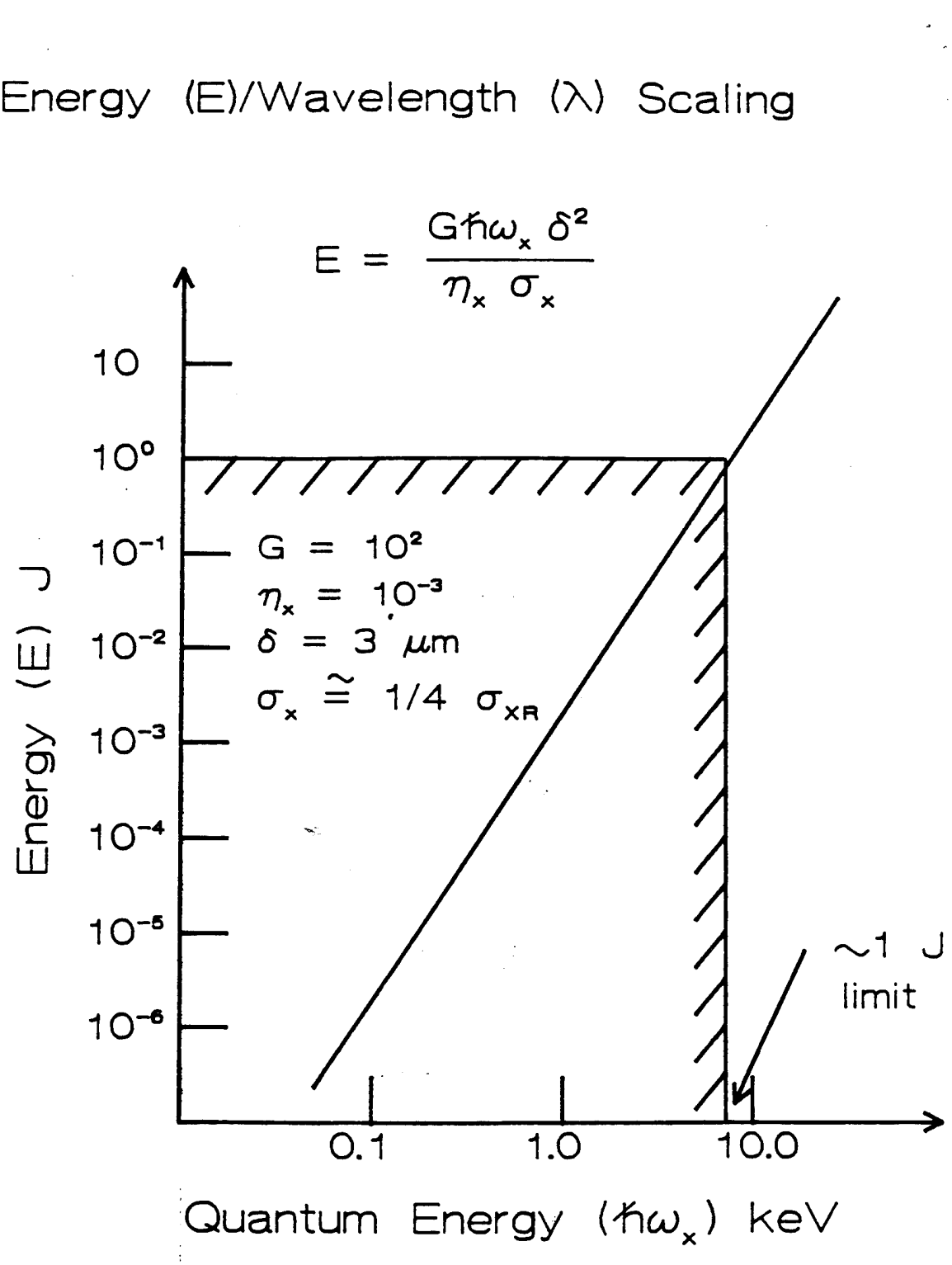

Fig. 1: Scaling relationship between required excitation energy (E) and quantum energy ($\hbar\omega_x$) characteristic of the amplifier. Parameters: total gain exponent G = 100, energy efficiency $\eta_x = 10^{-3}$, channel diameter δ = 3 μm, x-ray ($\hbar\omega_x$) cross section for stimulated emission σ_x, x-ray cross section for stimulated emission for radiatively-broadened transition σ_{xR}.

X-Ray Laser Scaling

Spatial Distribution/Amplifying Volume

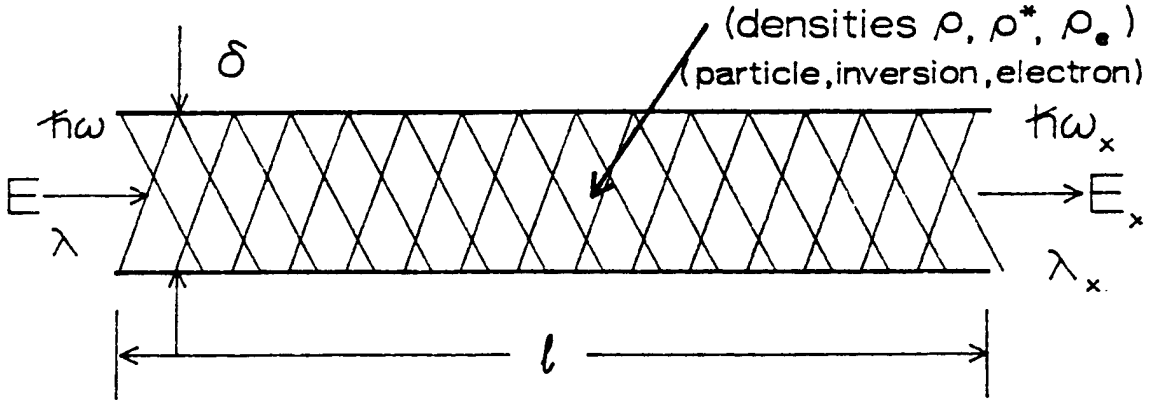

$$E = \frac{\hbar\omega_x \rho^* \delta^2 l}{\eta_x}$$

$$G = \rho^* \sigma_x l$$

Laboratory Scale Technology--

$$\frac{G}{E} = \frac{\eta_x \sigma_x}{\hbar\omega_x \delta^2} \Rightarrow \text{small } \delta$$

$\therefore$ Large l/δ, but $\delta \geq \sqrt{\lambda l}$ free space propagation

Really want to set--

$l >>$ Rayleigh range $l_R \sim \delta^2/\lambda$

$l \sim$ loss length

δ small ρ^* large as possible

$\therefore$ **Guided Mode of Propagation**

Fig. 2: Spatial distribution of energy of excitation (E) for an x-ray ($\hbar\omega_x$) amplifier. Parameters are the same as in Fig. 1 with λ the wavelength of the excitation energy, assumed longitudinally delivered, and with ρ, ρ^*, and ρ_e representing the particle, inversion and electron densities, respectively. The analysis shows that optimization of G/E requires a guided mode of propagation so that high concentrations of power can be organized into high-aspect-ratio spatial volumes.

a dynamical theory[2] yield close agreement for both the longitudinal structure and the radial extent of the propagation observed. These results represent a profound change in the field of x–ray laser research because they alter drastically the fundamental scaling relationships among the relevant physical variables.

The implications of this development for general applications to x–ray imaging and the micro–characterization of condensed matter are extremely important and propitious. In terms of the x–ray source, they are (1) that a properly controlled energy deposition rate, sufficient for the production of stimulated x–ray sources up to a few kilovolts in quantum energy, can now be achieved with an excitation energy of ~ 1 J, (2) that an x–ray output energy of ~ 1 mJ per pulse is achievable with laboratory–scale technology, and (3) that an x–ray beam diameter (~ 2 – 3 μm) arises as a natural consequence of the physics. These parameters represent an exceptionally high peak brightness figure that permits a new and completely unexplored range of physical measurements to be made. Indeed, a high–brightness source of this nature is ideal for the microimaging of condensed matter. In particular, an x–ray source with these parameters is perfectly matched to the requirements for holographic imaging of biological materials[10–14] in terms of all its relevant properties, specifically, wavelength (10 – 40 Å), pulse energy (~ 1 mJ), pulse length (~ 10^{-13} s), beam diameter (~ 2 – 3 μm), and divergence (~ 1 mrad).

II. Conclusion

Recent experimental and theoretical results on electromagnetic propagation at high intensities in plasmas lead to very favorable scaling relationships for high–brightness x–ray amplifiers. Such x–ray sources will have important applications in the holographic imaging of biological materials.

III. Acknowledgements

The authors acknowledge the expert technical assistance of J. Wright and P. Noel in addition to fruitful conversations with A. R. Hinds, R. R. Goldstein, and B. Bouma. Support for this research was partially provided under contracts AFOSR–89–0159, (ONR) N00014–91–J–1106, (SDI/NRL) N00014–91–K–2013, (ARO) DAAL 3–91–G–0174, (DoE) DE–FG02–91ER1208, and (NSF) PHY–9021265.

IV.References

1. A. B. Borisov, A. V. Borovskiy, V. V. Korobkin, A. M. Prokhorov, C. K. Rhodes, and O. B. Shiryaev, "Stabilization of Relativistic Self–Focusing of Intense Subpicosecond Ultraviolet Pulses in Plasmas", Phys. Rev. Lett. 65, 1753 (1990).
2. A. B. Borisov, A. V. Borovskiy, O. B. Shiryaev, V. V. Korobkin, A. M. Prokhorov, J. C. Solem, T. S. Luk, K. Boyer, and C. K. Rhodes, "Relativistic and Charge–Displacement Self–Channeling of Intense Ultrashort Laser Pulses in Plasmas", Phys. Rev. A, in press.
3. A. B. Borisov, A. V. Borovskiy, V. V. Korobkin, A. M. Prokhorov, O. B. Shiryaev, X. M. Shi, T. S. Luk, A. McPherson, J. C. Solem, K. Boyer, and C. K. Rhodes, "Observation of Relativistic/Charge–Displacement Self–Channeling of Intense Subpicosecond Ultraviolet (248 nm) Radiation in Plasmas", Phys. Rev. Lett., submitted.
4. K. Boyer, A. B. Borisov, A. V. Borovskiy, O. B. Shiryaev, D. A. Tate, B. E. Bouma, X. Shi, A. McPherson, T. S. Luk, and C. K. Rhodes, "Methods of Concentration of Power in Materials for X–Ray Amplification", Appl. Optics, in press.
5. C. Max, J. Arons, and A. B. Langdon, "Self–Modulation and Self–Focusing of Electromagnetic Waves in Plasmas," Phys. Rev. Lett. 33, 209 (1974).
6. J. C. Solem, T. S. Luk, K. Boyer, and C. K. Rhodes "Prospects for X–Ray Amplification with Charge–Displacement Self Channeling," IEEE J. Quantum Electron. QE–25, 2423 (1989).
7. P. Sprangle, E. Esarey, and A. Ting, "Nonlinear Theory of Intense Laser Plasma Interactions," Phys. Rev. Lett. 64, 2011 (1990); Phys. Rev. A 41, 4463 (1990); P. Sprangle, C. M. Tang,

and E. Esarey, "Relativistic Self–Focusing of Short–Pulse Radiation Beams in Plasmas," IEEE Trans. Plasma Sci. 15, 145 (1987).

8. G. Z. Sun, E. Ott, Y. C. Lee, and P. Guzdar, "Self Focusing of Short Intense Pulses in Plasmas," Phys. Fluids 30, 526 (1987).
9. T. Kurki–Suonio, P. J. Morrison, and T. Tajima, "Self–Focusing of an Optical beam in a Plasma," Phys. Phys. Rev. A 40, 3230 (1989).
10. J. C. Solem and G. C. Baldwin, "Microholography of Living Organisms", Science 218, 229 (1982).
11. W. S. Haddad, D. Cullen, K. Boyer, C. K. Rhodes, J. C. Solem and R. S. Weinstein, "Design for a Fourier–Transform Holographic Microscope," in X–Ray Microscopy II, D. Sayre, M. Howells, J. Kirz and H. Rarback, eds. (Springer–Verlag, Berlin, 1988) pp. 284–287.
12. W. S. Haddad, J. C. Solem, D. Cullen, K. Boyer, and C. K. Rhodes, "A Description of the Theory and Apparatus for Digital Reconstruction of Fourier Transform Holograms," in Electronics Imaging '87, Advanced Printing of Paper Summaries, Vol. II (Institute for Graphic Communication, Inc., Boston, 1987) pp. 683–688.
13. W. S. Haddad, D. Cullen, J. C. Solem, K. Boyer, and C. K. Rhodes, "X–Ray Fourier–Transform Holographic Microscope," in Short Wavelength Coherent Radiation: Generation and Applications, Vol. 2, R. W. Falcone and J. Kirz, eds. (Optical Society of America, Washington, D.C., 1988) pp. 284–289.
14. W. S. Haddad, D. Cullen, J. C. Solem, J. W. Longworth, A. McPherson, K. Boyer, and C. K. Rhodes, "Fourier Transform Holographic Microscope", Appl. Opt., in press.